Characterization of midlatitude cirrus clouds with airborne lidar - Investigating an indirect aviation effect

Benedikt Leander Urbanek

München 2019

Characterization of midlatitude cirrus clouds with airborne lidar - Investigating an indirect aviation effect

Benedikt Leander Urbanek

Dissertation
an der Fakultät für Physik
der Ludwig–Maximilians–Universität
München

vorgelegt von
Benedikt Leander Urbanek
aus Finning

München, den 26.07.2019

Erstgutachter: Prof. Dr. Bernhard Mayer
Zweitgutachter: Prof. Dr. Markus Rapp
Tag der mündlichen Prüfung: 09.10.2019

Zusammenfassung

Angesichts global steigender Temperaturen ist die Wissenschaft gefordert, alle potentiellen Einflüsse auf das Klima zu erforschen. Zirruswolken, die aus kleinen Eiskristallen bestehen, weisen aufgrund ihrer großen Ausdehnung eine beträchtliche Klimawirkung auf. Sie sorgen für große Unsicherheiten in der Klimavorhersage, da nicht klar ist, wie sich ihr Einfluss in einem sich wandelnden Klima und durch menschliche Aktivitäten verändert.

Stetig zunehmender Flugverkehr verursacht die Bildung von Kondensstreifen, die unter den passenden Bedingungen für längere Zeit fortbestehen können und den gesamten Zirrenbedeckungsgrad erhöhen. Neben diesem direkten Effekt wurde schon vor Jahrzehnten das Konzept eines indirekten Luftfahrtseffekts vorgeschlagen. Eine Anzahl von Modellierungsstudien hat seither diesen Effekt untersucht, bei dem Flugzeug-Abgaspartikel zur Hintergrundbelastung mit Aerosolen in der oberen Troposphäre beitragen und als Eiskeime während der natürlichen Zirruswolkenbildung fungieren. Bisher wurde dieser jedoch noch nie in Feldstudien nachgewiesen. Die Abschätzung der Strahlungswirkung mithilfe globaler Zirkulationsmodellen brachte widersprüchliche Resultate hervor. Sie reichen von keiner signifikanten Wirkung bis zu einem Strahlungsantrieb im Bereich von $-350\,\mathrm{mW\,m^{-2}}$ bis $90\,\mathrm{mW\,m^{-2}}$. Diese Unsicherheiten lassen sich mit dem Fehlen von Beobachtungen erklären, da diese benötigt werden, um die relevanten Modellszenarien einzugrenzen.

In der vorliegenden Arbeit werden Zirruswolken in den nördlichen mittleren Breiten mithilfe eines flugzeuggetragenen Lidars charakterisiert und auf einen indirekten Effekt hin untersucht. Basierend auf deren optischen Eigenschaften werden zwei Gruppen von Wolken identifiziert. Sie formen zwei Moden in ihrem Partikel-Depolarisationsverhältnis bei $\delta^{part} = 0.4$ und $\delta^{part} = 0.5$. Dies weist auf eine grundlegend unterschiedliche Wolkenmikrophysik beider Gruppen hin. Die erhöhten Depolarisationsverhältnisse der einen Gruppe werden mit dem indirekten Flugverkehrseffekt in Verbindung gebracht. Andere mögliche Einflussfaktoren werden ausgeschlossen. Dies gestattet erste Einblicke in den indirekten Effekt.

Wolken in der beeinflussten Gruppe weisen geringere Eisübersättigungen, größere Kristalldurchmesser und niedrigere Anzahlkonzentrationen auf. All das kann als Auswirkung heterogenen Gefrierens an Flugzeug-Abgaspartikeln interpretiert werden. Die einzelnen Wolken sind großflächig und in ihrer Gesamtheit betroffen. Ihr häufiges Auftreten und ihre ungewisse, aber potentiell große Klimawirkung verlangt nach weitergehenden Untersuchungen. Aus den Ergebnissen dieser Arbeit werden Messstrategien abgeleitet, welche zukünftig helfen werden, weitere Beobachtungsbelege zu sammeln. Diese sollten sich auf Nukleationsgebiete in Luftfahrtsregionen und in unbelasteter Luft konzentrieren.

Abstract

In view of global warming, science is prompted with the task to investigate all potential impacts on climate. Cirrus clouds that consist of small ice crystals exhibit a considerable climate impact due to their large extent. They lead to high uncertainties in climate prediction, as it is unclear how their impact is modified in a changing climate and by anthropogenic activities.

The evermore growing air traffic causes the formation of condensation trails that can persist for long times under suitable conditions and add to the general cirrus cover. Besides this direct effect from aviation, the concept of an indirect effect on natural cirrus clouds has been proposed decades ago. Several modeling studies have investigated this indirect effect, where aircraft exhaust particles contribute to the background aerosol load in the upper troposphere and act as ice nuclei during natural cirrus formation. Yet, it has not been verified in field studies until now. Model estimations of the radiative forcing, delivered contradicting results from no significant effect to a range of $-350\,\mathrm{mW\,m^{-2}}$ to $90\,\mathrm{mW\,m^{-2}}$. These uncertainties stem from the absence of observational evidence that is needed to specify the relevant model scenarios.

In this work northern hemisphere midlatitude cirrus clouds are characterized by an airborne lidar and investigated in the context of an indirect effect. Two groups of clouds are identified based on their optical properties. They form two modes in their particle depolarization ratio at $\delta^{part} = 0.4$ and $\delta^{part} = 0.5$. This indicates fundamental differences in the cloud microphysics of both groups. The group with elevated depolarization ratios is associated with the indirect aviation effect. Other possible influences are excluded. This allows first insights into the indirect effect.

Clouds in the affected group show lower ice supersaturations, larger particle sizes and lower number concentrations. All this can be interpreted as the traces of heterogeneous freezing due to aircraft exhausts. Whole clouds are affected on a large scale. Their frequent occurrence and their unclear but potentially large climatic impact demands further investigations. From the results of this work, measurement strategies are deduced that will help to gather further observational evidence in future. They should focus on nucleation areas in air traffic and unpolluted regions.

Publications

Parts of the results presented in this thesis have been published in the following two peer-reviewed articles:

- **Determining stages of cirrus evolution: a cloud classification scheme** (2017),
  Benedikt Urbanek, Silke Groß, Andreas Schäfler, and Martin Wirth,
  Atmospheric Measurement Techniques, 10, 1653, doi: 10.5194/amt-10-1653-2017

  Benedikt Urbanek conceived and developed the classification scheme, applied it to the case study and took the lead in writing the manuscript. Silke Groß supervised the findings of this work and encouraged Benedikt Urbanek to investigate the specific cirrus cloud chosen for the case study. Andreas Schäfler helped interpreting the meteorologic situation in which the cirrus case formed. Martin Wirth processed the raw lidar data. All authors discussed the results and contributed to the final version of the manuscript.

- **High Depolarization Ratios of Naturally Occurring Cirrus Clouds Near Air Traffic Regions Over Europe** (2018),
  Benedikt Urbanek, Silke Groß, Martin Wirth, Christian Rolf, Martina Krämer, and Christiane Voigt,
  Geophysical Research Letters, 45, 10, doi: 10.1029/2018GL079345

  Benedikt Urbanek prepared and performed the statistical data analysis including all data visualization and wrote the article with inputs from all authors. Silke Groß closely supervised the investigations. Martin Wirth processed the raw lidar data and helped with all measurement related questions. Christian Rolf and Martina Krämer provided trajectory calculations and discussed the results. Christiane Voigt is one of the principal investigators of ML-CIRRUS and discussed the results.

Contents

Chapter 1

Introduction

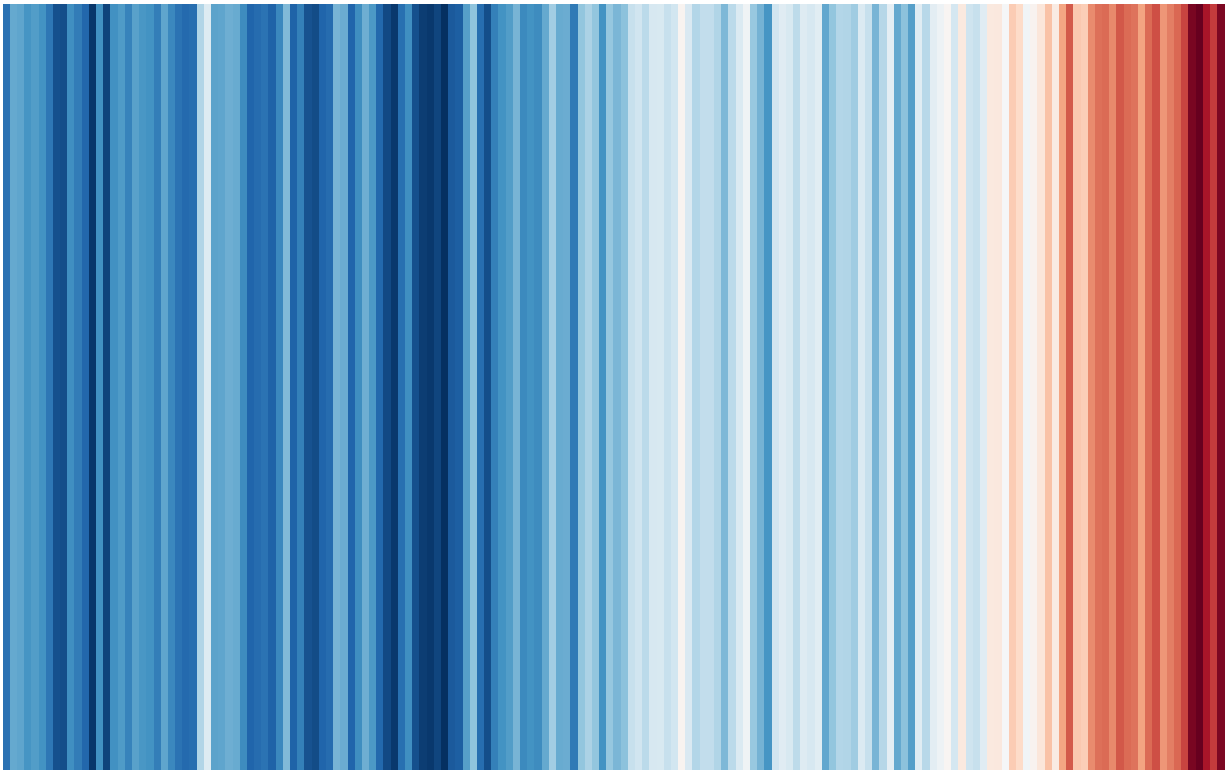

Figure 1.1: "Warming stripes": Annual global temperatures from 1850-2019. The color scale represents the change in global temperatures covering 1.35 °C. Reproduced after *Hawkins* (2018).

Ed Hawkins, a Climate scientist in the National Centre for Atmospheric Science (NCAS) at the University of Reading and a Contributing Author to the Fifth Assessment Report of the Intergovernmental Panel on Climate Change (IPCC AR5), published an illustration

of global temperature change over the last 170 years, called "Warming stripes", in May 2018.

This visualization highlights *"how we have witnessed temperature change across the globe over the past century or more. The colour of each stripe represents the temperature of a single year, ordered by the earliest available data [...] to now. All other superfluous information is removed so that the changes in temperature are seen simply and undeniably"* (*Hawkins*, 2018).

"Warming stripes" excited vast resonance in many people, not only in the scientific community, that appreciate its visual appeal and strong message. This pattern is so popular that people want to wear it on their bodies in form of self knitted sweaters, flip-flops, tights, scarfs, leggings, ties, and t-shirts or print it on anything from coffee mugs to electric cars.

The rising awareness of the need for humanity to change its way of living in order to bring the warming trend to a halt also shows itself in movements like "school strike for climate" (also known as "Fridays For Future") where - inspired by the example of Swedish school girl Greta Thunberg - students all over the world have been attending school strikes each Friday since August 2018 to protest for immediate measures to combat climate change. Parents and teachers have joined their protest.

These calls for action are based on a robust body of scientific evidence that documents temperature change and the responsibility of human activities for a large part of it. Science has developed a good understanding of climate change and its causes and is working to comprehend all possible impacts that may affect human life today and in future (*National Research Council*, 2010).

1.1 Cirrus clouds and climate

Cirrus clouds consist of ice crystals. Their size can range from below 10 µm to more than a few millimeter (*Baran*, 2012). These crystals exist in an abundance of shapes that comprises hexagonal plates, columns, needles, bullet rosettes and more. Laboratory freezing experiments and field study findings showed that the temperature and humidity during the formation process determines the resulting crystal shape (see Figure 1.2). Columnar ice particles are found at temperatures below −40 °C, plate-like particles are found above this temperature. High ice supersaturation leads to complex crystals like rosettes or crossed plates whereas lower supersaturation produces more basic shapes.

Sassen et al. (2008) derived the global distribution for the frequency of occurrence of cirrus clouds from combined radar and lidar measurements from the satellites CALIPSO (Cloud-Aerosol Lidar and Infrared Pathfinder Satellite Observations) and CloudSat (Figure 1.3). The highest cirrus coverage with up to ∼60 % is found in the tropics (±15° latitude) over the equatorial land masses of South America, western Africa, and Indonesia, as well as over the western Pacific Ocean. Northern and southern midlatitude storm tracks feature lesser occurrence frequencies of up to ∼30 %. Minima in cirrus cloud cover are found in the polar regions and between 15° and 30° latitude. The average global cirrus cloud cover was determined at ∼30 % (*Wylie and Menzel*, 1999; *Stubenrauch, Chédin, Rädel, Scott,*

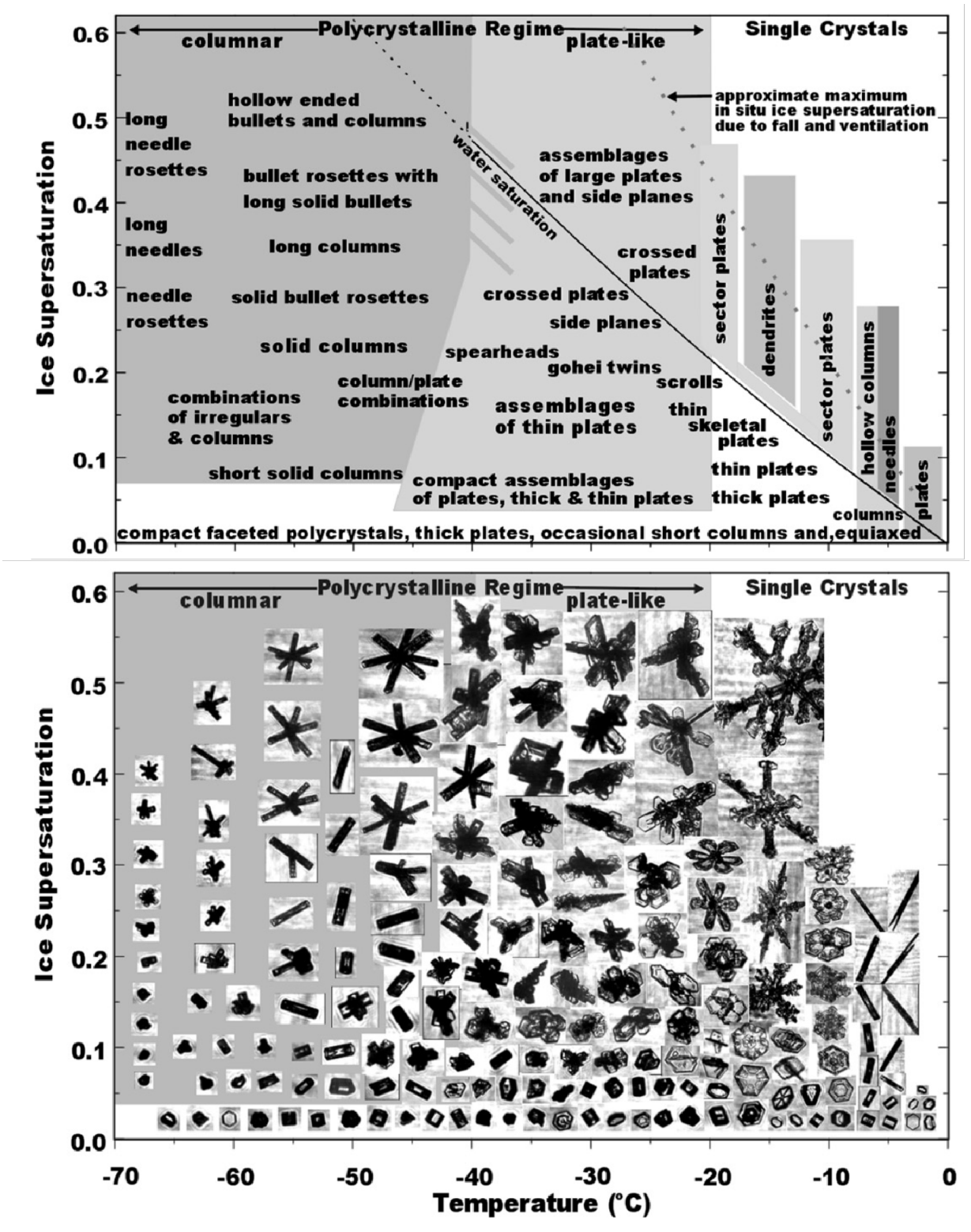

Figure 1.2: Chart of atmospheric ice crystal habit in text format and with example images. It was determined from laboratory experiments and field study results. Taken from *Bailey and Hallett* (2009, their Figure 5).

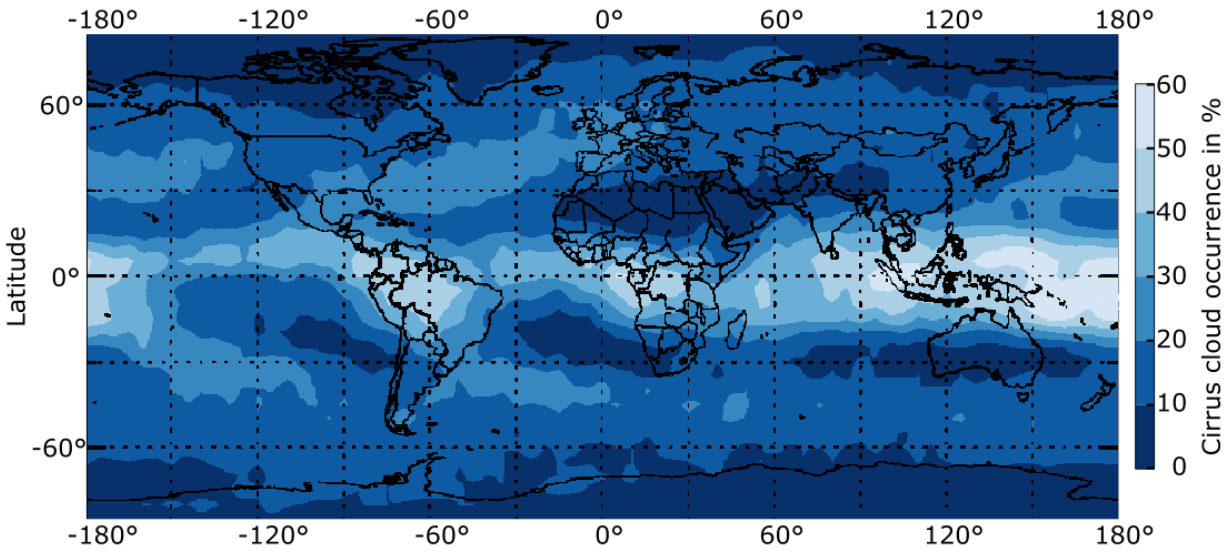

Figure 1.3: Annual global occurrence frequency of cirrus clouds derived from joined radar lidar measurements from the CloudSat and CALIPSO satellites. Reproduced with adapted color scheme from *Sassen et al.* (2008, their Figure 1).

and Serrar, 2006).

Due to their frequent occurrence, cirrus play a considerable role in Earth's radiative budget. They reflect parts of the solar radiation back to space which can cause the Earth's surface to cool. The amount of reflected and transmitted radiation depends on crystal shape, surface roughness and particle orientation (*Liou*, 1986; *Wielicki et al.*, 1995; *Wendisch et al.*, 2007; *Yi et al.*, 2013). As cirrus clouds are typically high and cold, they only emit little long-wave radiation into space, and thus also cause a trapping of radiative energy in the Earth-atmosphere system, which can eventually contribute to a rising surface temperature.

In order to assess the balance between the amount of solar radiation that is absorbed by the Earth and the amount of terrestrial thermal radiation that is emitted, the energy flux at the top-of-atmosphere (TOA) is considered. Figure 1.4 shows the annual average net radiative effect from cirrus clouds at TOA. For this climate simulation, *Gasparini et al.* (2017) used a general circulation model (ECHAM6-HAM2). The radiative effect tends to be stronger over landmasses than over oceans. Around the equator over the east Pacific Ocean, cirrus even show a weak net cooling effect. In a global average, cirrus clouds are expected to have net warming effect on the Earth-atmosphere system.

Whether the net effect of a particular cirrus cloud is warming or cooling is governed by atmospheric and Earth surface parameters as well as cloud properties: ice crystal number concentration, particle size and shape (*Liou*, 1986; *Stephens et al.*, 1990; *Zhang et al.*, 1999; *Gallagher et al.*, 2012; *Schnaiter et al.*, 2016).

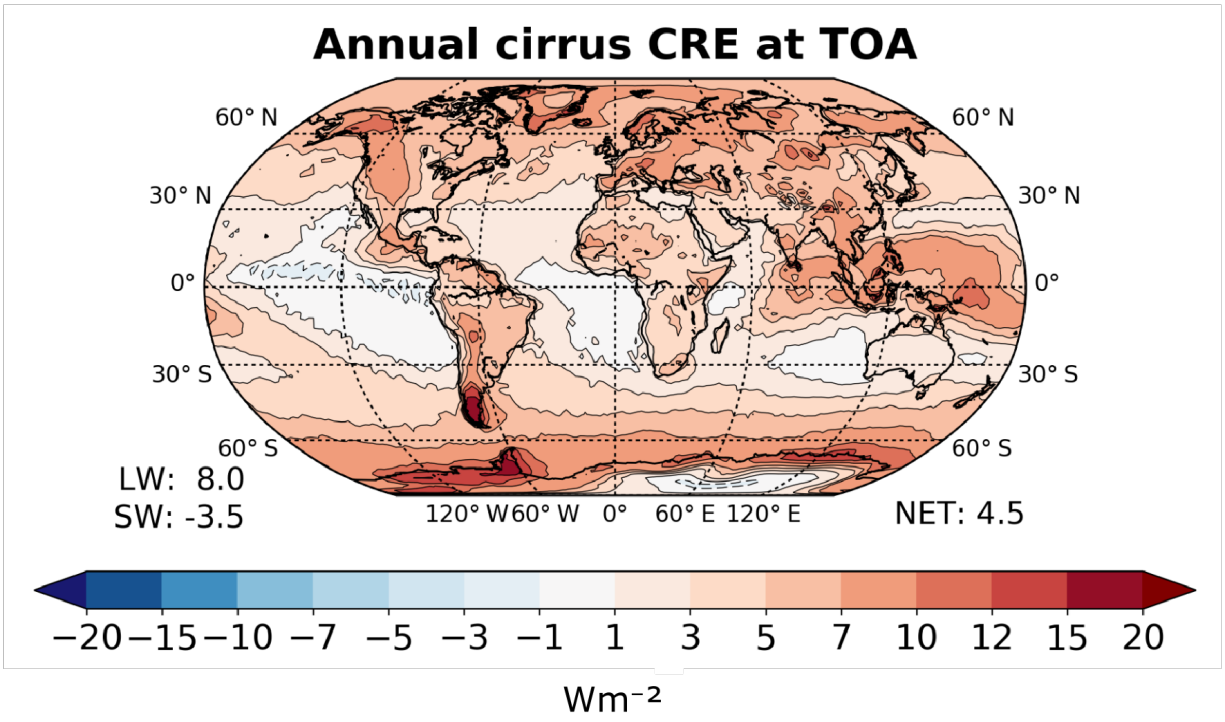

Figure 1.4: Simulated cirrus net radiative effect (CRE) at the top of the atmosphere (TOA). Taken from *Gasparini et al.* (2017, their Figure 3)

Recent studies have investigated factors that affect these properties: The amount and composition of natural and anthropogenic aerosol particles in the troposphere and their ability to nucleate ice crystals are determining details of heterogeneous freezing (*DeMott et al.*, 2010), but aerosol distributions and properties are not well known until today, in particular in the temperature range of cirrus clouds. For example, it remains unclear how aviation exhaust soot particles emitted in the upper troposphere influences natural cirrus clouds (see section 1.2). Exact freezing conditions and mechanisms were studied by *Cziczo et al.* (2013) from in-situ measurements taken during flight campaigns conducted in Middle and North America. They found a dominance of heterogeneous freezing with mineral dust and metallic particles as the main source of residual particles. Although they managed to span a range of geographic regions and seasons, it is not clear, if those results are globally valid.

Sublimation of ice crystals was reported to result in the disappearance of facets and corners, changing the crystal symmetry (*Korolev and Isaac*, 2006). The dependence of freezing on the updraft velocity during cloud formation is theoretically known (*Kärcher and Lohmann*, 2002), but measurements are difficult and rare. In idealized settings, there is also a good understanding of the relevant processes in cloud formation and break up. But in nature no two clouds are alike and there exists a confusing variability of conditions under which they occur. This makes it difficult to represent cirrus clouds adequately in global circulation models for weather and climate prediction (*Baran*, 2012; *Zhang*, 2005).

1.2 Anthropogenic influence on cirrus clouds

Global mobility is gaining an increasing importance in human society. As a consequence, air traffic volume showed annual growth rates of more than 4% in the last years and is predicted to do so in the coming decades (International Civil Aviation Organization (ICAO) *'Long-Term Traffic Forecasts'*, 2016). This leaves geosciences with the urgent task to quantify the numerous aviation impacts on climate (*Lee et al.*, 2009).

Radiative forcing (RF) results from direct engine emissions in the upper troposphere (*Lund et al.*, 2017) and from contrails that form under suitable conditions (*Burkhardt et al.*, 2010). Observations from 1975 to 1995 showed a significant increase in cirrus cover over northern Oceans and the United States. *Minnis et al.* (2004) concluded that this trend is most likely caused by persisting linear contrails that spread horizontally and form so called contrail cirrus. This effect amplifies the impact of aviation on the cirrus cover. In the last years, a lot of research effort has been dedicated to measuring and understanding contrails (*Heymsfield et al.*, 2010; *Voigt et al.*, 2011; *Iwabuchi et al.*, 2012; *Kärcher et al.*, 2015; *Schumann et al.*, 2017) and to determining the climatic effect that arises from their increasing occurrence (*Burkhardt and Kärcher*, 2011).

Contrails also alter the properties of cirrus clouds. *Tesche et al.* (2016) studied contrail formation in pre-existing cirrus. They analyzed satellite lidar measurements and could show that embedded contrails cause an increase in cloud optical thickness inside individual flight tracks compared to adjacent parts of the cloud.

The total RF from contrails is small compared to that of natural ice clouds. Therefore, indirect aviation effects that alter the properties of natural cirrus can potentially have a comparably high climatic impact. *Jensen and Toon* (1997) suggested already two decades ago that aircraft exhaust particles may act as efficient ice nuclei, leading to more heterogeneous freezing in polluted regions. A number of modeling studies simulated this indirect aerosol effect: *Jensen and Toon* (1997) themselves suggested that as a result of heterogeneous freezing, the ice crystal number density in affected clouds should be reduced and that the crystals would probably grow larger. Later, *Hendricks et al.* (2005) concluded from their simulations that at northern midlatitudes, ice crystal number concentrations could be changed significantly by cloud modifications induced by aviation black carbon (BC). And *Kärcher et al.* (2007) proposed two principle scenarios: The first contains high concentrations of original soot emissions that could increase ice crystal number slightly. The second comprises low concentrations of particles that were formed by coagulation of emitted soot with background aerosols and could significantly reduce the ice crystal number. Later, studies determined estimations of the radiative impact but provided contradicting results that range from no statistical effect to a range between $-0.35\,\mathrm{W\,m^{-2}}$ and $0.09\,\mathrm{W\,m^{-2}}$ (*Gettelman and Chen*, 2013; *Zhou and Penner*, 2014). In the $-0.35\,\mathrm{W\,m^{-2}}$ scenario, the radiative forcing from aviation ($90\,\mathrm{mW\,m^{-2}}$ not including indirect effects (*Kärcher*, 2018)) would be compensated almost four times, in the $0.09\,\mathrm{W\,m^{-2}}$ scenario the forcing would double. These studies suffer from huge uncertainties that stem from a lack of field observations that could help restrict model scenarios. Still, this effect may potentially alter cirrus properties in large areas of the globe and therefore could cause RF that exceed that of contrails.

To my knowledge, only two field campaign studies tried to investigate this indirect effect. *Ström and Ohlsson* (1998) examined airborne in-situ measurements and found increased ice crystal number densities in confined regions inside cirrus clouds that also showed elevated black carbon concentrations. This was confirmed by *Kristensson et al.* (2000). They found reduced effective ice diameters and therefore increased number densities during the same campaign. However, it remained unclear whether their observations were caused by the indirect aerosol effect. The results agree better with more recent findings that found higher number densities of small ice crystals in contrail cirrus compared to natural cirrus (*Voigt et al.*, 2017). Therefore, from today's stand point there is reason to assume that these early observations show traces of a direct aviation effect from contrails.

1.3 Atmospheric lidar for cirrus studies

Already early in the development of lidar systems, they have been used to measure cirrus cloud top and base height. Today more advanced techniques exist. Airborne lidar systems can provide two-dimensional cross-sections through cirrus at high spacial resolutions and are therefore a valuable tool to study the macrophysical extent and the fine structure of cirrus clouds (*Groß et al.*, 2014). Combining water vapor differential absorption lidar measurements with temperature information from measurements or models enables the

study of relative humidity and supersaturation in and outside of cirrus clouds. They are decisive variables in nucleation, growth and sublimation of ice crystals (*Heymsfield and Miloshevich*, 1995).

Polarization sensitive lidar systems provide measurements of depolarization ratio which is a key variable for characterizing cirrus properties (*Sassen*, 1991), and is used to derive microphysical properties (*Sassen and Benson*, 2001; *Noel et al.*, 2002, 2006; *Schnaiter et al.*, 2012). When linearly polarized light is scattered by atmospheric ice crystals, reflections at internal facets can lead to skew ray paths that result in a change of polarization. The strength of this effect can be evaluated by analyzing the backscattered light, splitting it into the polarization components perpendicular and parallel to the incident light. The depolarization ratio is defined as the power ratio of both components and therefore mainly determined by the precise crystal shape (see section 2.1.3). A satellite based study determined a global averaged depolarization ratio of 35 % for cirrus clouds (*Sassen and Zhu*, 2009). With the access to relative humidity and depolarization ratio, advanced airborne lidar systems are important tools to efficiently observe and study cirrus clouds.

1.4 Objective and structure of this thesis

The objective of this work is to find observational evidence of an indirect aerosol effect from aviation on natural cirrus clouds. Modeling studies investigating this effect found contradicting results concerning the impact on cirrus clouds and climate. In order to decrease these uncertainties, atmospheric observations of the effect are needed that can specify appropriate modeling scenarios.

For that, measurements from the lidar system WALES (derived from WAter vapor Lidar Experiment in Space, (*Esselborn et al.*, 2008; *Wirth et al.*, 2009)) that was employed during the ML-CIRRUS campaign (midlatitude cirrus experiment (*Voigt et al.*, 2017)) over Europe are assessed. WALES gives access to measurements of humidity and depolarization ratio. Humidity is a decisive factor regarding ice formation and sublimation (*Heymsfield and Miloshevich*, 1995) and depolarization ratio is linked to ice microphysics. Lidar data and insitu measurements of ice crystal size and number concentration are analyzed with the aim to answer the following research questions:

RQ1: Can features in optical cirrus properties be associated with an indirect aerosol effect from aviation?

RQ2: How are ice supersaturation and microphysical properties modified in affected clouds?

To approach these questions, first the cirrus cloud cases of ML-CIRRUS are characterized. The airborne lidar data allows to efficiently observe whole cloud cross-sections. Then, distinct features in cloud depolarization ratio are correlated to their origin in air traffic regions. Further, humidity and in-situ measurements that were taken in these cirrus cases are investigated for traces of the indirect aerosol effect. Finally other possible

influences like cloud evolution, cloud formation in a specific meteorological situation, or the existence of embedded contrails are examined and excluded.

To identify regions of ice nucleation, depositional growth and sublimation within measured lidar cross-sections of cirrus clouds, a classification scheme is developed and applied during this doctoral thesis. It is used to investigate the influence of cloud evolution on the depolarization ratio.

The atmospheric lidar techniques, WALES is based on, are described theoretically in chapter 2.1. The objectives, flight strategy and instrumentation of the ML-CIRRUS campaign are presented in section 2.2, and the classification scheme is discussed in section 2.3.

The characterization of cirrus clouds measured during the campaign comprises three parts (section 3.1). First, a detailed case study of a cirrus clouds impacted by gravity waves in the lee of the Pyrenees introduces all variables measured by WALES and demonstrates the applicability of the classification scheme (section 3.1.1). Then the statistical analysis of relative humidity and classified evolution stages in section 3.1.2 reveals differences and common features between the cloud cases. Finally in section 3.1.3 several features of depolarization ratio distributions are investigated.

In section 3.2 the results of the cirrus characterization are investigated in the context of the research questions, regarding the origin of clouds in air traffic regions (section 3.2.1), humidity distributions (section 3.2.2) and in-situ measurements of size and concentration (section 3.2.3). Other possible influences are examined in section 3.2.4 to exclude their impact on the observed differences in the clouds.

In Chapter 4, the findings are put into a broader context of previous studies. I discuss probable types of soot and the potential climate impact of the indirect aerosol effect. Further, a set of requirements for future flight missions is proposed that might enable proceeding examinations of the indirect aerosol effect from aviation exhausts. Finally, conclusions are drawn in Chapter 5.

1.5 Data sources

While carrying out this study, contributions from several persons were brought together. They are summarized below. Christiane Voigt, Ulrich Schumann and Andreas Minikin were the principal investigators of ML-CIRRUS and over 50 scientists worked together to make this campaign a success.

- The WALES lidar system was maintained and operated by Martin Wirth, Silke Groß and Andreas Fix. The analysis of WALES data makes up the core of this work.

- Backward trajectory data of measured air masses were provided by Christian Rolf and Martina Krämer. I use them to identify the origin of cirrus clouds (section 3.2.1).

- In-situ measurements of particle size and concentration during ML-CIRRUS was provided by Tina Jurkat-Witschas and Christiane Voigt. I analyze them in the context of an indirect aerosol effect in section 3.2.3.

- The Contrail Cirrus Prediction Tool (CoCiP) was developed by Ulrich Schumann. He compiled Contrail simulations for all ML-CIRRUS flight missions based on the actual air traffic in the time period and provided simulation data interpolated to the lidar cross-sections. I use them to verify the existence of contrails in investigated lidar data (section 3.2.4).
- Mattia Righi and Johannes Hendricks engaged in a preliminary modeling of the impact of aviation emissions. They performed the simulation and provided the calculated aerosol impact for individual cirrus cases discussed in section 4.2.1.

Chapter 2

Methods

In this chapter, basic and advanced lidar techniques are described (section 2.1). They are employed in the airborne Laser system WALES. The results of this thesis are based on measurements of cirrus clouds taken with WALES during the ML-CIRRUS flight campaign in 2014. A description of the campaign, the lidar system and in-situ instrumentation employed during ML-CIRRUS is given in section 2.2. A thermodynamic classification scheme that identifies the evolution stage of cloud parts was developed and is presented in section 2.3.

2.1 Atmospheric lidar techniques

Soon after the invention of the laser, as a highly coherent light source (*Maiman*, 1960), its application in meteorology in radar-type instruments was discussed (*Goyer and Watson*, 1963). These instruments were given the name lidar. The word is either used as a combination of light and radar or as an acronym of light detection and ranging (compare its use in (*Goyer and Watson*, 1963; *Collis and Ligda*, 1964; *Collis*, 1965; *Northend et al.*, 1966)).

Within the next two decades, pioneering work that still forms the basis of today's atmospheric lidar research has been accomplished, such as first observations of water and ice clouds from ground based and airborne lidars (*Collis*, 1965; *Davis*, 1969, 1971), or the successful development and application of water vapor differential absorption lidars and high spectral resolution lidars (*Browell et al.*, 1979; *Maddrea and Bendura*, 1981; *Baker*, 1983; *Shipley et al.*, 1983).

Today lidar instruments are valuable tools used in all branches of atmospheric science from monitoring green house gas emissions, deriving temperature profiles, investigating clouds, classifying aerosols, to measuring wind. They are employed on land, aboard ships, planes, and satellites.

2.1.1 Basic lidar setup and the lidar equation

A basic lidar system contains a laser that emits short light pulses along a collimated beam into the atmosphere and a telescope with subsequent data acquisition for time-resolved measurement of the fraction of light that gets scattered back to the instrument, e.g. by atmospheric molecules or aerosols (Figure 2.1). For that, the laser beam is aligned with the optical axis of the telescope. From the difference between the time of pulse emission t_0 and the time at which the backscattered light is recorded t, and the speed of light c, the distance r at which the scattering occurred can be determined:

$$r = \frac{c(t - t_0)}{2}. \tag{2.1}$$

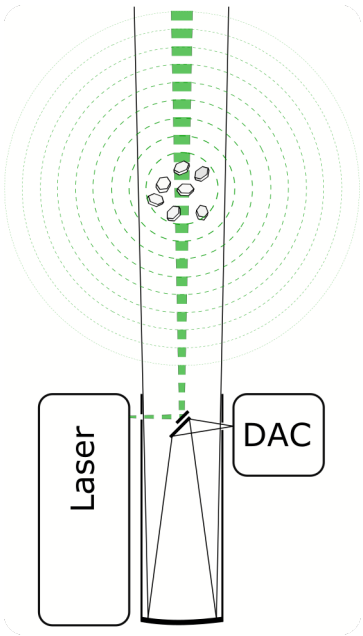

Figure 2.1: Schematic of a basic lidar setup. Laser pulses are sent into the atmosphere where gas molecules, aerosols, cloud particles, etc. cause scattering. Backscattered light is received by a telescope and detected and recorded by a data acquisition module (DAC).

For a single-wavelength setup, the lidar equation that connects the measured power to atmospheric extinction and scattering processes can be given as:

$$P(r) = P_0 \frac{c\tau}{2} A \Omega_{FOV} \frac{\beta(r)}{r^2} e^{-2\int_0^r \alpha(r')dr'}. \tag{2.2}$$

Here, $P(r)$ is the instantaneous received power from range r, P_0 is the transmitted power at time t_0, τ the pulse duration, A the system receiving area, Ω_{FOV} the receiver field of view, and $\beta(r)$ and $\alpha(r)$ the atmospheric backscatter and extinction coefficient of the measured air volume at range r for the given operation wavelength.

The following description is based on the approach taken by *Eloranta* (2005). The backscatter coefficient comprises the components from molecular scattering β^{mol} and from particulate scattering β^{part}:

$$\beta = \beta^{mol} + \beta^{part}. \tag{2.3}$$

Atmospheric extinction arises from scattering and absorption of light both by molecules and particles. Thus the extinction coefficient can be expressed as:

$$\alpha = \alpha^{mol}_{sca} + \alpha^{mol}_{abs} + \alpha^{part}_{sca} + \alpha^{part}_{abs}. \tag{2.4}$$

In most situations α^{mol}_{abs} can be assumed to be zero, as operation wavelengths are typically chosen to fall within atmospheric windows where no molecular absorption takes place. Equation (2.2) then can be written as:

$$P(r) = P_0 \frac{\tau c}{2} A \Omega_{FOV} \frac{\beta^{mol} + \beta^{part}}{r^2} e^{-2\int_0^r \alpha^{mol}_{sca}(r') + \alpha^{part}_{sca}(r') + \alpha^{part}_{abs}(r') dr'}. \tag{2.5}$$

The molecular coefficients β^{mol} and α^{mol}_{sca} are determined by Rayleigh scattering and can be calculated if information on the concentration of molecules is available, e.g. from atmospheric pressure and temperature profiles. They are linked by the molecular lidar ratio

$$L^{mol} = \frac{\alpha^{mol}_{sca}}{\beta^{mol}} = \frac{\int^{4\pi} \mathbb{P}(\theta) d\Omega}{\mathbb{P}(\theta)|_{\theta=\pi}} = \frac{8\pi}{3} sr \tag{2.6}$$

that can be derived from the Rayleigh phase function $\mathbb{P}(\theta) = \frac{3}{16\pi}[1 + cos^2\theta]$. Here θ is the scattering angle and Ω a solid angle.

The particle coefficients β^{part}, α^{part}_{sca}, and α^{part}_{abs} are related to one another. For homogeneous particles (not always the case), these relations are determined by particle size, shape, and refractive index. In practical measurement situations all this information oftentimes is not accessible. Therefore α^{part}_{sca} and α^{part}_{abs} are considered together as one unknown $\alpha^{part} = \alpha^{part}_{sca} + \alpha^{part}_{abs}$, and β^{part} as the other.

This leaves two unknown physical quantities β^{part} and α^{part} in equation 2.5, which makes it still under-determined. When assuming a proportionality between those two in the form of a fixed particle lidar ratio ($\alpha^{part} = L^{part}\beta^{part}$), the number of unknowns is reduced to one and the equation can be solved (*Klett*, 1981). However, the strong variability of atmospheric particles can destroy this assumed proportionality, limiting the applicability of this method. For example, L^{part} shows values of ∼20 sr for marine aerosol, ∼45 sr for urban haze, ∼50 sr for forest fire smoke and ∼60 sr for Saharan desert dust (*Müller et al.*, 2007).

Another approach for solving equation 2.5 is to measure two lidar profiles in one of which $\beta^{part} = 0$. This is done in Raman lidar and High Spectral Resolution Lidar (HSRL) technology. In the case of Raman lidars, the in-elastic lidar return is caused by Raman scattering by oxygen and nitrogen molecules and can be measured in the corresponding frequency-shifted spectral range. Therefore it is only affected by α^{part}. The elastic lidar return is affected by β^{part} and α^{part}. This produces two equations with two unknowns that can be solved. A detailed description of Raman lidar theory can be found in (*Ansmann et al.*, 1992). In this work, the second option, HSRL, is used.

2.1.2 High Spectral Resolution Lidar

The High Spectral Resolution Lidar technique overcomes the drawbacks of simple elastic backscatter lidars by resolving the different spectral broadening of the molecular and particle lidar return. At a given temperature, molecules are considerably faster in terms of their root-mean-square speed, than the much heavier aerosol and cloud particles. Therefore the molecular scattering return is Doppler broadened and the particle scattering return is nearly line shaped (see Figure 2.2).

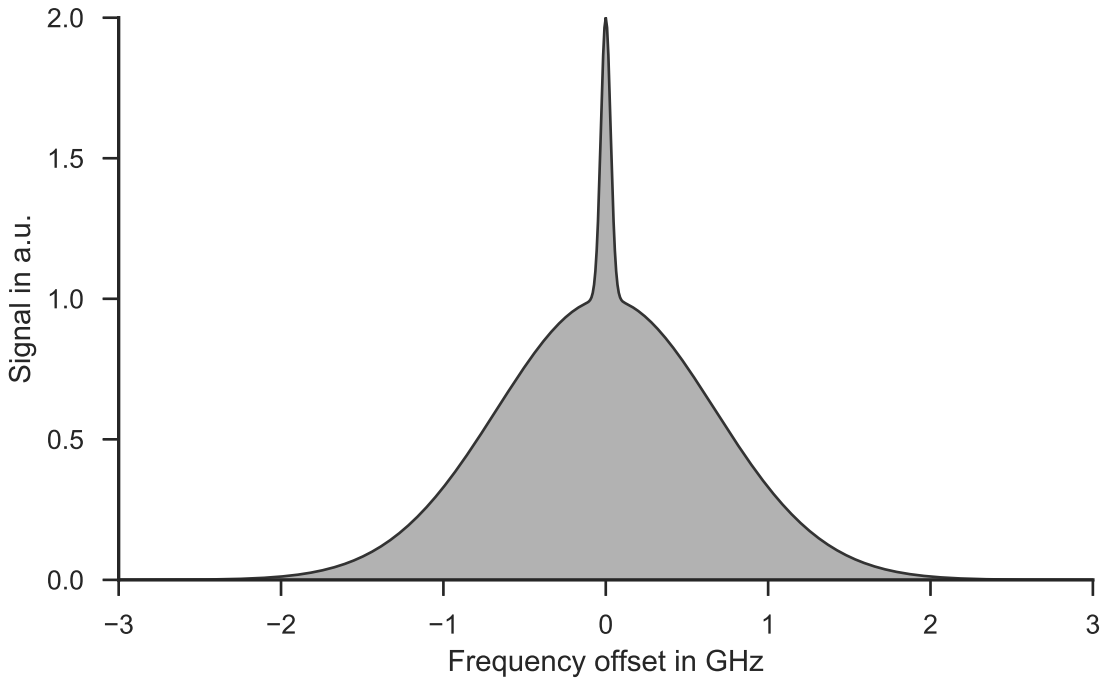

Figure 2.2: Idealized lidar return (532 nm) from a mixture of molecules and particles at a temperature of 220 K

By applying narrow band-pass filters, light scattered by molecules and light scattered by particles can be separated. The two corresponding lidar equations are

$$P^{part}(r) = C^* \frac{\beta^{part}}{r^2} e^{-2\int_0^r \alpha^{mol}+\alpha^{part}dr'} \tag{2.7}$$

and

$$P^{mol}(r) = C \frac{\beta^{mol}}{r^2} e^{-2\int_0^r \alpha^{mol}+\alpha^{part}dr'}. \tag{2.8}$$

Here, the system parameters are summarized in C and C^* that are generally not the same in both channels and must be determined for the given lidar system beforehand. The transmission part $e^{-2\int \alpha_{mol}+\alpha_{part}dr'}$ does not depend on the scattering process at range r

and therefore cancels out, when solving these equations for β_{part}:

$$\beta^{part}(r) = \beta^{mol}(r)\frac{C}{C^*}\frac{P^{part}(r)}{P^{mol}(r)} \tag{2.9}$$

The separation of the molecular and particle contribution requires narrow filtering ($\sim$1 GHz) and locking of the emitted laser to the center frequency of the filter. This is technically demanding but it results in strong signals that allow operation in daylight, where high background light levels render other advanced techniques such as Raman lidars unusable (*Eloranta*, 2005). This makes HSRL lidars suitable for the use aboard air planes.

The backscatter ratio $\mathbb{R}$ is defined as the ratio of the total backscatter coefficient to the molecular backscatter coefficient:

$$\mathbb{R} = \frac{\beta^{mol} + \beta^{part}}{\beta^{mol}} \tag{2.10}$$

2.1.3 Depolarization lidar

When the emitted laser light is scattered by spherical particles such as water droplets, Lorenz-Mie theory predicts that the backscattered light has the same orientation of polarization as the incident light. However, when scattered by cirrus ice crystals, parts of the returning light can exhibit different polarization states. A theoretical understanding of this scattering problem can be derived from Maxwell's equations. However, solving these equations for the given situation is not trivial and depending on the size parameter x, which is the ratio of particle diameter d to wavelength λ ($x = \frac{\pi d}{\lambda}$), different tools and approximations have to be applied.

For $x > 50 - 100$, the approximation of geometric optics and ray tracing methods show that the rotation of the polarization vector stems from skew reflections inside the ice crystal and depends on the crystals shape and complexity (see Figure 2.3). For smaller particles ($x < 50$), tools like the finite time domain method, the discrete dipole approximation, and T-matrix calculations have been applied and revealed large variations of the scattering parameters with changing particle size (*Sassen*, 2005).

The strength of such processes can be evaluated with depolarization lidars that employ polarization optics at their receiver to split the returning light into polarization components parallel and perpendicular to the plane of polarization of the linearly polarized laser. The corresponding lidar equations for both component $P_\parallel$ and $P_\perp$ are

$$P_\parallel = C\frac{\beta_\parallel}{r^2}e^{-2\int_0^r \alpha_\parallel(r')dr'} \tag{2.11}$$

and

$$P_\perp = C\frac{\beta_\perp}{r^2}e^{-2\int_0^r \alpha_\perp(r')dr'}. \tag{2.12}$$

Here, the backscatter and extinction coefficients are split up into the parallel- ($\beta_\parallel$, $\alpha_\parallel$) and cross-polarized ($\beta_\perp$, $\alpha_\perp$) components.

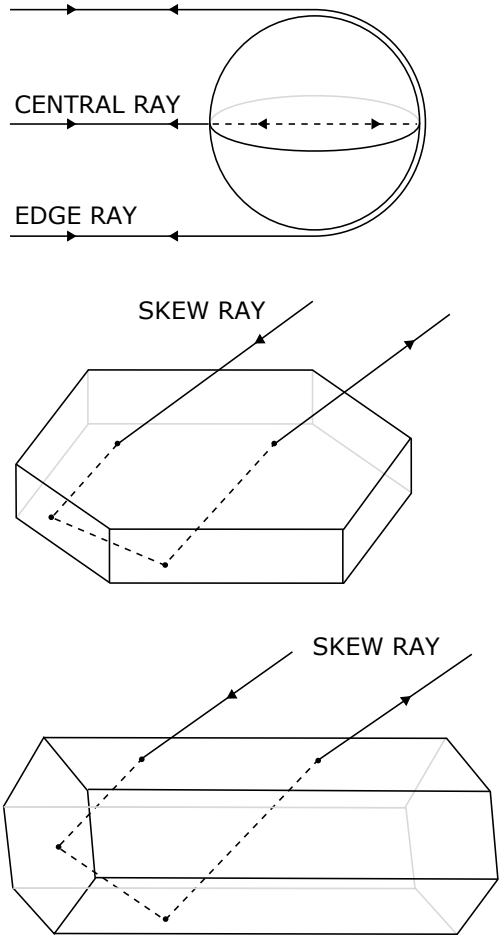

Figure 2.3: Incident and backscattered rays from a spherical drop and idealized hexagonal ice particles (plate and column) in the regime of geometric optics. Reproduced from *Liou and Lahore* (1974, their Fig. 1).

The linear volume depolarization ratio δ^{vol} is defined as the ratio of both power components:

$$\delta^{vol} = \frac{P_{\parallel}}{P_{\perp}} = \frac{\beta_{\parallel}}{\beta_{\perp}} e^{-2\int_0^r \alpha_{\parallel}(r') - \alpha_{\perp}(r') dr'} \approx \frac{\beta_{\parallel}}{\beta_{\perp}}. \tag{2.13}$$

The two polarization components can theoretically experience different transmission through the atmosphere due to anisotropic scatterers such as raindrops or uniformly oriented ice particles. This would lead to deviations in the extinction coefficients ($\alpha_{\parallel} - \alpha_{\perp} \neq 0$). However, such cases seem to be rare and the exponential term is neglected in practice (*Sassen*, 2005).

The particle linear depolarization ratio which characterizes only the scattering properties of particles can be derived by combining HSRL or Raman lidar and depolarization techniques and is defined as:

$$\delta^{part} = \frac{\beta_{\parallel}^{part}}{\beta_{\perp}^{part}}. \tag{2.14}$$

To determine these ratios in practice, the properties of the polarizing optics, typically a polarizing beamsplitter (PBS), and its alignment (φ) with respect to the plane of polarization of the emitted light have to be considered (see Figure 2.4). The following description is based on *Freudenthaler et al.* (2009). The power components parallel (P_p) and perpendicular (P_s) to the plane of incidence of the PBS are

$$\begin{aligned} P_s(\varphi) &= P_{\parallel} sin^2(\varphi) + P_{\perp} cos^2(\varphi), \\ P_p(\varphi) &= P_{\parallel} cos^2(\varphi) + P_{\perp} sin^2(\varphi). \end{aligned} \tag{2.15}$$

These components are reflected and transmitted according to the PBS's reflectances (R_p, R_s) and transmittances (T_p, T_s) and amplified in the two subsequent channels. The signals that are measured and recorded from the reflected (P_R) and transmitted (P_T) channel are

$$\begin{aligned} P_R &= \left[P_p(\varphi) R_p + P_s(\varphi) R_s\right] V_R, \\ P_T &= \left[P_p(\varphi) T_p + P_s(\varphi) T_s\right] V_T. \end{aligned} \tag{2.16}$$

The amplification factors (V_R, V_T) include the optical losses and electronic gain in each channel.

For an alignment of $\varphi = 0°$, δ^{vol} can be given as

$$\delta^{vol} = \frac{P_{\perp}}{P_{\parallel}} = \frac{P_s}{P_p}, \quad \varphi = 0°. \tag{2.17}$$

However, it is desired to reduce cross-talk from the strong parallel-polarized signal onto the weaker cross-polarized signal. As R_s is typically much closer to 1 than T_p for commercial PBS, it is therefore favorable to use an alignment of $\varphi = 90°$:

$$\delta^{vol} = \frac{P_p}{P_s}, \quad \varphi = 90°. \tag{2.18}$$

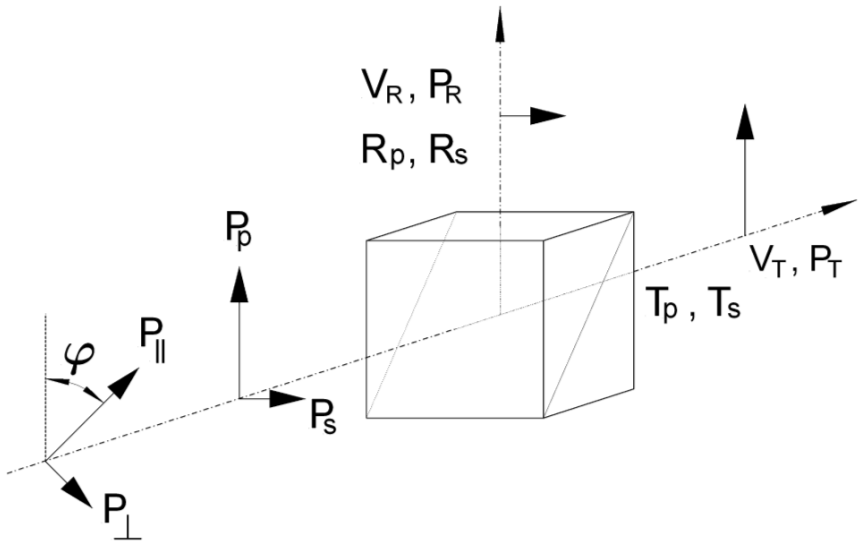

Figure 2.4: Measured power components (P_R and P_T) in the two channels of a polarization sensitive lidar, employing a polarizing beamsplitter cube for linearly polarized radiation parallel (p) and perpendicular (s) to the beamsplitter's plane of incident. The beamsplitter has the reflectances R_p and R_s and the transmittances T_p and T_s. V_R and V_T are the amplification factors of the reflected and transmitted channel, respectively. Taken from *Freudenthaler et al.* (2009, their Figure 1):

After introducing the measured signal ratio δ^* and the relative amplification factor V^* for convenient notation:

$$\delta^* = \frac{P_R(\varphi)}{P_T(\varphi)}, \qquad V^* = \frac{V_R}{V_T}, \tag{2.19}$$

the volume depolarization can be determined as

$$\delta^{vol} = \frac{R_s - \frac{\delta^*}{V^*} T_s}{\frac{\delta^*}{V^*} T_p - R_p}. \tag{2.20}$$

From δ^{vol} and the backscatter ratio $\mathbb{R}$ (see section 2.1.2), an expression for δ^{part} can be derived:

$$\delta^{part} = \frac{(1+\delta^m)\delta^{vol}\mathbb{R} - (1+\delta^{vol})\delta^m}{(1+\delta^m)\mathbb{R} - (1+\delta^{vol})}. \tag{2.21}$$

The linear depolarization ratio of air molecules $\delta^m = \beta^m_\perp / \beta^m_\parallel$ in this equation depends on the temperature of the atmosphere and can be determined with high accuracy (*Behrendt and Nakamura*, 2002).

In order to calibrate the system, V^* has to be determined through calibration measurements. With equations 2.15, 2.16 and 2.19, V^* can be expressed as

$$V^* = \frac{\left[1+\delta^{vol} tan^2(\varphi)\right] T_p + \left[tan^2(\varphi) + \delta^{vol}\right] T_s}{\left[1+\delta^{vol} tan^2(\varphi)\right] R_p + \left[tan^2(\varphi) + \delta^{vol}\right] R_s} \delta^*(\varphi). \tag{2.22}$$

For $\varphi = 0°$, equation 2.22 can be evaluated as

$$V^* = \frac{(T_p + \delta^{vol} T_s))}{(R_p + \delta^{vol} R_s))} \delta^*(0°). \tag{2.23}$$

In this configuration, an aerosol-free section of the lidar profile, where the depolarization stems only from molecular scattering ($\delta^{vol} = \delta^{mol}$), could be used to determine V^*. However, only small amounts of highly depolarizing aerosols in the chosen section would render this calibration useless.

Using $\varphi = 45°$ or $\varphi = -45°$ is more promising. Equation 2.22 turns into

$$V^* = \frac{T_p + T_s}{R_p + R_s} \delta^*(\pm 45°). \tag{2.24}$$

Now, V^* is independent of δ^{vol}. The drawback is that already a small deviation γ from ($\varphi = \pm 45°$) leads to considerable errors.

Freudenthaler et al. (2009) demonstrated an advanced calibration method taking subsequent measurements at $\varphi = +45° + \gamma$ and $\varphi = -45° + \gamma$ flipping the receiver optics by a total of 90°:

$$V^* = \frac{T_p + T_s}{R_p + R_s} \sqrt{\delta^*(+45°) \cdot \delta^*(-45°)}. \tag{2.25}$$

The rotation of 90° can be achieved by mechanical stops at high accuracy, the method is independent of δ^{vol}, and *Freudenthaler et al.* (2009) showed that calibration errors compensate each other very well over a large range of misalignment angles.

2.1.4 Differential absorption lidar

Differential absorption lidar (DIAL) is a valuable lidar technique that is used to measure trace gas concentrations of e.g. water vapor or ozone in the atmosphere. It uses two laser wavelengths. The so called on-line wavelength λ_{on} is located at an absorption line of the target species. The off-line wavelength λ_{off} is located next to the absorption line. The lidar equations for both lines are:

$$P_{on}(r) = P_{0,on} C \frac{\beta(r, \lambda_{on})}{r^2} e^{-2 \int_0^r \alpha(r', \lambda_{on}) dr'} \tag{2.26}$$

and

$$P_{off}(r) = P_{0,off} C^* \frac{\beta(r, \lambda_{off})}{r^2} e^{-2 \int_0^r \alpha(r', \lambda_{off}) dr'}. \tag{2.27}$$

In an ideal DIAL setup, λ_{on} and λ_{off} would be chosen such that the backscatter coefficients are the same:

$$\beta(r, \lambda_{on}) = \beta(r, \lambda_{off}) \tag{2.28}$$

and such that the difference in extinction coefficients, at a given molecule number concentration n^{mol} of the trace gas, stems only from the differences in the molecular absorption cross-section σ, which is well known from laboratory measurements:

$$\Delta\alpha = \alpha(\lambda_{on}) - \alpha(\lambda_{off}) = n^{mol} \left[\sigma(\lambda_{on}) - \sigma(\lambda_{off})\right] = n^{mol} \Delta\sigma. \tag{2.29}$$

With (2.28), equations (2.26) and (2.27) can be combined into the form:

$$ln\left(\frac{P_{on}(r)}{P_{off}(r)}\right) = ln\left(\frac{P_{0,on}C}{P_{0,off}C^*}\right) - 2\int_0^r \Delta\alpha(r)dr'. \tag{2.30}$$

Using (2.29), an expression for the molecule number concentration at range r can be derived:

$$n^{mol}|_r = \frac{1}{2\Delta\sigma}\left[\frac{d}{dr}ln\left(\frac{P_{off}(r)}{P_{on}(r)}\right)\right]. \tag{2.31}$$

From this it is clear that any system fluctuations cancel each other out when forming the lidar return ratio of both wavelengths, finding the logarithm and evaluating the derivative. This self-calibration is one of the main advantages of DIAL (*Gimmestad*, 2005).

2.2 ML-CIRRUS campaign

2.2.1 Objectives and flight strategies

From 21 March to 15 April 2014, the ML-CIRRUS campaign was conducted with the goal to study cirrus in meteorological regimes typical for the midlatitudes, to observe contrail cirrus, and to investigate differences between anthropogenic and natural cirrus. For this, the German High Altitude and Long Range Research Aircraft (HALO) was equipped with a combined in-situ and remote sensing instrumentation including cloud probes, WALES lidar and novel ice residual, aerosol, trace gas, and radiation instruments (*Voigt et al.*, 2017). Flight planning was guided by meteorological forecasts and advanced model predictions of cirrus and contrails (*Schumann*, 2012; *Schumann and Graf*, 2013). The 16 flight missions cover the whole range of the midlatitudes from 36 to 58°N and from the Atlantic Ocean (15°W) to central Europe (15°E) (see Figure 2.5).

During research flights, several legs at different altitudes were combined. The remote sensing instruments measured the clouds during legs well above cirrus top and in-situ instruments directly sampled the air and the aerosol and cloud particles during lower legs at various cloud levels. This way a combined remote sensing and in-situ data set could be compiled for several cirrus clouds.

To investigate a cloud over its life cycle, quasi-Lagrangian measurements along air parcel trajectories were performed. Close coordination with air traffic control centers in Karlsruhe and Shannon enabled flights near and in air traffic corridors. Flights were announced two days in advance and the final flight plans were handed in 24 hours before the flight. Additionally, HALO could freely operate within specific air spaces with temporarily restricted access for general aviation.

Table 2.1 gives an overview of the research missions. The flight date, the cirrus cross-section recorded by lidar, the operation region, the duration, the availability of collocated in-situ and lidar data (see section 2.2.3), and the mission scope are presented. Contrails and contrail cirrus were measured over the North Atlantic Ocean and the European mainland.

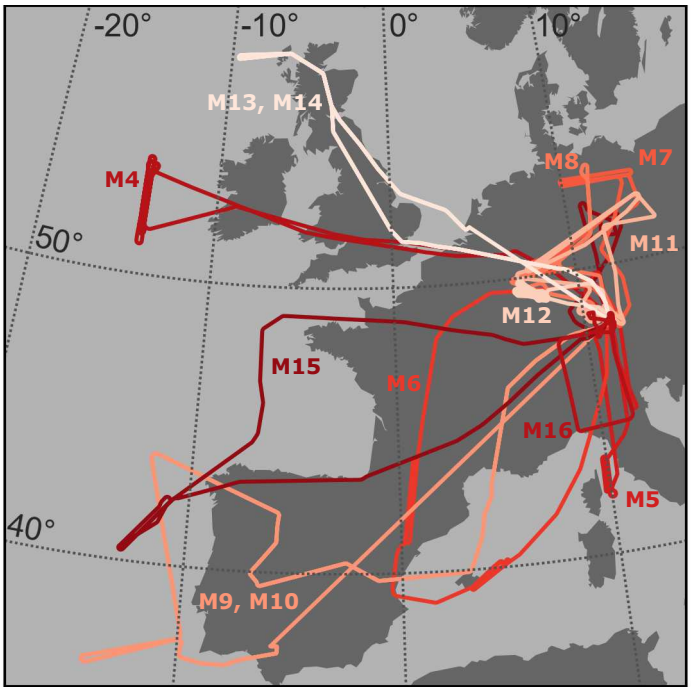

Figure 2.5: Map showing the flight paths of 12 flight missions during ML-CIRRUS covering the midlatitude over Europe from 36 to 58 °N

Cleaner, less polluted cirrus were encountered over Portugal and Spain. Four missions were dedicated to cirrus in frontal ridge systems mainly in the outflow regions of warm conveyor belts. Synoptic and jet-stream induced cirrus were measured over the Atlantic Ocean, the Mediterranean Sea and western Europe, orthographically excited mountain wave cirrus and lee wave cirrus were probed over the Pyrenees and France, and convective cirrus were encountered over the Mediterranean Sea. Further details on the flights, instrumentation, flight planning, and forecast products and selected scientific highlights can be found in the overview article by *Voigt et al.* (2017).

2.2.2 WALES lidar

The HSRL and DIAL lidar system WALES (derived from WAter vapor Lidar Experiment in Space) aboard HALO is capable of measuring backscatter ratio ($\mathbb{R}$) and δ^{part} at 532 nm, with a high vertical resolution. The additional non-HSRL channel at 1064 nm is also polarization sensitive. Water vapor concentrations (r_{H_2O}) are measured by simultaneously emitting laser pulses at three online and one offline wavelength in the water vapor absorption band around 935 nm (*Wirth et al.*, 2009). The partly overlapping range contributions from the three online wavelengths provide the needed sensitivity to compose a complete water vapor profile that ranges from just below the aircraft down to ground level.

The HSRL transmitter utilizes a Nd:YAG laser. The Q-switched master oscillator is seeded by a monolithic Nd:YAG ring laser and three subsequent amplification stages

Table 2.1: Overview of ML-CIRRUS flights. The mission number, date, recorded cirrus lidar cross-section, operation region, flight duration, availability of collocated measurements from CIP/CAS and the mission scope are given. The table was adapted and extended from *Voigt et al.* (2017)

Mission	**Date**	**cirrus lidar cross section**	**Region**	**Duration**	**collocated CIP/CAS data**	**mission scope**
M1-3	21-22 Mar 2014	-	Germany	6 h	-	Intrument test flights
M4	26 Mar 2014	1190 km^2	North Atlantic flight corridor	8 h 30 min	yes	Contrails and contrail cirrus
M5	27 Mar 2014	860 km^2	Alps, Italy, Germany	4 h 45 min	yes	Frontal cirrus, WCB in- and outflow
M6	29 Mat 2014	2880 km^2	France, Spain	7 h 30 min	yes	Lee wave cirrus, WCB, jet stream divergence, convective cirrus
M7	1 Apr 2014	3380 km^2	Germany	6 h 35 min	yes	Cirrus, contrail cirrus
M8	3 Apr 2014	220 km^2	Germany	5 h 15 min	yes	Frontal cirrus, WCB outflow
M9, M10	4 Apr 2014	1230 km^2 910 km^2	Spain, Portugal	9 h 55 min	yes, -	Clean jet stream cirrus, poplluted WCB
M11	7 Apr 2014	2180 km^2	Germany	5 h 35 min	yes	Contrail cirrus, cirrus sublimation, Halo
M12	10 Apr 2014	170 km^2	Germany	3 h 15 min	-	Contrails and contrail cirrus
M13, M14	11 Apr 2014	-, 2540 km^2	Great Britain	10 h	-, yes	Frontal cirrus, large WCB, ridge cirrus
M15	13 Apr 2014	-	France, Spain, Portugal	7 h 15 min	-	High pressure system, jet stream cirrus
M16	15 Apr 2014	-	Alps	3 h	-	Föhn, divergence, gravity wave cirrus

produce pulse energies of >400 mJ at 1064 nm. A temperature stabilized potassium titanyl phosphate (KTP) crystal is employed for frequency-doubling. The 532 nm light has a pulse energy of 220 mJ. A fraction of the frequency-doubled radiation is fed into a frequency stabilizer that is based on acousto-optic modulation and locks the green laser radiation to a Doppler-broadened absorption line of iodine (I_2) by controlling the temperature of the seed laser Nd:YAG crystal. This method ensures the necessary frequency stability even under airborne conditions (*Esselborn et al.*, 2008).

In order to generate the four DIAL wavelengths, a part of the 532 nm radiation is used to pump a optical parametric oscillator (OPO) in a dual-crystal, four mirror ring-oscillator configuration. For the frequency conversion, two KTP crystals are mounted on flexure stages driven by piezo-transducers. This allows the fine tuning and fast switching of the phase-matching angle in a way that the produced wavelength can be changed to one of the four DIAL wavelengths from laser shot to laser shot.

Two of the described laser systems are used simultaneously in WALES. The two OPOs are seeded by four independent distributed feedback (DFB) laser diodes. They can be tuned to any wavelength in the range from 935.0 nm to 936.0 nm and are locked and stabilized to their appropriate DIAL wavelength using a 36 m multi-pass H_2O absorption cell and wavemeters.

Each OPO generates two DIAL wavelength in an alternating fashion. This is achieved by switching two DFB-lasers with micro-electromechanical switches to one OPO every 10 ms. The time difference between output pulses of the two transmitters is set to 5 ms such that DIAL pulses are emitted at an effective frequency of 200 Hz. The remaining radiation at 1064 nm and 532 nm is also emitted to the atmosphere. The output pulse energy is 120 mJ at 1064 nm, 45 mJ at 935 nm and 75 mJ at 532 nm.

A 480 mm Cassegrain telescope with a field of view of 1.6 mrad mounted in nadir viewing direction collects the atmospheric backscatter. The 1064 nm, 935 nm and 532 nm signals are spectrally separated by dichroic beamsplitters. In the 532 nm channel, a polarizing beamsplitter reflects the cross-polarized light onto a photo multiplier tube (PMT). One half of the transmitted parallel polarized light is detected by another PMT. This signal is the combined backscatter from aerosols and molecules. The other half is sent through an iodine absorption cell. Here the spectrally narrow backscatter peak from aerosols is filtered out, leaving only molecular backscatter. This molecular signal is recorded by a third PMT. In the 1064 nm channel, another polarizing beamsplitter is employed, however no HSRL filtering is available at this wavelength. All DIAL wavelengths around 935 nm are directed onto the same avalanche photo diode sensor.

The recorded profiles of r_{H_2O}, $\mathbb{R}$ and δ^{part} form two dimensional curtains along the flight track of the research aircraft intersecting the atmosphere below. The lidar data used in this work have a vertical resolution of 15 m. Raw data are sampled at a rate of 5 Hz. At HALO's typical ground speed of 210 m s^{-1} and after averaging for an improved signal-to-noise-ratio, horizontal resolution is 2.5 km for r_{H_2O} and 210 m for $\mathbb{R}$ and δ^{part} in the data used in this work.

An in-depth description of the system can be found in (*Esselborn et al.*, 2008) and (*Wirth et al.*, 2009). For determining δ^{part}, an advanced two-angle $\pm 45°$ calibration scheme

is applied (see section 2.1.3), achieving an absolute accuracy of 5 percentage points at typical cirrus δ^{part} values. For this the whole detection unit can be rotated around the optical axis of the telescope.

In order to exclude liquid and mixed phase clouds and aerosol layers from the data, only measurements at temperatures below 235 K and above a $\mathbb{R}$ threshold of three are considered. The $\mathbb{R}$ threshold was determined after carefully inspecting all flight legs for aerosol layers. The further analysis was found to be only weakly depending on the exact choice of $\mathbb{R}$ threshold within the range from two to 25.

2.2.3 In-situ instrumentation

During ML-CIRRUS several cloud probes mounted under the wings of HALO, directly sampled ice crystals providing measurements of key microphysical parameters. This work uses measurements of particle number concentration n^{part} and effective diameter d_{eff} from the Cloud Aerosol Spectrometer (CAS, size range: 3 to 50 µm) and Cloud Imaging Probe (CIP, size range: 25 to 475 µm).

CIP takes shadow images of cloud particles that cross a collimated laser beam focused on a linear array of 64 photo diodes. The particles lead to a shading at the sensor array which can be recorded in a snap-shot. These one-dimensional snap-shots are called slices. Multiple slices are taken while the particle advances through the beam and a two-dimensional image is constructed. In order to achieve distortion-free images, the slice recording frequency f is coupled to the true air speed v measured by a pitot tube near the sampling volume of the probe:

$$f = \frac{v}{25\,\mu\text{m}}. \tag{2.32}$$

This way, the measured particle advances by 25 µm in between two recordings. This is also the size resolution in the direction of the sensor array. From the two-dimensional recordings, particle sizes and number concentrations are determined.

CAS, which measures smaller particles, relies on scattering of light rather than on imaging (*Baumgardner et al.*, 2001). It collects the forward scattered light in the range from 4 to 12° of single particles that get illuminated by a focused laser beam when passing through the measurement volume. CAS also measures back scattered light (5 to 14°). With the use of Mie scattering theory, the particle size is determined assuming rotationally symmetrical ellipsoids of random orientation with aspect ratios of 0.75. From the recording of multiple single particles, the number concentration is derived.

Number concentrations from both probes are corrected for the effect of air compression that occurs upstream of the instrument body. This effect depends on the flight velocity and is particularly strong for a fast flying aircraft like HALO. With a method developed by *Weigel et al.* (2015), a correction factor is calculated as a function of true air speed measured at the cloud probe.

In order to compare distributions of d_{eff} and n^{part} with lidar results for specific clouds, suitable in-situ and lidar legs were selected manually ensuring that the data stem from the

same cirrus. In total, eight cases were identified with available in-situ and lidar data (see Table 2.1).

2.2.4 Trajectory calculations

The origin of the air masses that produced the studied clouds, is assessed by examining 24-hour backward trajectories. They are calculated on horizontal wind data from European Centre for Medium-Range Weather Forecasts (ECMWF) Era-Interim reanalysis with a horizontal resolution of 1° by 1°. For vertical transport, diabatic heating rates are used with the trajectory module of the Chemical Lagrangian Model of the Stratosphere (CLaMS) (*McKenna*, 2002). The starting points of these trajectories were chosen such that they are narrowly distributed over the whole lidar cross-section with a temporal resolution of 12 s (about 2.5 km) and a vertical resolution of 150 m. The cloud ice water content (IWC) is interpolated from the reanalysis onto the trajectory path.

2.2.5 Contrail Cirrus Prediction Tool (CoCiP)

The Contrail Cirrus Prediction Tool (CoCiP) was used during the campaign to predict contrail occurrence and proofed to be a valuable tool for flight planning. After the campaign, it was employed to model contrails in the measurement area based on the actual air traffic at the time. For this, traffic data was gathered from multiple organizations and companies (Deutsche Flugsicherung, Eurocontrol, Federal Aviation Administration/Volpe and Flightradar24). Exhaust plumes were simulated for each aircraft with a Gaussian concentration distribution. The plume model accounts for turbulent diffusion and shear. Meteorological data from the ECMWF model was used to determine contrail formation and to transport the contrail and exhaust plume. By combining all plumes/contrails that reached the lidar measurement cross-section, the contribution from contrails to the lidar signal was modeled. I use this information in section 3.2.4 investigating the role of contrails in my analysis. Details of the model are described in *Schumann* (2012).

2.3 Classification scheme of cloud evolution stages

In this section, a newly developed classification scheme is presented. Based on $\mathbb{R}$ and r_{H_2O} measured by WALES and model temperature data, it identifies nucleation regions, ice crystal growth regions and sublimation regions within lidar cloud cross-sections. For that, parameterized freezing onset thresholds for homogeneous and heterogeneous freezing are employed.

A prerequisite for the classification of evolution stages in clouds is relative humidity with respect to ice (RH_i). It is calculated from measured r_{H_2O} and model temperature (6-hourly analysis data from ECMWF, interpolated in time and space onto the lidar cross-section), using the parameterization for water vapor saturation $e_{sat,i}$ by *Murphy and Koop*

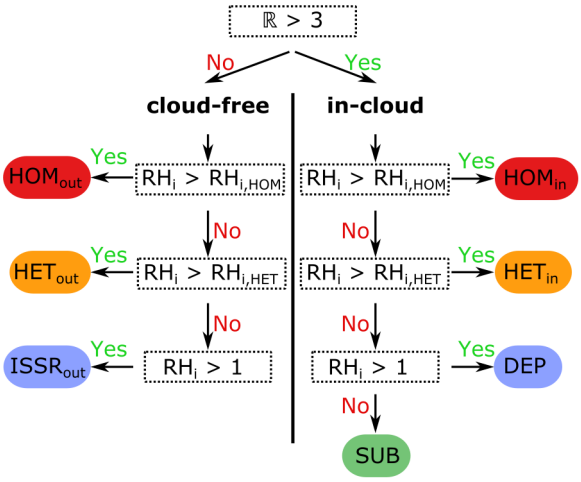

Figure 2.6: Cirrus evolution classification scheme based on WALES backscatter ratio ($\mathbb{R}$) and relative humidity (RH_i) derived from WALES humidity and ECMWF temperature field

(2005):

$$RH_i = \frac{r_{H_2O} n_{air} T k_B}{e_{sat,i}(T)}. \tag{2.33}$$

Here, T is temperature, n_{air} is the volume number density of air, and k_B is the Boltzmann constant.

The accuracy of calculated relative humidity relies strongly on the quality of absolute humidity and temperature data. WALES humidity measurements exhibit a mean statistical uncertainty of 5 %. The applicability of ECMWF temperature on this calculation was investigated by *Groß et al.* (2014). They showed that during ascent and descent of a similar research flight in 2010, the mean temperature difference between ECMWF and on board temperature sensors was 0.8 K and estimated a resulting maximum relative uncertainty of 10 to 15 % as an upper boundary for the calculated RH_i at typical cirrus temperatures.

In cases where collocated radiosonde or dropsonde measurements are available, their temperature profiles can be used to calibrate ECMWF temperature fields, eliminating possible offsets. As modern sondes feature measurement uncertainties of down to 0.2 K, the total relative uncertainty of RH_i can therefore be reduced to values as low as 6 %. Although successfully demonstrated by *Groß et al.* (2014) in a research flight over Germany, calculating RH_i inside of cirrus from model temperature could potentially lead to inaccuracies, as temperature fluctuations might not be properly resolved in other cases.

With atmospheric lidar cross-sections of RH_i and $\mathbb{R}$ at hand, in-cloud and cloud-free regions can readily be identified by applying a threshold for the backscatter ratio (see Figure 2.6). As mentioned above, in this work a value of $\mathbb{R}$=3 is used, however in cases where, for example, thick aerosol layers are present, this threshold might need to be increased to avoid misclassifications.

Looking at cloud-free parts of the cross-section, regions that might possibly lead to

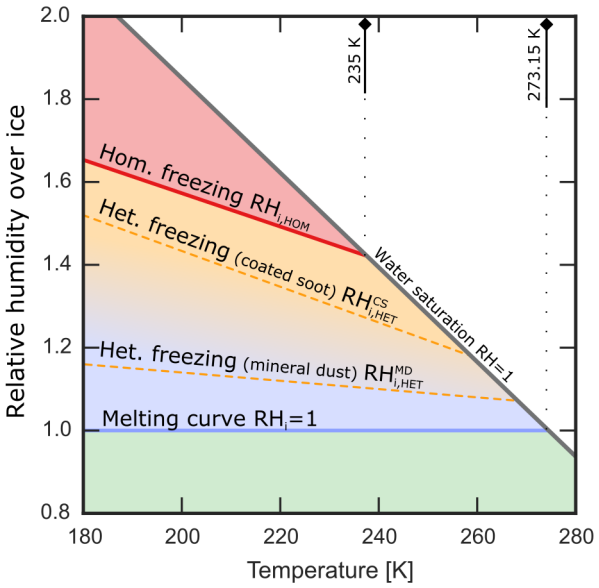

Figure 2.7: Homogeneous and heterogeneous freezing onset thresholds plotted against temperature

cirrus cloud formation can be identified by searching for data points exhibiting ice supersaturation ($RH_i > 100\,\%$). Moderately supersaturated cloud-free parts are classified as $ISSR_{out}$. With higher supersaturations, the chance for the imminent nucleation of ice particles becomes increasingly higher. Therefore I introduce the class HET_{out} and HOM_{out} in the classification. They represent regions outside of the cloud where onset conditions for heterogeneous and homogeneous freezing, respectively, are surpassed. Their classification is implemented via temperature-dependent humidity thresholds.

Koop et al. (2000) found that the homogeneous freezing temperatures of numerous aqueous solution droplets (1 to 10 µm in size) would fall on a single solute-independent curve, when plotted in terms of water activity a_w. They suggested that this curve could be constructed by shifting the melting point curve by Δa_w. From experiments on homogeneous freezing, they determined a shift by Δa_w=0.305. For atmospheric applications, water activity is equal to relative humidity, when the droplet is in equilibrium with the water vapor pressure of the surrounding air (*Kärcher and Lohmann*, 2002). These findings are used to extract a parameterization of the temperature-dependent onset humidity for HOM[1] (see Figure 2.7).

To determine a humidity threshold for HET, detailed information of the involved aerosol type, its coating, and size distribution would be required. Then results from laboratory experiments on onset freezing temperatures and saturation for this kind of aerosol could be used. As heterogeneous freezing conditions are still subject to current research (*Hoose and Möhler*, 2012) and as comprehensive aerosol information is difficult to acquire solely from

[1] $RH_{i,HOM}(T) = 232 - 0.37\,\mathrm{K}^{-1} \cdot T$ (*Koop et al.*, 2000)

remote sensing, I make only a coarse distinction between two aerosol types - mineral dust (MD) and coated soot(CS) - and employ simplified onset parameterizations $RH_{i,het}^{MD}(T)$[2] and $RH_{i,het}^{CS}(T)$[3]. They represent ice nuclei that lead to earlier and later heterogeneous freezing.

Until more detailed parameterizations are available, this imposes an uncertainty for the determination of the exact border of heterogeneous freezing regions. The classes $\mathrm{ISSR_{out}}$ and $\mathrm{HET_{out}}$ represent pre-stages of cirrus formation and indicate regions where a cirrus cloud is likely to develop.

Inside a cloud ($\mathbb{R} > 3$), I proceed in the same manner. When the $RH_{i,hom}(T)$ threshold is surpassed I classify the region as $\mathrm{HOM_{in}}$. The region shows active ice nucleation. Together wit $\mathrm{HET_{in}}$ which is classified analogously, it represents the youngest evolution stage of a cirrus cloud. $\mathrm{HET_{in}}$ is also expected to show active nucleation as long as ice nuclei are present in the freezing region. However, due to the limitations mentioned above, the border of HET towards lesser supersaturated areas must be interpreted with caution. Also, ice crystals found in HET must not necessarily be formed by heterogeneous freezing, as sedimentation from higher levels featuring different nucleation conditions may take place. Nevertheless, heterogeneous freezing is an important freezing mechanism in midlatitudes (*Cziczo et al.*, 2013) and the class $\mathrm{HET_{in}}$ adds more information to the classification, leading to a more complete characterization of cirrus clouds.

When relative humidity inside the cloud is lower than the freezing threshold, I classify as DEP, as the remaining supersaturation is depleted by deposition of water vapor onto the existing ice particles. This intermediate evolution stage is dominated by depositional growth of ice crystals. The final evolution stage of a cloud sets in, when relative humidity falls below 100 %. In such an environment ice inevitably must sublimate. I classify this region as SUB.

It should be noted that ice forms at the latest point, as soon as conditions for homogeneous freezing are reached, as there is always a sufficient amount of solution droplets in the atmosphere (*Minikin et al.*, 2003). Therefore, a cloud classification should not feature considerable regions of HOM_{out}. This fact should be kept in mind when choosing a $\mathbb{R}$ threshold value for the cloud border detection, making sure that HOM regions lie inside the cloud. However this might not always be completely achievable without misclassifying aerosol layers (see above). In contrast to $\mathrm{HOM_{out}}$, $\mathrm{HET_{out}}$ regions may exist in cases with no sufficient amount of aerosol ice nuclei or due to simplification in the utilized $RH_{i,het}(T)$ threshold.

During the life cycle of a cloud, nucleation, growth, and sublimation events may occur more than once, e.g., when atmospheric dynamics cause renewed updrafts and a second freezing event on top of pre-existing ice takes place. As described, the classification scheme is able to identify nucleation, growth, sublimation regions, and pre-stages of cloud formation. However on its own, it does not yield any information about earlier developments of those regions. Its very strength is to revel the actual atmospheric state with regards

[2] $RH_{i,het}^{MD}(T) = 134 - 0.1\,\mathrm{K^{-1}} \cdot T$ (*Krämer et al.*, 2016)
[3] $RH_{i,het}^{CS}(T) = 230 - 0.43\,\mathrm{K^{-1}} \cdot T$ (*Krämer et al.*, 2016)

to cirrus evolution at the time of measurement. This is done on a high spatial resolution that exceeds typical resolutions of global circulation models, enabling the detailed study of individual cloud parts.

Chapter 3

Results

In the first part of this chapter, midlatitude cirrus clouds are characterized concerning their particle depolarization ratio and relative humidity, both measured by WALES. As cirrus clouds are still difficult to access with atmospheric measurements, such a characterization may help to intensify our knowledge on cirrus properties in different regions of the globe. In a detailed case study (section 3.1.1) data measured by lidar and the application of the classification scheme are introduced. Then in sections 3.1.2 and 3.1.3, statistical examinations of relative humidity and particle linear depolarization are presented.

In the second part, distinct features in the δ^{part} distribution of clouds are associated with an indirect aerosol effect from aircraft exhaust particles on natural cirrus cluods. For that, the origin of the clouds in air traffic regions is examined (section 3.2.1) and traces from heterogeneous freezing are identified in lidar measurements of relative humidity and in in-situ measurements of crystal size and number concentration (sections 3.2.2 and 3.2.3). In section 3.2.4 I show that other potential influences cannot explain the results from section 3.1.

3.1 Characterization of midlatitude cirrus clouds with airborne lidar data

3.1.1 Case Study (Application in a lee wave cirrus case)

The applicability of the classification scheme is demonstrated in a cirrus case that was obtained during the research flight on 29 March 2014. The meteorological situation over western Europe and the Iberian Peninsula on the flight day is dominated by a trough extending from the west of Ireland to the Iberian Peninsula and further to the western part of northern Africa (Figure 3.1(a)). At 300 hPa, high southerly winds with wind speeds up to $35\,\mathrm{m\,s^{-1}}$ are observed on the leading edge over southern France and Spain. Two days before the research flight, model forecasts indicated the existence of cirrus forming from high updrafts over the Pyrenees, as well as cirrus influenced by lee waves north of the mountain ridge. Additionally, high dust-loaded air masses over southern France originating

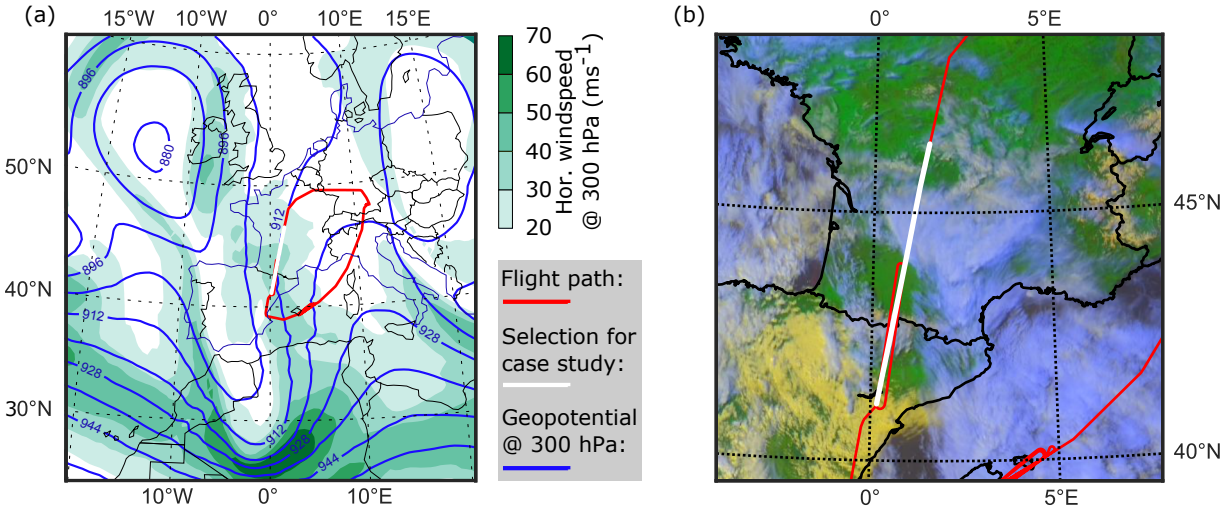

Figure 3.1: Meteorological situation on 29 March 2014 over western Europe: (a) ECMWF analysis data (12:00 UTC) at 300 hPa of geopotential (blue isolines) and horizontal wind speed (shaded green). (b) SEVIRI false-color image taken at 14:30 UTC (see text). High ice clouds have a blue color, lower liquid clouds are yellow, cloud-free ground has green color. The path of the research flight is plotted in red and the flight leg used in the case study (14:16–14:58 UTC) is marked white.

from Saharan dust events over Algeria were expected.

In this meteorological setting the research flight was performed with the aim of sampling all stages of cirrus evolution that resulted from an overflow of the Pyrenees with high wind speeds and consequent gravity wave excitation in the lee of the mountain ridge. For this, the flight path in the relevant measurement region was chosen to run along the main wind direction, sampling the clouds along their path of advection.

The flight (Figure 3.1 red flight path) started at Oberpfaffenhofen, Germany at 12:37 UTC and first went westward towards Paris, followed by a southward flight leg towards Spain at an altitude of 11 200 m. The investigated cirrus cloud was encountered over southern France during this leg, which runs with a bearing of 190° (white flight leg). Inside cirrus clouds, over the Pyrenees mountains, three legs at different lower altitudes followed. From the Mediterranean coast the aircraft turned eastward and probed cirrus at several altitudes near the Balearic Islands before it went northward towards Oberpfaffenhofen (landing at 19:50 UTC).

The following discussion of the classification scheme focuses on the southward flight leg stretching about 400 km to the north and 200 km to the south of the Pyrenees (Figure 3.1 white flight leg). Figure 3.1(b) shows a false-color image of the Pyrenees area derived from SEVIRI (Spinning Enhanced Visible Infrared Imager) data at 14:30 UTC. The red,

green, and blue color channels of the image take SEVIRI's 635 nm, 850 nm, and inverted 10.8 µm channel data. This way, the high and therefore cool cirrus clouds stand out with a bluish color. Low clouds are depicted in yellow and the surface of the Earth has a green tone. Coming from the north, the flight path intersects an ice cloud that is part of a larger cloud regime expanding from southern France towards the Algerian coast. This cloud is followed by a completely cloud-free area north of the Pyrenees. Over the mountain ridge some localized high clouds are crossed.

Earlier satellite pictures and ECMWF data (not shown) indicate that the cirrus cloud regime formed under the influence of a highly humid air mass stemming from southern Spain that also shows the tendency to produce lower liquid clouds. As the air mass is transported to the north, it is impacted by gravity waves generated when crossing the Pyrenees. The analysis of preliminary temperature data (not shown) provided by the on-board, passive Microwave Temperature Profiler (*Denning et al.*, 1989) shows that temperature oscillations, caused by gravity waves, continue to exist inside the cirrus cloud intersected by the flight path.

In Figure 3.2, a cross-section showing backscatter ratio at a wavelength of 532 nm along the chosen part of the flight path is plotted. Here atmospheric features apparent in Figure 3.1 can be studied in greater detail. On the lee side, north of the Pyrenees (14:19 to 14:34 UTC), a high cirrus cloud is observed that extends from a height of 7000 m to 10 400 m. The southern and middle parts are dominated by high $\mathbb{R}$ values from 50 up to 200, whereas the northern section exhibits lower values. Depolarization ratios of more than 0.3 inside the cloud and temperatures below 240 K clearly indicate a pure ice cloud (see description below and Figure 3.4).

Over the Pyrenees (14:42 to 14:53 UTC) a lower cloud is located at an altitude of about 6000 m. Its spatially restricted occurrence over the mountain ridge indicates a formation due to forced updrafts stemming from the southerly cross-mountain flow. Even lower, at a height of 4000 m a thick aerosol layer is discernible. An analysis of δ^{part} shows values between 0.2 and 0.3, typical for Saharan mineral dust (*Groß et al.*, 2013) which is consistent with the origin of the air masses in northern Africa, as forecasted by dust models.

Furthermore, in the region between the two clouds (14:34 to 14:43 UTC) gravity lee waves are discernible at an altitude of about 9500 m and also in the lower aerosol layer. These waves are expected to influence at least parts of the northern cirrus cloud.

Figures 3.3, 3.4 and 3.5 give a close-up view of the selected data marked with a black rectangle in Figure 3.2. Water vapor volume mixing ratio r_{H_2O} measured by WALES is plotted in Figure 3.3(a), together with red isolines of ECMWF temperature. A black contour line ($\mathbb{R}$=3) marks the cloud border. With increasing altitude, r_{H_2O} is generally decreasing. This is because almost all sources of water vapor, such as oceans, lakes, and streams, are located at the Earth's surface, and because the chance for condensation and precipitation rises with decreasing temperatures, depleting the absolute humidity at higher levels of the troposphere. In contrast to that general behavior, a humid layer, surrounded by dryer air at a height of approximately 9000 m, can be found upstream of the cirrus cloud (14:34 to 14:40 UTC). In this region, the water vapor data exhibit the same oscillations as previously seen in the $\mathbb{R}$ data.

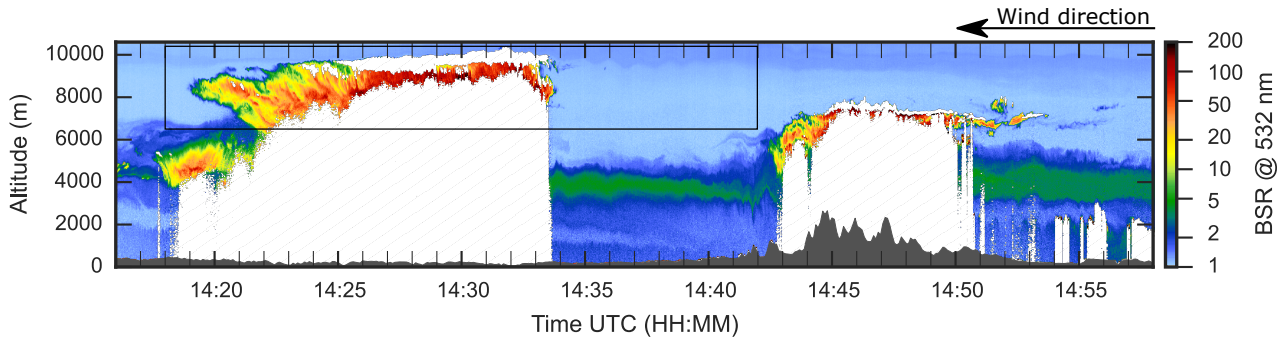

Figure 3.2: Backscatter ratio ($\mathbb{R}$) at 532 nm measured along the flight path (white line in Figure 3.1). Hatched areas indicate data that were excluded due to detector saturation or low signal-to-noise ratio and the terrain profile is shown in dark gray. The black rectangle marks the cirrus region that is studied further (see Figures 3.3, 3.4 and 3.5). The arrow shows the main wind direction at cirrus level.

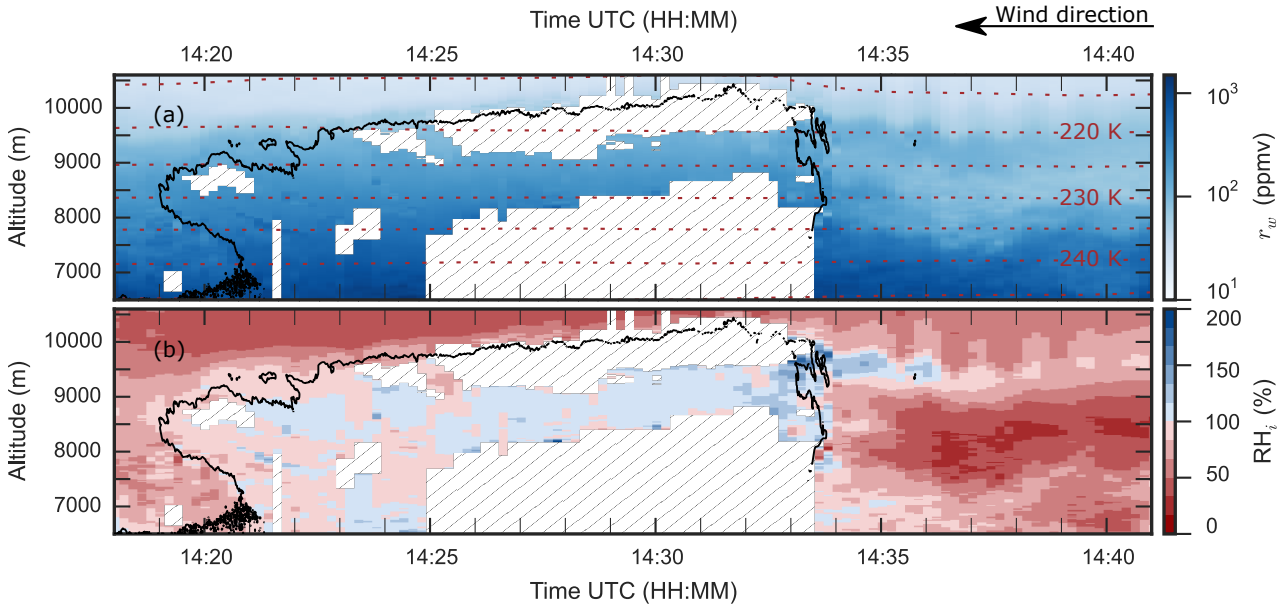

Figure 3.3: Humidity data of cirrus marked in Figure 3.2: (a) water vapor mixing ratio rw as measured with WALES and ECMWF temperature contour lines. (b) Relative humidity with respect to ice (RH_i) derived from WALES data and ECMWF temperature field. The cirrus is outlined by a black contour line ($\mathbb{R} = 3$) and invalid data are marked by black hatching.

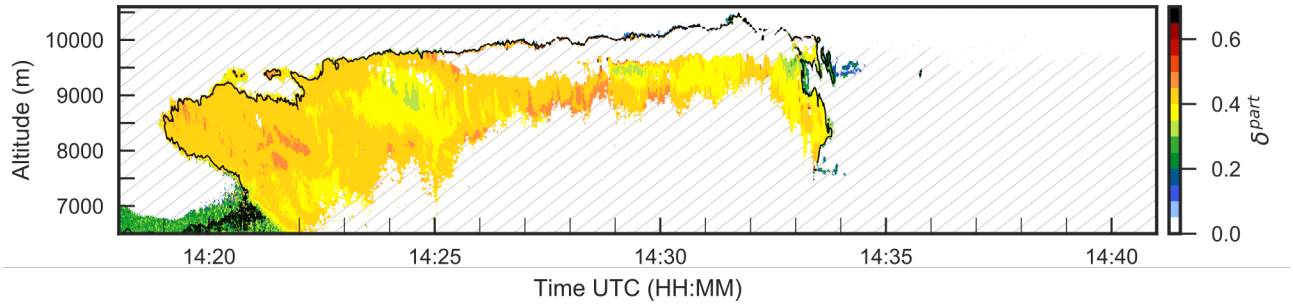

Figure 3.4: cross-section of particle linear depolarization ratio δ^{part}. The cirrus is outlined by a black contour line ($\mathbb{R} = 3$) and invalid data are marked by black hatching.

Relative humidity with respect to ice is plotted in Figure 3.3(b). As expected, supersaturated regions (blue) are found mostly inside of the cirrus. There are also major subsaturated regions (red) in the northern part of the cloud. South of the cirrus, high supersaturations exist in cloud-free air, mostly in the crests of the gravity waves (14:34 to 14:36 UTC), and directly at the cloud edge. They indicate a nucleation region.

The particle linear depolarization ratio δ^{part} (Figure 3.4) at the southern cloud edge and cloud top (from 14:29 to 14:35 UTC) shows remarkably low values between 0.05 and 0.25 that provide a stark contrast to the much higher values at the core of the cloud. This specific pattern exists in other ML-CIRRUS cases too. I will investigate and interpret it in section 3.1.3. Inside the cloud, δ^{part} values range from 0.35 to 0.5. Patches with ∼0.35 are located at 14:24:30 UTC, 14:29:30 UTC and 14:33:00 UTC. Regions with ∼0.5 are found betwen 14:20 and 14:23 UTC and between 14:26 and 14:30 UTC. The mineral dust layer below the cloud (14:18 to 14:21 UTC) is clearly distinguishable due to its low and homogeneous δ^{part} of about 0.3.

The classification is applied and the results are visualized in Figure 3.5. Data pixels are classified and marked in color accordingly, and in-cloud and cloud-free regions can be distinguished by the black contour line for a $\mathbb{R}$ value of 3. Heterogeneous freezing is identified using the HET threshold for coated soot ($RH^{CS}_{i,het}(T)$). This decision is based on 48 h backward trajectory calculations of air masses at 8 to 9.5 km (not shown) that indicate no influence from lower Saharan dust-loaded levels. Subsaturated regions outside of the cloud are left blank and areas where no valid data are available are indicated by black hatching.

The above mentioned humid layer, discernible in Figure 3.3, reaches ice supersaturation (ISSR) in the two crests of the gravity lee wave to the south of the cloud (14:34 to 14:36 UTC). At the cloud edge, the HET and HOM freezing thresholds are also surpassed (14:33 to 14:34 UTC). As no relevant isolated HET region exists and HOM freezing also sets in at the cloud edge, there is reason to assume that homogeneous freezing might be the dominant freezing mechanism here. This upper, southern section of the cirrus is dominated

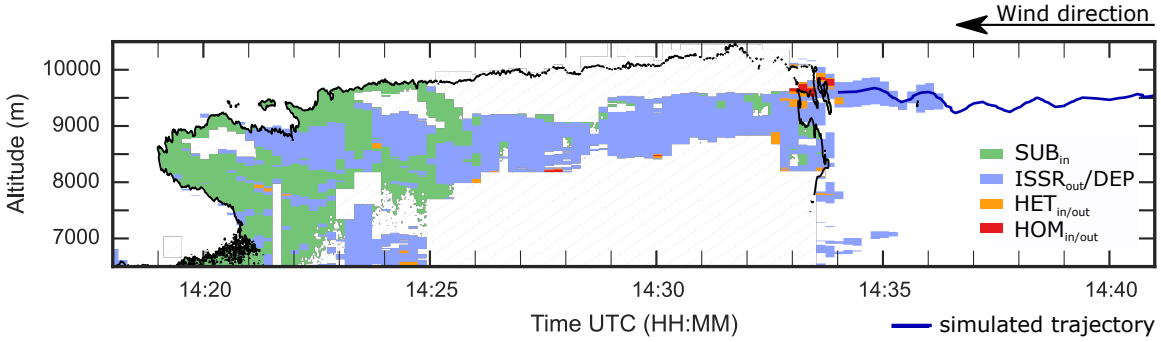

Figure 3.5: Classified evolution regions of cirrus cloud. In-cloud and cloud-free regions can be distinguished by the black contour line of $\mathbb{R} = 3$. Regions of ice nucleation ($\mathrm{HOM_{in/out}}$, $\mathrm{HET_{in/out}}$), ice supersaturation outside ($\mathrm{ISSR_{out}}$), and depositional growth (DEP) and subsaturation (SUB) inside the cloud are visualized. Subsaturated regions outside the cloud are left blank and invalid data are marked by black hatching.

by nucleation and represents the youngest part of the cloud.

The top level of the cloud and the ISSR south of it climbs from about 9300 m to 10 400 m at 14:31:50 UTC. Considering the speed of the aircraft ($200\,\mathrm{m\,s^{-1}}$) and the wind speed (about $30\,\mathrm{m\,s^{-1}}$ in opposite direction), and assuming that the fount pattern is stationary, this corresponds to a vertical velocity of about $0.5\,\mathrm{m\,s^{-1}}$. In the temperature range between 200 K and 220 K, such high vertical velocities typically lead to high ice crystal number densities with small ice particles (*Kärcher and Lohmann*, 2002, $r < 10\mu m$). As the updraft region is observed between 14:32 and 14:36 UTC, it can be assumed that freezing takes place at least between the cloud edge and the peak of the cloud top at 14:31:50 UTC, although no valid data are available for parts of the upper cloud due to detector saturation.

In the middle (14:26 to 14:32 UTC), a section of moderate supersaturation (DEP) is located. This is an already well developed part of the cirrus that is dominated by depositional growth of ice crystals. After the initial ascent (14:32 to 14:34 UTC), the cloud top slopes from over 10 000 m down to under 9000 m at the northern edge, corresponding to a vertical velocity of about $-0.3\,\mathrm{m\,s^{-1}}$. Sedimentation may contribute to this, but sub-10-μm particles are rather associated with fall speeds of under $0.02\,\mathrm{m\,s^{-1}}$ (*Gasparini et al.*, 2017, their Figure 1). This large-scale descent, also apparent in ECMWF model data (not shown), reduce supersaturation and evokes the intermediate DEP region as well as large connected regions of subsaturation (SUB) in the northern part of the cloud (14:19 to 14:26 UTC). Here the cloud is starting to break up, as ice particles are sublimating.

From these results all cirrus evolution stages can be identified: from cloud-free ISSR and ice nucleation (HET, HOM) aided by vertical displacements in a gravity lee wave, to crystal growth by deposition of water vapor in a moderately supersaturated region DEP, to the dissolving of the cloud in a subsaturated region (SUB), caused by a large-scale descent.

The spatial distribution of these major stages of cirrus evolution feature a horizontal

component with ice nucleation in the south and dissipation in the north. Also, SUB regions are found at the cloud top level, in part, located above DEP regions in the north of the cloud. These finding fit well into the perspective of model simulations, investigating the influence of dynamics on the evolution of a cirrus cloud (*Spichtinger and Gierens*, 2009) that also found more complex horizontal distributions deviating from a simplistic cirrus evolution pattern comprising ice nucleation at the cloud top level, crystal growth in the middle and sublimation at the bottom. Thus, the classification illustrates how the large-scale meteorological context, wind, and gravity wave fields can affect the structure of individual clouds.

Unfortunately no dropsonde temperature measurements could be conducted in this cirrus case. Thus the maximum relative uncertainty of RH_i is estimated between 10 and 15% at cirrus level. This directly translates into an uncertainty in locating the exact border between evolution stages. However, the horizontal distribution order and the existence of SUB regions at the cloud top continue to exist even after offsetting the temperature by $\pm 0.8\,K$. Thus, ECMWF temperature data is suitable for this kind of analysis.

Overall, the classification proved to be applicable in a meteorological context that comprises both mesoscale and large-scale dynamics. It identifies all relevant stages of cirrus evolution and their detailed spatial distribution and thus also reveals the influence of gravity waves and large-scale atmospheric motion on the studied cirrus cloud. Further investigations of the influence of gravity waves in this case study can be found in the publication by *Urbanek et al.* (2017).

3.1.2 Relative humidity and the thermodynamic state

The overall distribution of relative humidity over ice inside cirrus clouds ($\mathbb{R} > 3$ and $T < 235\,K$) during ML-CIRRUS is plotted in Figure 3.6. It shows a mean value of 96 % with an inter-quartile range (IQR) of 16.4 %. Measured values range from below 54.6 % to more than 141.3 % (0.5^{th} and 99.5^{th} percentile).

The supersaturated part of the distribution features a tail towards higher values. In this cloud parts, the supersaturation has not yet relaxed to the equilibrium at 100 %. They can be interpreted as formation regions. The highest achievable supersaturation in cirrus is limited by the homogeneous freezing threshold (143 % and above, depending on the temperature, see section 2.6), or in case of heterogeneous freezing by the threshold of the relevant ice nuclei that lies below that. However, in mature or dissipating clouds with no active nucleation, the maximum observed humidity may be much lower.

Distributions of all clouds are plotted in Figure 3.7 ($\mathbb{R} > 3$ and $T < 235\,K$). They form more or less bell-shaped, slightly skewed curves with one clear mode around the saturation point. Their median lies between 84 % (M4) and 101 % (M11) with IQR between 11 % (M12) and 20 % (M10). The highest supersaturations (99.5^{th} percentile) reach values between 122 % (M9) and 156 % (M11). In the region below 50 % almost no data is found. Median, IQR, and 99.5^{th} percentile of all distributions are given in Table 3.1.

In the cases M6 and M11, very high supersaturations (150%) indicate active homogeneous ice nucleation. Together with a median above 100% (the majority of the cloud is

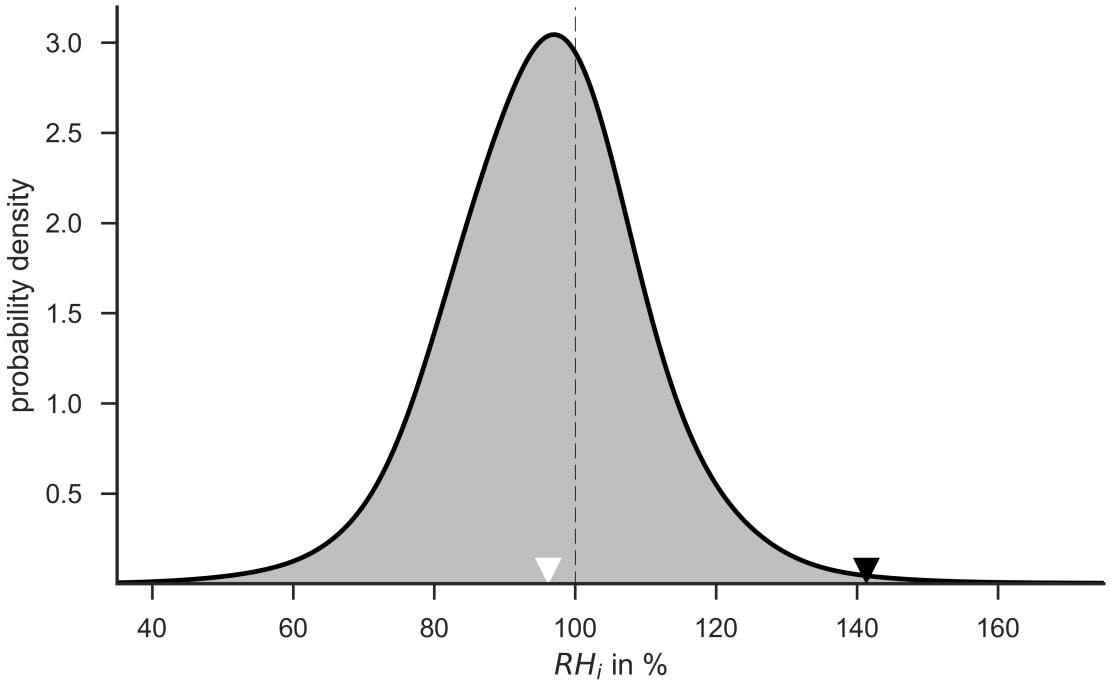

Figure 3.6: Probability density function of Lidar RH_i data taken inside midlatitude cirrus clouds, during ML-CIRRUS ($\mathbb{R} > 3$ and $T < 235\,K$).

Table 3.1: Median, Inter-quartile-range (IQR) and 99.5th percentile in % for RH_i distributions plotted in Figure 3.7

Number	**M4**	**M5**	**M6**	**M7**	**M8**	**M9**	**M10**	**M11**	**M12**	**M14**
Median	84.3	94.9	101	98.4	95.0	94.1	94.7	101.3	97.2	94.8
IQR	13.5	18.9	16.7	12.0	18.4	12.2	20.0	15.2	10.5	13.2
99.5th perc.	126.0	142.8	154.9	127.6	144.3	122.0	142.5	156.1	130.2	137.7

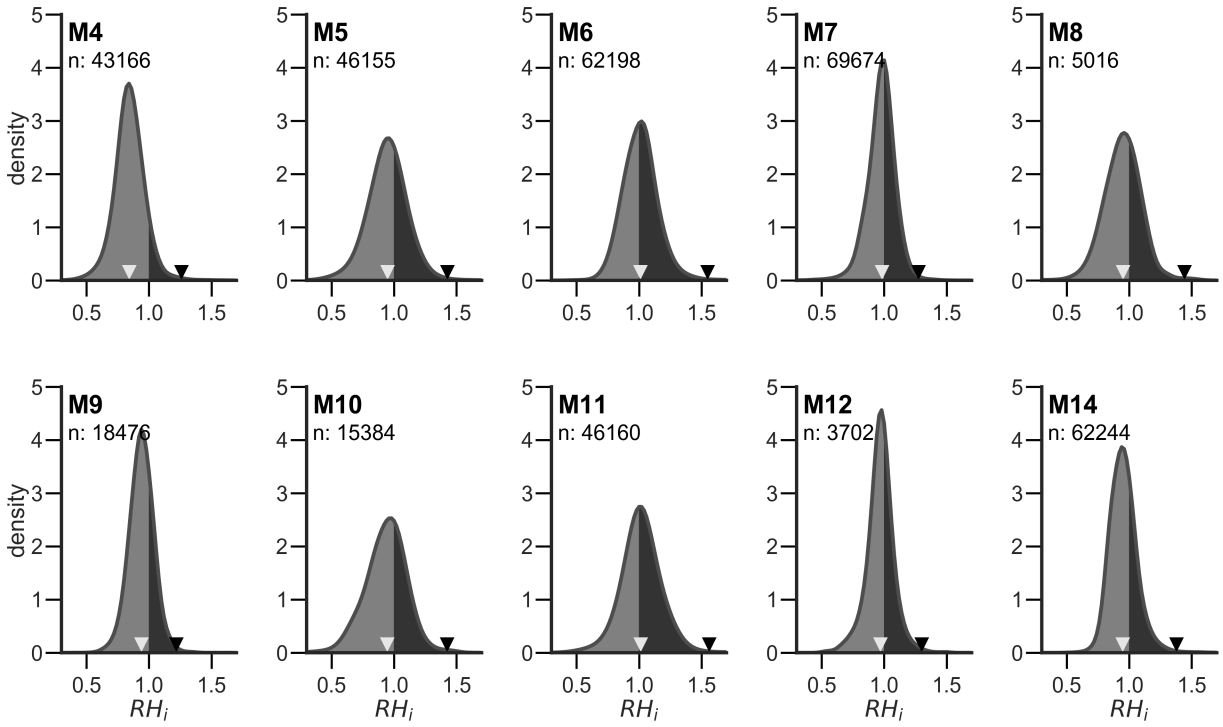

Figure 3.7: Probability density functions of Lidar RH_i data taken inside midlatitude cirrus clouds, during ML-CIRRUS ($\mathbb{R} > 3$ and $T < 235\,K$). Supersaturated parts are highlighted in black, white triangles mark the median, black triangles mark the 99.5^{th} percentile and n gives the number of data points.

supersaturated, particles are growing) this represents a cloud in an developing life-cycle state. The case M4 has a very low median. That means a large majority of the cloud undergoes ice sublimation and particle loss. Low supersaturations (126 %) show that hardly any nucleation is taking place. Together this characterizes a cloud at a late life-cycle state that is likely to break up soon.

Other cases are not that clear. One example is M7: On the one hand its comparably high median at 98.4 % indicates a developing cloud, on the other hand its 99.5^{th} percentile is only at 128% which excludes the possibility of homogeneous freezing. This distribution might be explained by the active formation through heterogeneous nucleation. However in the case of doubt, a cloud forming through heterogeneous freezing might not be distinguishable from a cloud shortly after the end of active nucleation with absolute certainty, based on its humidity distribution.

The thermodynamic state of clouds

Applying the newly developed classification scheme (section 2.3) different evolution stages inside cirrus are identified based on measured humidity, model temperature and freezing onset parameterizations. Figure 3.8 shows the rate of occurrence of these stages in the measured cirrus cross-sections of all mission flights. The majority of the cross-section (62 %) is in a subsaturated state and 27 % shows a moderate supersaturation. Heterogeneous freezing conditions are surpassed in 10 % of the in-cloud data and homogeneous freezing conditions are surpassed in 0.5 % (corresponding to a cross-section of 72 km^2). Ice-free supersaturation is registered in an area corresponding to 13 % of the cloud cross-section.

Strong backscatter from cloud top regions with high ice crystal number concentrations occasionally led to detector saturation and invalid data during the flight campaign. It can be expected that nucleation classes are affected by this to a higher proportion. Thus the fractions of HOM and HET in our analysis might be slightly underestimated.

In an earlier study, *Diao et al.* (2013) applied their own classification scheme to in-situ data taken in the upper troposphere ($T < 233\,\text{K}$) during a flight campaign in North America from April to June 2008. Due to the different approaches, only the results for ISSR and SUB can reasonably be compared. The general results are similar, however they found higher fractions of ISSR (25.5 %) and SUB (88 %). As the exact results are influenced by the sampling strategy during the flight, the definition of in- and out-of-cloud regions, and the sampled clouds, it is not possible to further interpret the deviation at this point.

3.1.3 Particle linear depolarization ratio

In this subsection, measurements of particle linear depolarization ratio are presented and interpreted. This is a particularly useful variable in investigating cirrus clouds, as it is closely linked to microphysical parameters of ice crystals. Earlier studies mostly reported depolarizations as a function of geographic location, altitude, or cloud type by averaging over all appropriate clouds. This way, the variability within one cloud and from one cloud

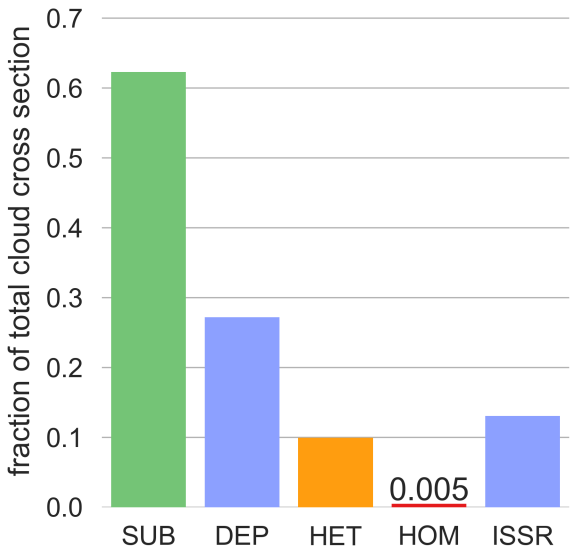

Figure 3.8: Fraction of evolution classes to total cloud cross-section

to another was left out of consideration. By investigating details of δ^{part} distributions, this thesis overcomes such limitations.

The overall δ^{part} distribution of all cirrus cases is plotted in Figure 3.9. It shows a clear bimodal structure with modes around 0.4 and 0.5. This prominent feature will be investigated and discussed in detail over the course of this section and section 3.2. The distributions mean value is 0.43 with an IQR of 0.11. The Majority of data (90 %) has a depolarization ratio between 0.29 and 0.56 which agrees well with the range of previously determined cirrus depolarization ratios both from space borne and ground based instruments (*Noel et al.*, 2002; *Sassen and Zhu*, 2009; *Iwabuchi et al.*, 2012). The flanks steeply decline towards 0.25 and 0.6, respectively, and then turn into long tails. Thus, cloud regions with extreme values, below 0.16 and above 0.62 (0.5^{th} and 99.5^{th} percentile) exist.

Extreme depolarization ratios

When examining individual cloud cross-sections, regions with such extreme values can regularly be found at the cloud top (see for example Figure 3.4). To quantify this result, the altitude of δ^{part} measurements is plotted relative to the cloud top height in Figure 3.10. The cloud top was determined as the 98^{th} altitude percentile for each cloud. Three distributions for cloud regions with $\delta^{part} < 0.16$, $\delta^{part} > 0.62$ and $0.16 < \delta^{part} < 0.62$ were determined. Regions with moderate δ^{part} values concentrate in a height 0.6 km to 1.8 km below cloud top (25^{th} and 75^{th} percentile). In contrast to that, regions with extreme values feature pronounced peaks at the cloud top (−0.05 km and −0.22 km) and smaller peaks around 3 km below cloud top.

A possible explanation for such extreme depolarizations comes from T-matrix calcu-

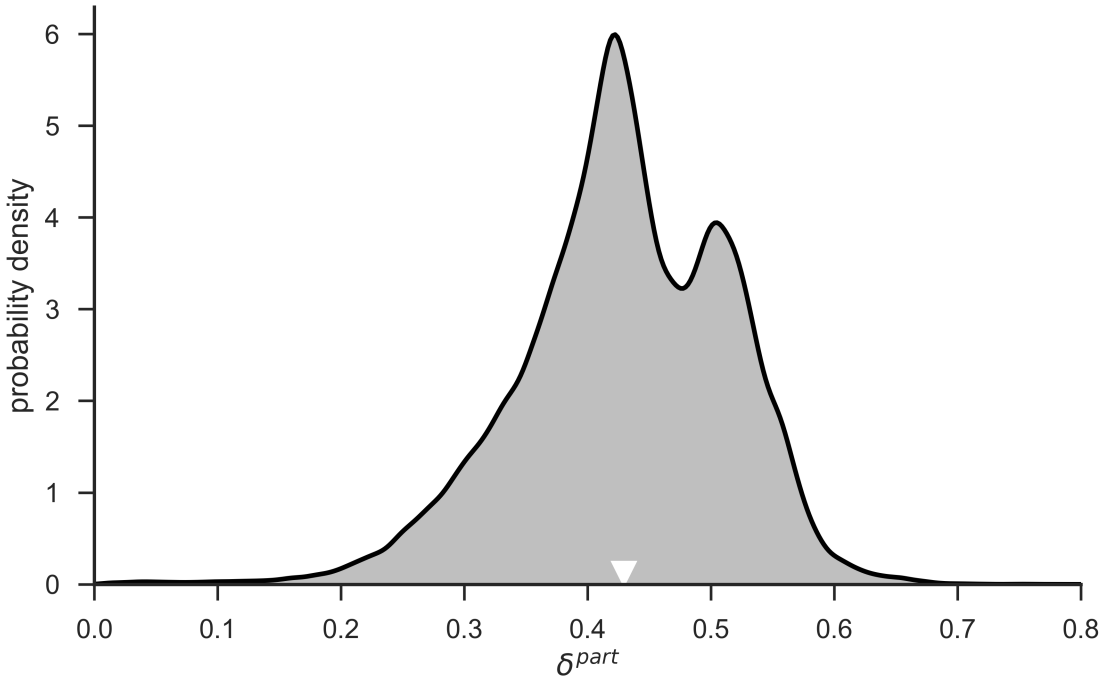

Figure 3.9: Probability density function of particle linear depolarization ratio data from all cirrus clouds during ML-CIRRUS ($\mathbb{R} > 3$ and $T < 235\,K$). The distribution shows a clear double mode structure with peaks at 0.4 and 0.5. Additionally extremely low values below 0.16 and high values above 0.62 have been recorded.

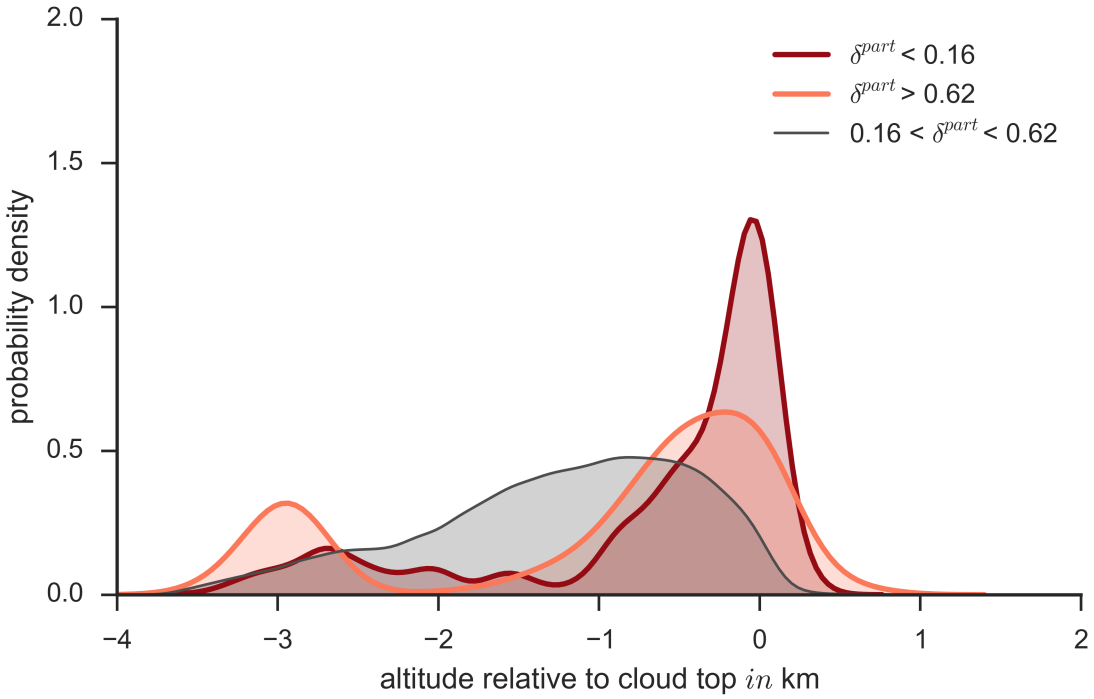

Figure 3.10: Altitude distributions relative to cloud top level for cirrus regions with specific depolarization values. The cloud top is defined as the 98$^{\text{th}}$ altitude percentile for each cloud case.

lations. *Mishchenko and Sassen* (1998) determined that ice crystals with effective radii smaller than 0.5 µm would exhibit δ-values between 0 and 0.2 in 532 nm lidar systems. As the crystals grow, δ rises rapidly, peaking at an effective radius of about 1 µm. After this, δ decreases again and settles at a more moderate level. This general behavior is mostly independent of particle shape, with the exception of quasi spherical particles that show δ values below 0.2 over a larger size range ($d_{eff} < 2\,\mu m$).

The maximum δ value that is reachable with varying size, strongly depends on the particle shape. In the study, only specific prolate spheroids (aspect ratio = 1.2) and chebychev particles ($0.08 \leqslant$ deforming parameter ≤ 0.12) reach $\delta \geqslant 0.62$. There is reason to believe that the found extreme depolarizatons at the cloud top and base stem from such small particles in the sub-2 µm range that freshly nucleated or are about to dissolve completely. So far, this effect has been associated mainly with contrail formation (*Freudenthaler et al.*, 1996; *Mishchenko and Sassen*, 1998; *Schnaiter et al.*, 2012). However, the existence of extreme depolarizations at cirrus cloud top level shows that it plays a role in natural cirrus as well.

The influence from cloud evolution

In order to examine the influence of classified evolution stages on optical cloud properties, δ^{part} distributions are plotted for all four evolution classes in Figure 3.11. In the

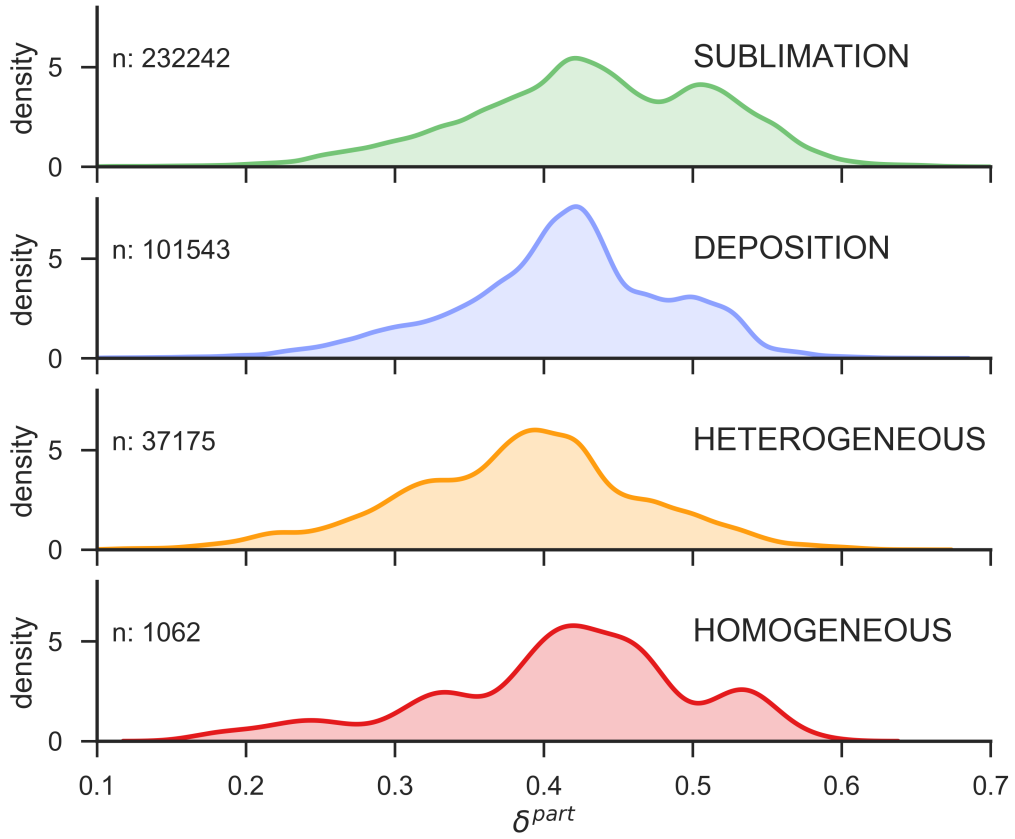

Figure 3.11: Distribution of particle linear depolarization ratio δ^p in four evolution classes, n gives the number of data points in each class.

distributions of sublimation and homogeneous freezing, the double mode is clearly visible. Also in deposition and heterogeneous freezing distributions, a shoulder at the higher mode, above 0.50 is discernible. The median of the distributions lies between 0.39 (heterogeneous freezing) and 0.44 (sublimation). In all, no distinct characteristic in depolarization can be found for individual evolution classes. This gives reason to believe that the evolution class of a cloud part is not the main influencing factor for δ^{part}. Apparently, possible effects from particle growth and aggregation in deposition regions with an increasing complexity in crystal geometry or from dissolving corners and facets during ice dissipation in sublimation regions do not influence the δ^{part} distributions of the cold midlatitude cirrus clouds recorded during ML-CIRRUS.

Two groups of clouds

The individual distributions of all ten mission flights plotted in Figure 3.12, reveal that clouds fall into either one of the two modes discernible in the joint distribution (Figure 3.9). The cases are grouped based on the corresponding mode. The distributions in the upper row (M4, M7, M10, M12, and M14) show significantly higher δ^{part} than distributions in the lower row, with values up to 0.65 and modes and medians above 0.45. Most of the upper row distributions also show very little depolarization below 0.30. In the lower row (M5, M6, M8, M9, and M11), distributions show sharp cut-offs above 0.45 with modes below 0.45 and medians below 0.41. Most of them have considerable cloud fractions with depolarizations below 0.30.

Further on, these groups are referred to as 'δ^{part}-high' and 'δ^{part}-low'. When averaging over the five distributions in each group, they form two separate modes with a mode difference of 0.10 (Figure 3.13). Their medians (means) are located at 0.39 (0.37) and 0.49 (0.47), and they have an IQR of 0.08 and 0.09, respectively.

Such a strong grouping into two modes was not expected and to my knowledge no similar findings have been reported in earlier studies. This discovery was published in *Urbanek et al.* (2018). The affected clouds spread over several thousand square kilometer. Therefore a large scale effect must be responsible for the differences. Further it is known, that deviations in δ^{part} are the result of differences in the microphysical properties of the clouds.

3.2 High depolarization ratios near air traffic regions

3.2.1 Origin of high depolarization clouds in air traffic regions

In order to determine the potential influence from aviation exhaust particles on the two cloud groups, the aerosol load at the location and time of cloud formation has to be considered. Unfortunately, ML-CIRRUS was not designed for the study of an indirect aerosol effect from aviation and the mission flights did not systematically target these regions. Thus crucial information is missing. To overcome this shortcoming, I resort to 24 hour backwards trajectory calculations that help to verify the possibility of aviation as the source of ice nuclei in one of the depolarization groups (see 2.2.4). The trajectories reveal the origin of air masses that produced the investigated cirrus clouds.

The trajectories of all cirrus cases are plotted in Figure 3.14. In order to avoid cluttering of the plot, all trajectories of one cloud are combined into one representative trajectory by taking the median of all locations for each time step. The point of maximum Ice water content along the trajectory is marked by a star. It gives a rough estimate of the location, where the majority of ice has been formed, that was then measured by HALO at a later time.

The air masses stay at pressures between 230 hPa and 380 hPa within the investigated time window of 24 hours. Trajectories from the Atlantic Ocean and the Iberian Peninsula (M4, M7, M8, M9, M11, M12, and M14) are higher in the atmosphere at pressures below

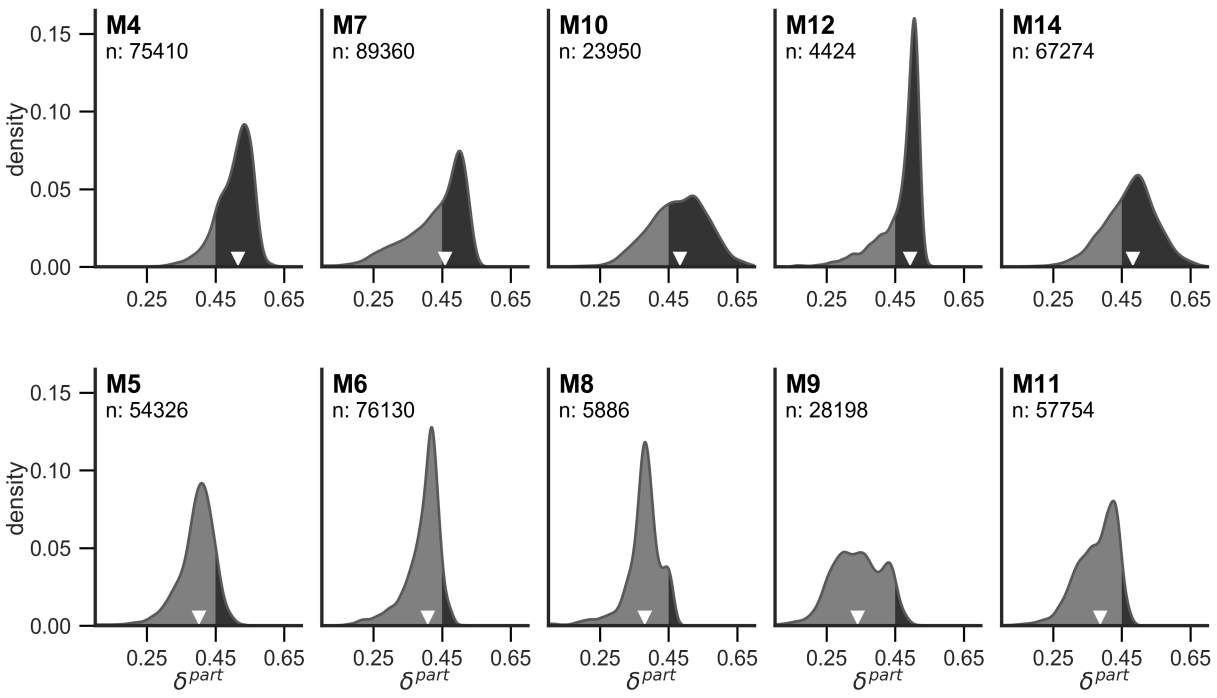

Figure 3.12: Histogram of δ^{part} inside ice clouds ($\mathbb{R} > 3, T < 235K$) for ten mission flights. Values above 0.45 are highlighted in black, medians are marked by a triangle, n gives the number of lidar data points.

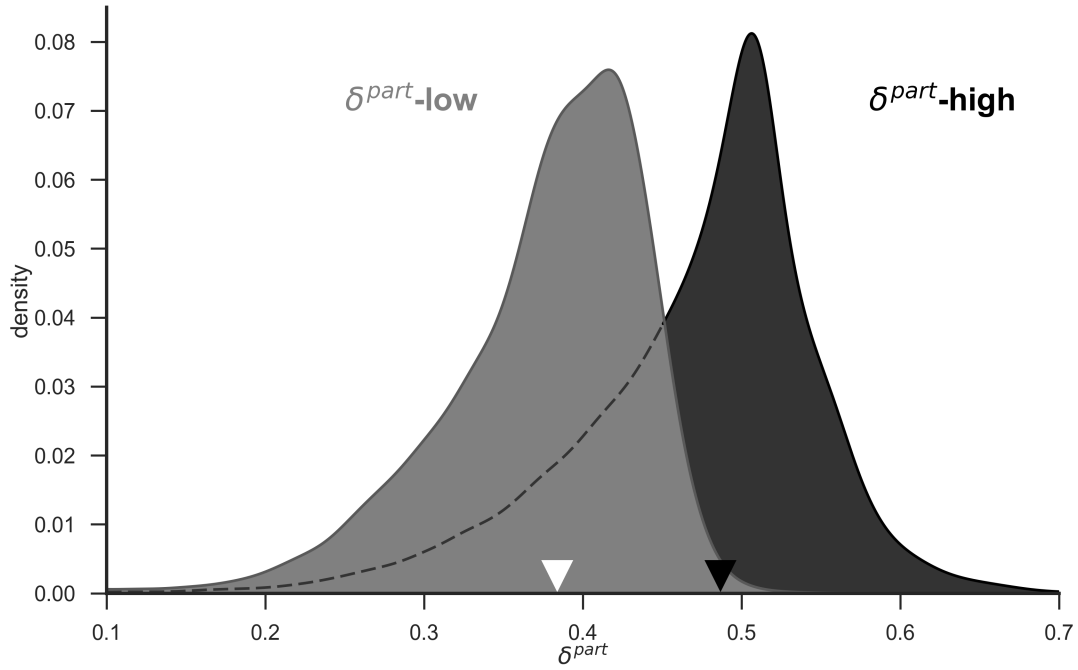

Figure 3.13: Averaged histograms of δ^{part} inside ice clouds ($\mathbb{R} > 3, T < 235K$) for the two groups 'δ^{part}-high' and 'δ^{part}-low' that correspond to the upper and lower row of Figure 3.12, respectively. Values above 0.45 are highlighted in black, medians are marked by a triangle.

320 hPa. Those stemming from the Mediterranean Sea and North Africa show pressures above 300 hPa. Typical aircraft cruise altitudes over the North Atlantic lie at 29 000 ft (315 hPa) and above. Over the mainland, aviation emissions happen also at lower altitudes during ascent and descent from and to the airports.

The trajectories can be compared to a map of black carbon emissions from civil aviation in 2005 (Figure 3.15) compiled by *Stettler et al.* (2013). Here, defined regions of high emissions can be recognized. They comprise the North Atlantic Tracks (NAT) to North America, the European mainland (connecting major cities), routes over the Iberian Peninsula to the Canary Islands and South America, and southeastern and eastern routes. Other parts of the region show much less black carbon emissions.

The 'δ^{part}-high' clouds M4, M12, and M14 formed in a very busy air traffic corridor connecting Central Europe with North America, In contrast, air masses in the 'δ^{part}-low' cases M8 and M9 originate from a more southern part of the Atlantic Ocean, featuring substantially lower emissions.

The trajectories for M7 and M11 look very similar at the first glance; however, M11 reaches its maximum ice water content (IWC, marked with a star) already at the North African Coast. Any emissions along the trajectory after that point might not influence the cloud, as no substantial further nucleation is expected. M7 reaches it maximum IWC over France, and its trajectory lies almost exactly along the air corridor from Central Europe to Madrid, the Canary Islands, and South America. Thus, the δ^{part} high case M7 might be affected by aviation emissions more heavily than the 'δ^{part}-low' case M11.

This co-occurrence of raised δ^{part} values and aviation emissions is less obvious for the Cases M5, M6, and M10, as all three originate from the relatively clean region over the Mediterranean Sea and North Africa. Still, the 'δ^{part}-low' case reaches maximum IWC more closely to the European mainland in the more emission affected region of Northern Italy.

The analysis identifies a connection between high δ^{part} values in cirrus clouds and the origin of air masses in regions with high aviation emissions. Clouds with lower δ^{part} stem from regions with low emissions. This effect is particularly strong for air masses that stem from the Atlantic Ocean.This demonstrates that aviation exhaust particles are a possible source of ice nuclei in the nucleation region of 'δ^{part}-high' clouds. Further it shows the absence of these particles in the 'δ^{part}-low' cases. When these particles act as ice nuclei, they may lead to early cirrus formation. The altered freezing conditions (relative humidity and temperature) would modify particle properties such as size, number concentration, and shape, and therefore also optical properties like the particle depolarization ratio which is especially sensitive to the crystal habit.

3.2.2 Differences in humidity distributions

In Figure 3.16, the distributions of RH_i inside 'δ^{part}-high' and 'δ^{part}-low' clouds are plotted. They are calculated by averaging over five normalized distributions for each group. This ensures that the resulting distribution is weighted by the number of independent observations rather than by the cross-section of the clouds. 'δ^{part}-high' clouds reach lower

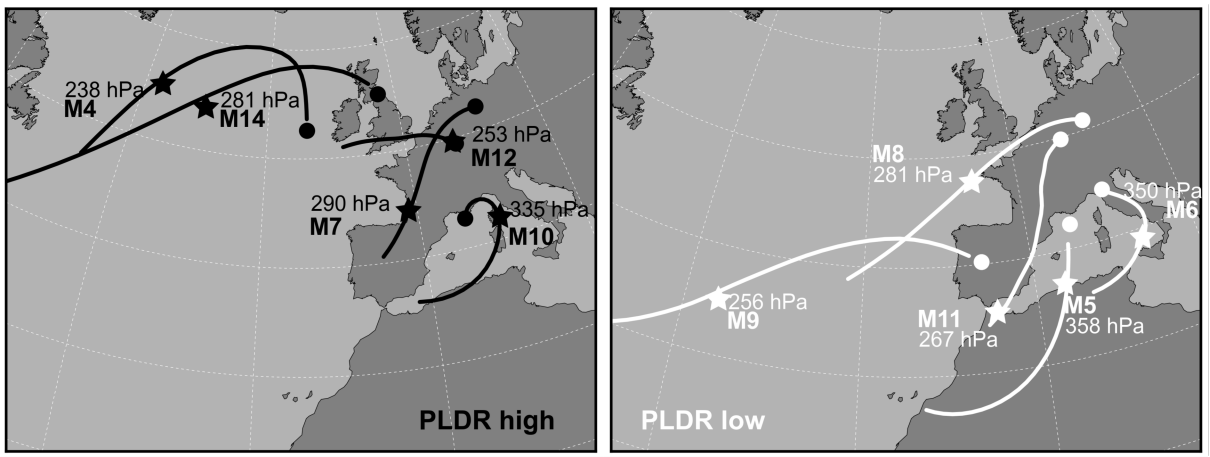

Figure 3.14: Location of measured cirrus clouds (dots), maximum cloud ice water content (stars), and the course of calculated backward trajectories for 'δ^{part}-high' cases (black) and 'δ^{part}-low' cases (white)

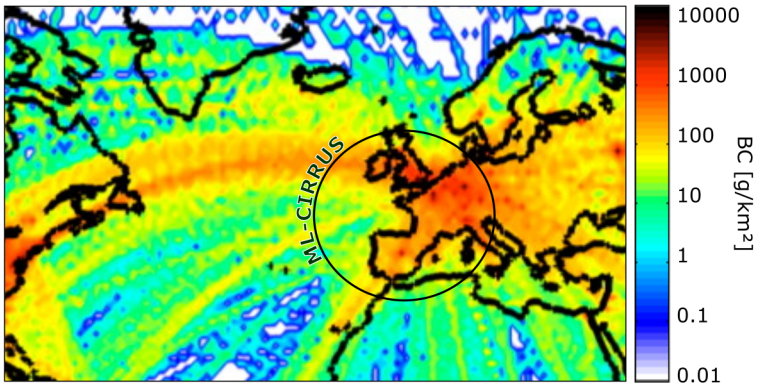

Figure 3.15: Map of black carbon emission from civil aviation in 2005 (modified version from *Stettler et al.* (2013, their Figure 4))

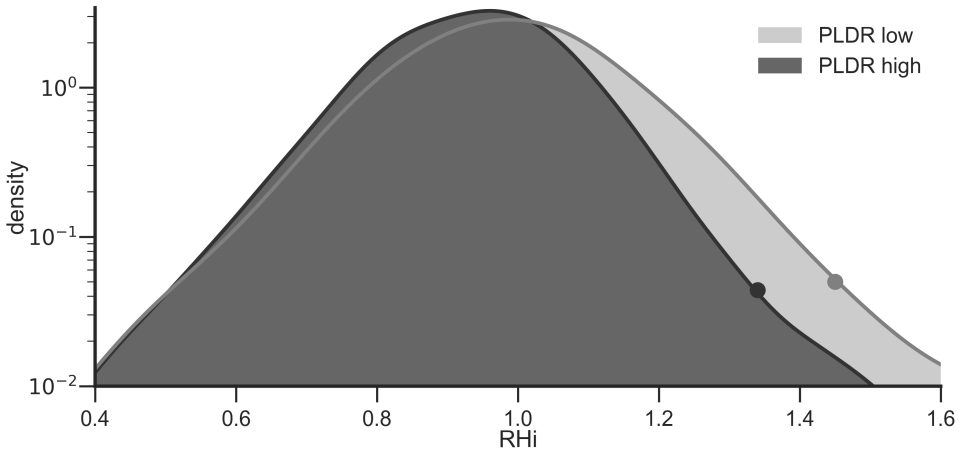

Figure 3.16: Distribution of relative humidity over ice (RH_i) averaged over cases in 'δ^{part}-high' and 'δ^{part}-low'.

supersaturations than 'δ^{part}-low' clouds. The 99.5th percentiles lie at 134 % and 145 %, respectively. The supersaturated fractions are 30 % for 'δ^{part}-high' and 41 % for 'δ^{part}-low'.

As the highest supersaturation observable in cirrus clouds is limited by the associated freezing threshold, these findings give reason to believe that the nucleation paths differ in both groups. Homogeneous freezing seems to play a much larger role in 'δ^{part}-low' clouds. Lower supersaturations are well in line with the existence of aviation soot particles in the 'δ^{part}-high' cases that can initiate heterogeneous freezing. From the difference in the 99.5th percentile, the heterogeneous freezing threshold for aviation exhausts can be roughly estimated to be 11 % below the homogeneous threshold under the assumption of pure homogeneous freezing in 'δ^{part}-low' and heterogeneous freezing in 'δ^{part}-high'.

The significance of the deviations between the two distributions can be verified by employing a statistical resampling method. When randomly choosing two groups of five cases each, from the ten mission flights and calculating their RH_i distributions as in Figure 3.16, the probability to observe a difference in the supersaturated fraction equal to or greater than the one found when grouping based on δ^{part} (11 %) is only 3.7 %. The probability to observe a difference in the 99.5th percentile equal to or greater than the one found when grouping based on δ^{part} (also 11 %) is only 1.9 %.

3.2.3 Differences in Microphysics

Traces of different freezing pathways should also be visible in direct measurements of microphysical parameters such as particle size and number concentration. Figure 3.17 shows distributions of effective diameter d_{eff} (a) and number concentration n^{part} (b) in 1-K temperature bins for 'δ^{part}-low' and 'δ^{part}-high' clouds measured by CAS and CIP (see section 2.2.3). This analysis concentrates on cold temperatures ($T < 215.5$ K) as differences should be strongest near nucleation regions. At temperatures below 213 K, 'δ^{part}-low'

distributions of d_{eff} peak around 16 µm at temperatures above that, the distributions become much broader with a large fraction of data above 50 µm. In contrast, 'δ^{part}-high' distributions peak at 24 µm below 210 K. At higher Temperatures the distributions become broader and shift towards larger diameters peaking around 80 µm below 212 K.

With increasing temperature, n^{part} tend to decrease in both cloud groups and the distributions develop long tails towards low concentrations. Below 214 K, 'δ^{part}-low' clouds have higher median number concentrations than 'δ^{part}-high' clouds. This is strongest between 208 K and 211 K, where 'δ^{part}-high' distributions show a median between 0.05 cm^{-1} and 0.12 cm^{-1}, and 'δ^{part}-low' distributions show a median between 0.15 cm^{-1} and 0.8 cm^{-1}, and even reach number concentrations of more than 5.4 cm^{-1} (99.5^{th} percentile).

From the RH_i distributions (section 3.2.2) it became clear, that homogeneous freezing plays a larger role in 'δ^{part}-low' cases. During homogeneous nucleation, water condensates on small aerosol solution droplets diluting them to the point where they can freeze. This is expected to produce high ice crystal number concentrations and small crystal sizes, due to the abundance of these solution droplets. During heterogeneous freezing, ice crystals form earlier on comparably less numerous solid aerosol particles at lower supersaturations. The available water vapor is deposited on a smaller number of ice crystals that in turn grow to larger sizes.

The found microphysical differences in the upper cloud regions ($T < 216$ K) can therefore be interpreted as the signature of more frequent heterogeneous freezing in 'δ^{part}-high' cases that produces fewer and larger ice particles than in 'δ^{part}-low' cases. This also agrees well with differences in the supersaturation found in the two groups and with the different aviation exhaust aerosol load in the air masses.

The number concentration and crystal size (except for very small particles, see section 3.1.3) is not expected to affect δ^{part} directly, as it is mostly influenced by crystal shape. However it is known that temperature and relative humidity during the nucleation determines the ice habit (*Bailey and Hallett*, 2009). Therefore heterogeneous freezing in 'δ^{part}-high' cases which already occurs at lower supersaturation and temperatures might well lead to altered crystal shapes and could therefore explain the raised δ^{part} values.

3.2.4 Other potential influences

During the campaign preparation and realization, other factors were thought to have an influence on δ^{part}. First, there is a well-known temperature dependence. Second, several flights were dedicated to cirrus forming from warm conveyor belts (see section 2.2.1). This very specific formation process was speculated to influence δ^{part}. Third, contrails were reported to show on average higher δ^{part} than surrounding cirrus. In this subsection I will examine these influences.

Temperature dependence

The depolarization ratio of midlatitude cirrus is known to increase with decreasing temperatures (*Sassen and Benson*, 2001). This is typically explained by the depolarization

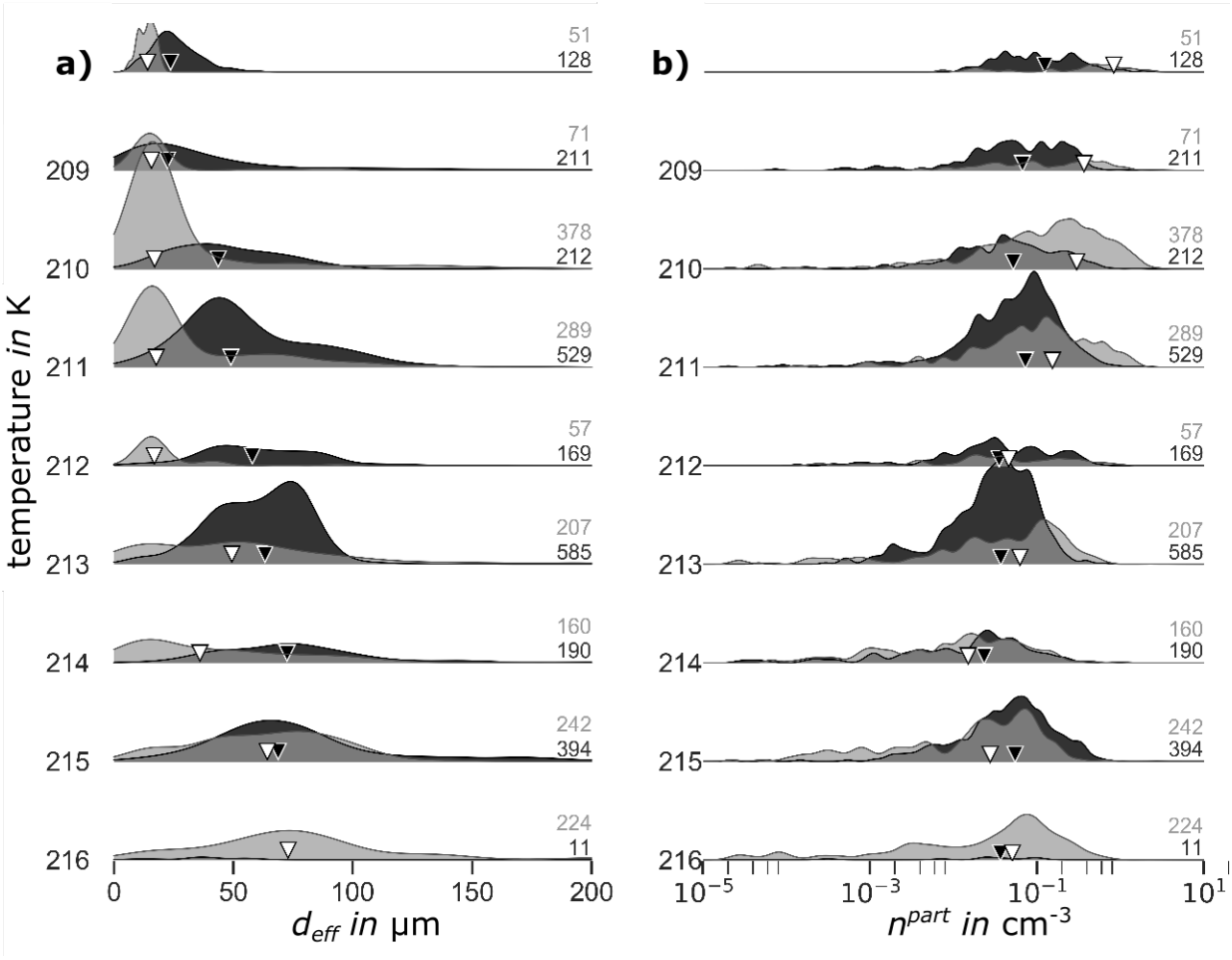

Figure 3.17: Distributions of ice effective diameter d_{eff} (a) and number concentration n^{part} (b) in 1-K temperature bins for 'δ^{part}-low' (blue) and 'δ^{part}-high' (red) cases. Triangles mark the median of each distribution.

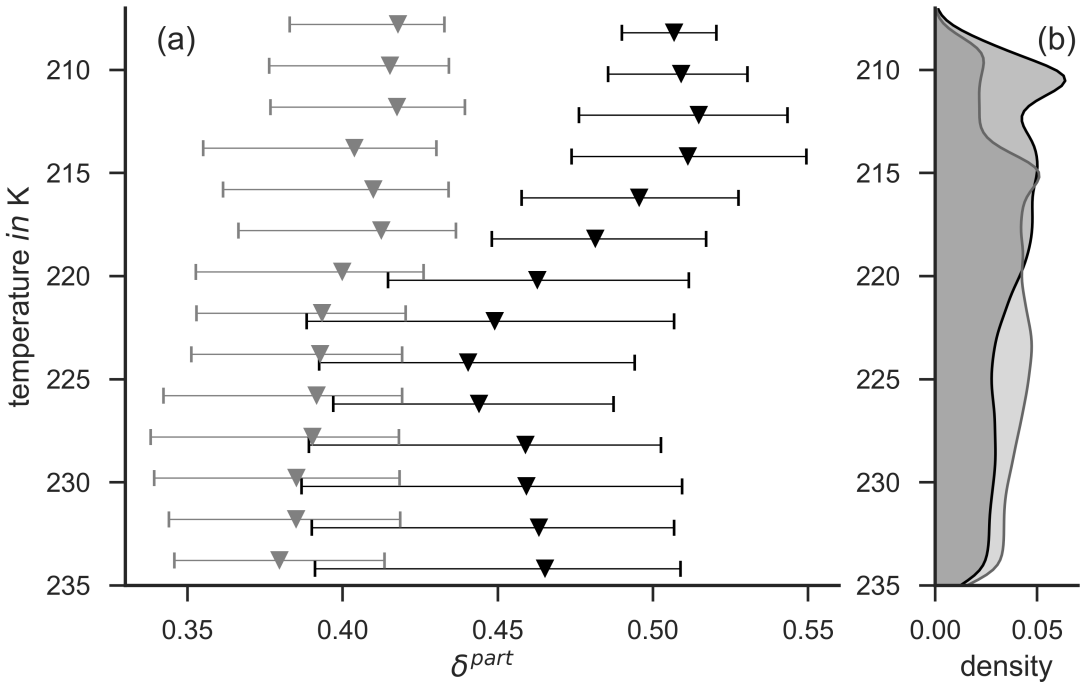

Figure 3.18: (a) median (triangle) and IQR (horizontal bars from 25$^{\text{th}}$ to 75$^{\text{th}}$ percentile) of δ^{part} distributions in 2-K temperature bins and (b) temperature distribution for 'δ^{part}-low' (grey) and 'δ^{part}-high' (black) cases.

ratio of different ice habits located at different temperature levels. According to that, higher depolarizations at lower temperatures arise from columnar particles found at these temperatures. In contrast, plate-like particles dominating lower parts of the clouds, lead to lower depolarizations. Therefore the two δ^{part} groups could theoretically be the result of different cloud temperatures, where 'δ^{part}-high' clouds are located at colder temperatures than 'δ^{part}-low' clouds.

In Figure 3.18(a), median and IQR of δ^{p} distributions in 2-K temperature bins are plotted for 'δ^{part}-high' and 'δ^{part}-low' cases. The coldest temperature that is observed in cirrus is 207.8 K. Both groups show a negative temperature trend, which is stronger in 'δ^{part}-high' cases than in 'δ^{part}-low' cases. The spread in δ^{part} between the groups is very clear at all temperature levels, however it is strongest below 220 K. 'δ^{part}-high' clouds are mostly concentrated in the temperature range between 207 K and 220 K (Figure 3.18(b)). In contrast, 'δ^{part}-low' clouds show a strong representation mostly from 215 K to 230 K but reach the same cold temperatures.

From this it is clear that the two δ^{part} groups are not caused by sampling clouds at different temperatures. A temperature trend is observed in both groups but the mode splitting in δ^{part} exists at all temperature levels. The concentration of 'δ^{part}-high' clouds at colder temperatures that coincide with typical aircraft cruising levels can rather be taken as a further indication for the importance of aviation emissions in the 'δ^{part}-high' cases.

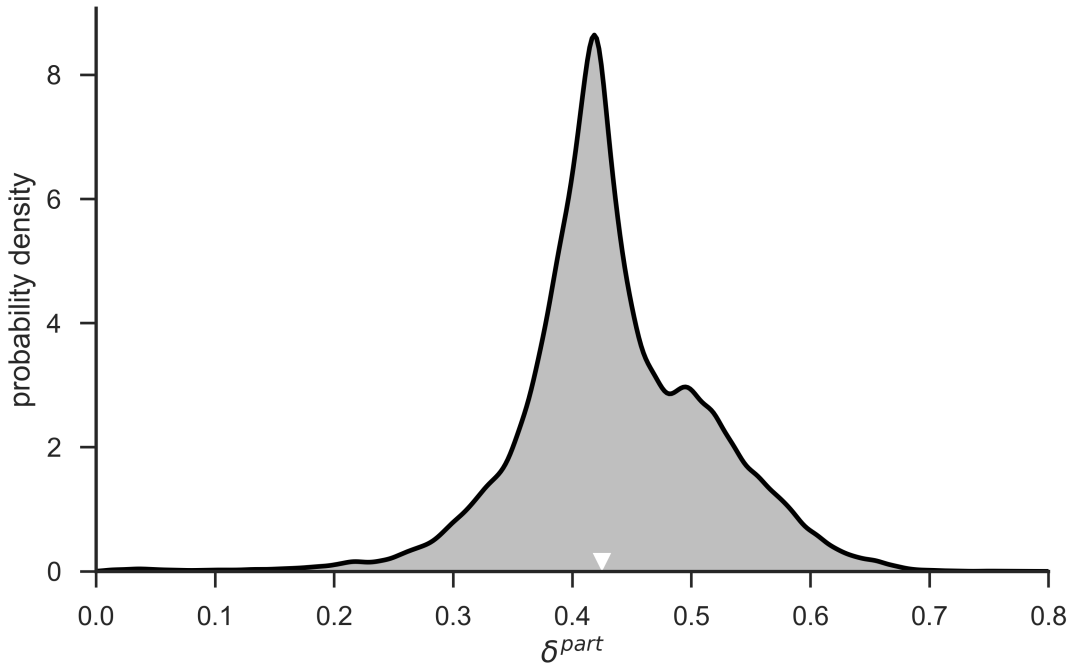

Figure 3.19: Distribution of δ^p for the four WCB cases measured during ML-CIRRUS (M5, M6, M10, and M14), the white triangle marks the median.

Cirrus formation in warm conveyor belts

A warm conveyor belt (WCB) is a distinct flow structure typical for the midlatitudes that leads to increased precipitation along its trajectory (*Eckhardt et al.*, 2004). In warm conveyor belts, warm humid air from low in the troposphere ascends over several kilometer to higher levels of the troposphere. During this ascent, liquid clouds form and freeze eventually to form pure ice clouds. Additionally, higher air layers can be lifted by this ascent from below leading to direct ice nucleation. This formation process has been shown to cause distinct microphysical properties in the clouds (*Krämer et al.*, 2016).

During ML-CIRRUS four cases of WCB cirrus were measured (M5, M6, M10, and M14). In Figure 3.19, their depolarization ratio distribution is plotted. It has a mean (median) of 0.434 (0.425) and an IQR of 0.09. Values reach from below 0.17 to more than 0.65 (0.5^{th} and 99.5^{th} percentile). This is similar to the distribution of all cirrus cases (see section 3.1.3). The main difference lies in the relative strength of the two modes. In the WCB cases the higher mode is much weaker than in the overall distribution, but it is still clearly discernible. No feature in δ^{part} can be found that would categorically distinguish the four WCB cases from other cirrus.

To illustrate the existence of both modes in the WCB subgroup, I investigate two WCB cases in more detail (M5 and M14). Both clouds have an higher-than-average subsaturated fraction (68 % and 70 %) and lower-than-average DEP (24 % and 23 %) and HET+HOM

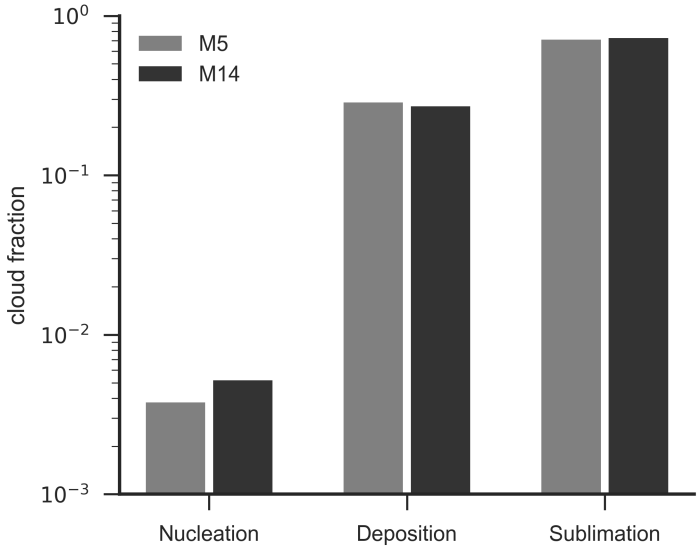

Figure 3.20: Fraction of the cloud that was classified as a region where nucleation (HOM+HET), crystal growth by water vapor deposition (DEP), or sublimation of ice crystals (SUB) is occurring for M5 and M14.

fraction (9 % and 7 %) (see Figure 3.20).

This indicates that both clouds are in an equally late life-cycle state at the time of measurement (compare section 3.1.2). Despite these similarities, they show unexpected differences in δ^{part}. Their cross-sections are plotted in Figure 3.21. M14 shows very high δ^{part} values of up to 0.7 at the top and in the lower parts of the cloud. In contrast, M5 features δ^{part} values below 0.05 at the cloud top and values in the rest of the cloud do not surpass 0.55. It can be concluded that the formation in this specific meteorological situation of a WCB does not determine the shape of δ^{part} distributions.

Possible contributions from contrails

It is already well established that contrails show slightly elevated δ values compared to natural cirrus clouds (*Freudenthaler et al.*, 1996; *Iwabuchi et al.*, 2012). Therefore one might readily think of contrails as the causing factor of higher depolarizations in cirrus clouds that stem from air traffic corridors. During ML-CIRRUS the mission flights M4, M7, M11, and M12 were specifically planned and executed to measure contrails. The existence of contrails in the encountered clouds was predicted by forecast tools and verified by in-situ measurements. The distribution of depolarization of these cases is plotted in Figure 3.22. It has a median (mean) at 0.46 (0.44) which is between the values for 'δ^{part}-high' and 'δ^{part}-low' and the IQR is 0.12. With M4, M7 and M12 belonging to 'δ^{part}-high', the higher mode is stronger than the low mode. Nevertheless, the double mode still exists.

To illustrate the existence of contrails in both groups two cases are examined more

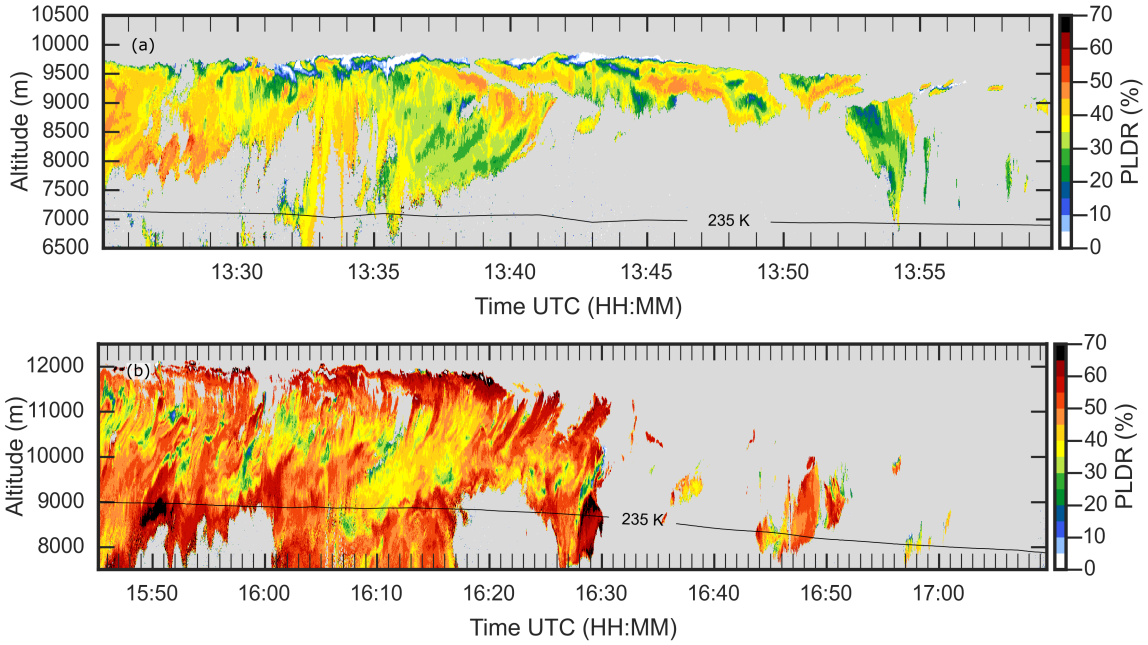

Figure 3.21: Lidar cross-sections of δ^p for the two WCB cases M5 (a) and M14 (b).

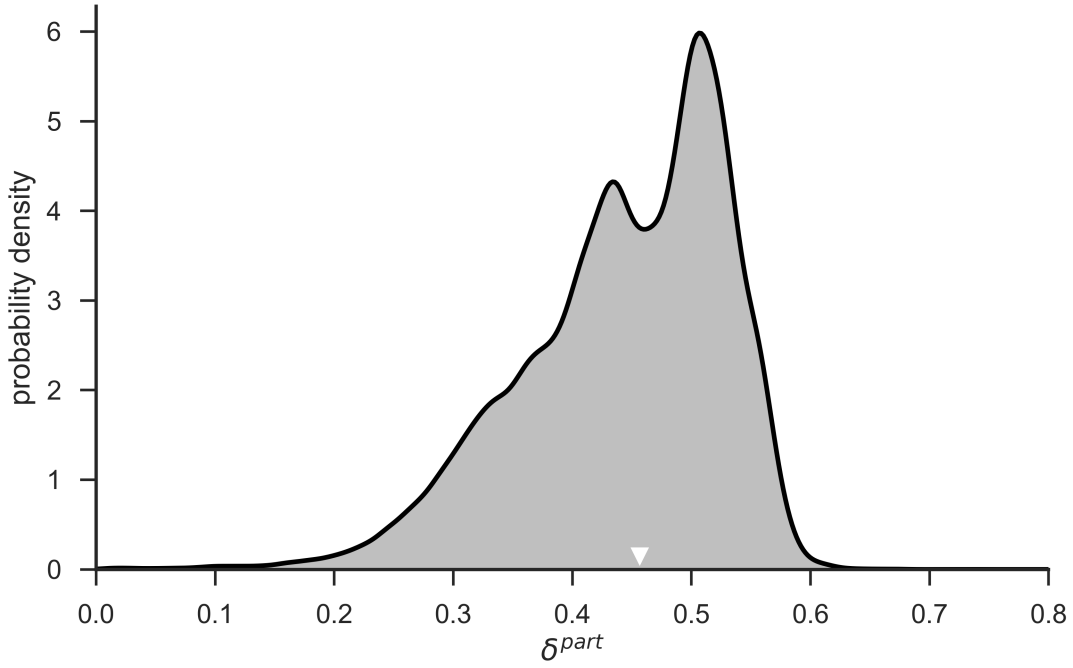

Figure 3.22: Distribution of depolarization ratio of all contrail cases, the white triangle marks the median.

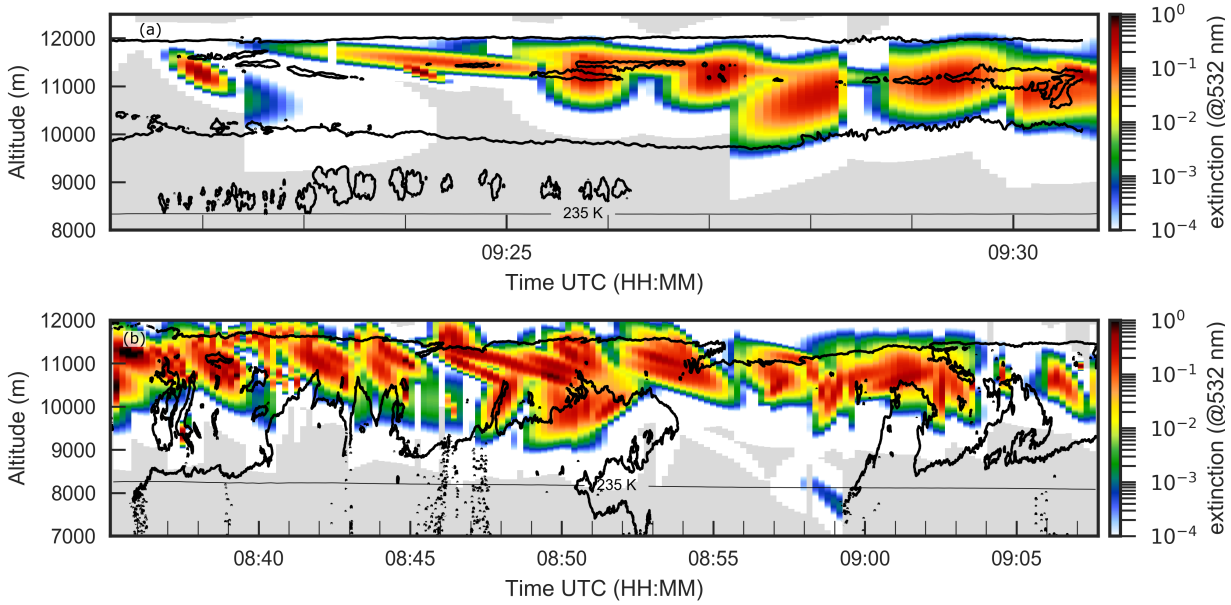

Figure 3.23: Results from CoCiP simulating the extinction from contrails as seen by a 532 nm lidar system for M4 (a) and M11 (b). The borders of the measured cirrus clouds are marked by a black contour line.

closely. M4 was measured in the region of the North Atlantic Tracks that bundle the traffic between Europe and North America. M11 was measured over Germany. Figure 3.23 shows the simulated extinction as would have been seen by a 532 nm lidar system caused by contrails for both cases. The contrails were simulated with CoCiP from actual air traffic data up to 24 hours before the measurement flight. In the cloud area (black contour) many contrails can be seen. M11 seems to be slightly more affected by contrails than M4.

Figure 3.24 shows the depolarization cross-sections of both cases. M4 features high depolarization values up to 0.65. Although M11 is heavily affected by contrails, δ^{part} barely reaches values of 0.5. These findings show that contrails do not influence the clouds δ^{part} distribution significantly on a large scale. If an influence on δ^{part} exists, it seems to be limited to confined areas and therefore not relevant for the over all distribution. This strengthens the hypothesis of cirrus formation by subsequent heterogeneous freezing on exhaust particles. Nevertheless, these particles might well be residuals from evaporated contrail ice crystals (see section 4.2.2).

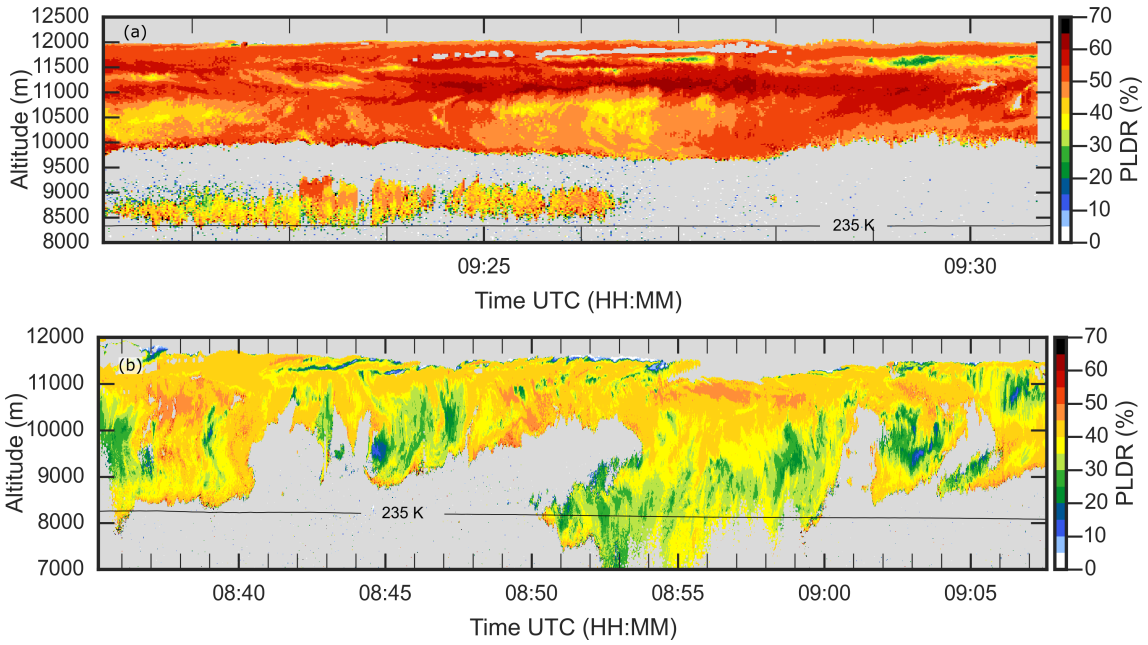

Figure 3.24: Lidar cross-sections of δ^p for two contrail cases M4 (a) and M11 (b)

Chapter 4

Discussion

4.1 Cirrus characteristics

Airborne lidar profiling has proven itself an efficient tool for characterizing cirrus clouds. With one cirrus overpass, complete cloud cross-sections can be recorded that include cloud top and edge regions. In order to represent these regions adequately with in-situ measurements, the flight altitude has to be adapted to the given situation which is not always possible due to the necessary coordination with air traffic control. Limitations of lidar profiling occur in optically thick cirrus that can only be penetrated to a certain range before all light is attenuated. Another limitation arises from the high dynamic range of the returning light signal. The r^{-2} dependency of the backscatterd light can lead to saturation of the highly sensitive avalanche photo diode and photo multiplier sensors when the distance between the cloud and the aircraft is too small. Due to HALO's ability to reach flight altitudes of up to 15 km this can be avoided in many cases. Despite that, detector overflow still happened in confined cloud areas in almost all recorded cirrus cases, especially at the cloud top region. Additional low-sensitivity channels in the lidar receiver would solve this problem and render WALES even more suitable for cirrus studies.

Relative humidity with respect to ice

The subsaturated fraction of measured cirrus clouds is 62.5 %. The existence of such large subsaturated cirrus regions might be counter intuitive at first glance, as ice crystals are in a dissipating state there. However, cirrus are routinely observed in subsaturated conditions (*Ovarlez et al.*, 2002; *Spichtinger et al.*, 2004; *Kübbeler et al.*, 2011; *Kaufmann et al.*, 2018) and evaporation simulations of thin cirrus revealed dissipation times of several hours for larger particles and small number concentrations (*Kübbeler et al.*, 2011). This makes clear that subsaturated cloud regions can make up a large fraction of the total cloud cross-section. In all, the findings concerning relative humidity in midlatitude cirrus clouds confirm the general expectations laid out by earlier studies.

The results from lidar data also compare well to in-situ measurements of relative humidity taken with the Atmospheric Ionization Mass Spectrometer AIMS and the tunable

diode laser hygrometer SHARC (Sophisticated Hygrometer for Atmospheric ResearCH) during ML-CIRRUS. They show mean values of 97 % and 94 % with IQR of 15 % and 8 %, respectively (*Kaufmann et al.*, 2018).

The slightly higher variability found in lidar data compared to in-situ data could be explained by the different sampling volumes. Where Lidar measures complete cross-sections through the cirrus, including regions with extreme humidities at the cloud top, base and edges, the sampling volume of in-situ instruments depends on the chosen flight altitudes. For in-situ measurements, this could potentially induce a bias towards oversampling central parts of the clouds with supposedly more moderate humidities.

Depolarization ratio

The strength of the presented characterization of depolarization ratio is that, unlike many earlier studies, it investigates the details of δ^{part} distributions. This is facilitated by the high accuracy of depolarization measurements achieved by the WALES lidar system (*Esselborn et al.*, 2008; *Freudenthaler et al.*, 2009). I was able to extract information from the variability within a cloud and from cloud to cloud. This revealed the role of extremely small particles at the cloud top and edge, and their influence on depolarization ratio.

The most significant finding however is the existence of two groups of natural cirrus clouds that form two modes at $\delta^{part} = 0.4$ and $\delta^{part} = 0.5$. To my knowledge cirrus depolarization has not been investigated in this way before and therefore this grouping stayed undiscovered until now. This discovery was published in *Urbanek et al.* (2018).

The fact that classified evolution stages, i.e. nucleation growth and evaporation, do not influence the δ^{part} distributions significantly, was surprising. It indicates that effects from changing crystal size are only relevant in the very early and late ice crystal life-cycle and are therefore insignificant for the distribution of whole clouds. Further, it shows that the crystal habit, which strongly influences δ^{part}, does not seem to change a lot during the life-cycle. Effects like the disappearance of facets and corners during sublimation (*Korolev and Isaac*, 2006) or ice crystal aggregation either are not relevant for cold ice clouds ($T < 235\,\mathrm{K}$) or do not influence δ^{part} significantly.

4.2 Indirect aerosol effect

4.2.1 Quantifying the aviation impact

The analysis of cloud trajectories can only deliver a qualitative co-occurrence of 'δ^{part}-high' cases and their origin in air traffic regions. It would be desirable to find a quantitative measure for the impact of aircraft exhaust on cirrus clouds. For this, spatial and temporal information on the aircraft exhaust is needed. In an impromptu approach the in-house available CMIP5 monthly-mean anthropogenic emissions (*Lamarque et al.*, 2010, Coupled Model Intercomparison Project - Phase 5) that also specifies aviation emissions was used to determine the impact in the formation region of the clouds. As a rough estimate, black

carbon emissions were evaluated at the location of maximum ice water content along the backward trajectories (marked with stars in Figure 3.14).

The aviation impact was derived from simulations by *Righi et al.* (2013). For this, the global model system EMAC (*Jöckel et al.*, 2005, ECHAM/MESSy Atmospheric Chemistry) including the aerosol submodel MADE (*Ackermann et al.*, 1998, Modal Aerosol Dynamics model for Europe) was employed. The version applied here features a horizontal grid spacing of 2.8° by 2.8° in longitude and latitude at 19 vertical levels from the surface up to 10 hPa. The aviation impact was determined by taking the difference between a reference and a sensitivity simulation, where emissions from aircraft were set to zero. It is spatially interpolated (nearest-neighbor) from the grid boxes to the location specified by the cloud trajectories and linearly interpolated to the corresponding pressure level. The 12-hourly model output is averaged for each April of 15 simulated years (1996 to 2010).

Figure 4.1 shows the correlation between the aviation induced black carbon at the location of maximum IWC and the median δ^{part} of the measured cirrus. 'δ^{part}-low' cases show BC concentrations around 0.9 ng m^{-2}, 'δ^{part}-high' cases values around 1.5 ng m^{-2}. However individual missions can exhibit similar concentrations even though they are in different groups (M7 and M11).

The weaknesses of this ad-hoc approach are the inability to locate the exact formation region due to insufficiently detailed modeling of cirrus clouds in the trajectory calculations, and the inability to represent the actual black carbon pollution at the date of the measurement flight, due to the climatologic emission data base. In order to represent the aviation impact appropriately, an episodic modeling approach has to be employed. The BC emissions used, ideally come from realistic daily emission data. They should be weighted by the number of newly forming ice crystals and accumulated along the cloud trajectory to form a measure for the aviation impact. Such sensitivity studies could also consider aging and pre-activation effects (see section 4.2.2). However, this would clearly go beyond the scope of this study.

4.2.2 What is the relevant soot type?

It is a well established fact, that soot particles are able to act as ice nuclei (*DeMott et al.*, 1999; *Alcala-Jornod et al.*, 2002; *Möhler et al.*, 2005; *Arienti et al.*, 2018; *Mahrt et al.*, 2018). However different methods employed to produce the soot for laboratory freezing experiments deliver different types of soot which makes it difficult to compare their results. Soot varies in its composition and size. It can be coated by sulfuric acid or contain metal compounds or residues from lubrication oil and organics. The large variability of experimental freezing results implies that the ability of soot to form ice in the atmosphere is still poorly understood (*Mahrt et al.*, 2018).

The difference in the 99.5$^{\text{th}}$ percentile of RH_i in the 'δ^{part}-high' and 'δ^{part}-low' group is 11 %. As the highest supersaturations that are reached inside cirrus clouds are determined by the freezing onset threshold of the relevant nucleation pathway, a rough estimate of the freezing threshold for the ice nuclei in 'δ^{part}-high' could be 11 % below that of homogeneous freezing. That would be around 145 % relative humidity over ice, depending on the

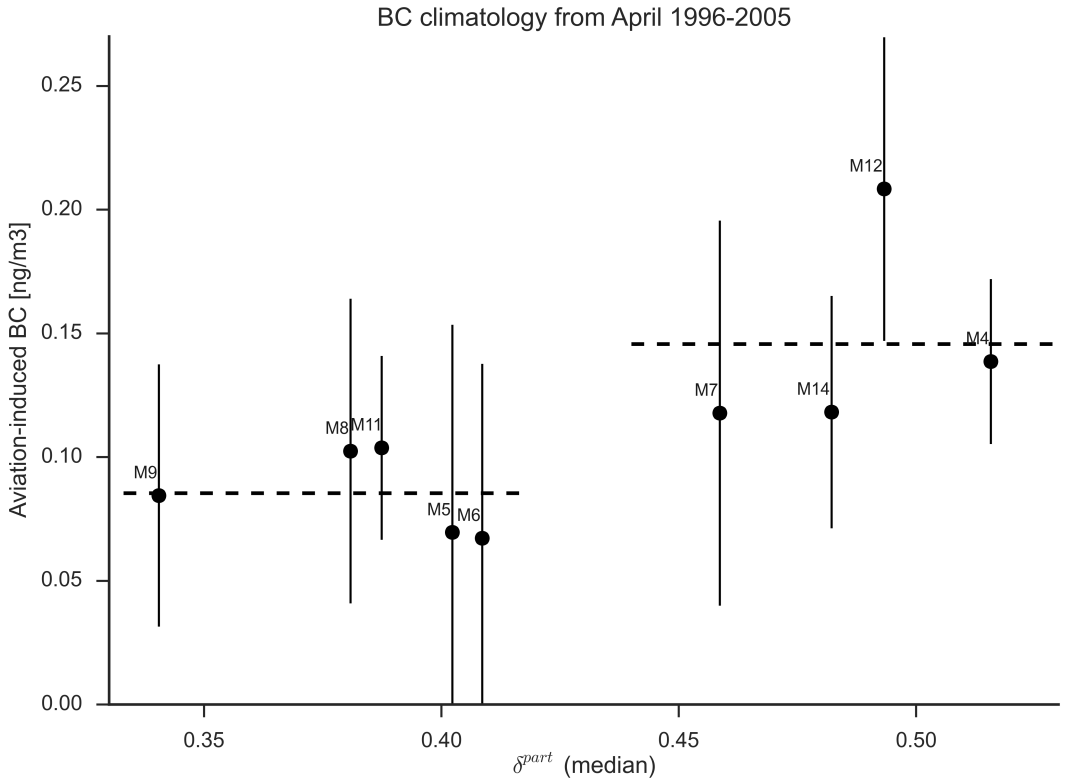

Figure 4.1: Correlation of black carbon and δ^{part}. Dots give the median over 15 years, and vertical bars the 1-sigma inter annual model variability. The dotted lines give the average black carbon concentration for the groups 'δ^{part}-low' and 'δ^{part}-high'.

temperature. Of course this is only true, assuming that 'δ^{part}-low' clouds nucleated purely homogeneously and 'δ^{part}-high' clouds nucleated heterogeneously.

Such a freezing threshold would correspond well to recent laboratory results from *Mahrt et al.* (2018) for soot particles of sizes bigger than 200 nm. As most of the freshly emitted aircraft soot is significantly smaller (<100 nm) (*Moore et al.*, 2017), they seem to be irrelevant as ice nuclei in an indirect aerosol effect. This would explain how cirrus clouds that contain fresh contrails and freshly emitted soot can show low depolarization ratios (compare section 3.2.4).

Aggregation of soot can produce larger particles. Thus, aviation soot at a certain aging level that grew to more than 200 nm seems to be a likely ice nuclei candidate that could explain the findings of this study. For that, the corresponding air masses need to collect soot hours before the nucleation. The analyzed trajectories only go back 24 h from the time of the cirrus measurement (see Figure 3.14). However they indicate that the air was located in air traffic regions even before that: Over North America (M4 and M14), NAT (M12), and the air corridor towards South America (M7). From that the timescale of the aging process can roughly be estimated in the order of one day. This aging hypothesis conforms with the second scenario proposed by *Kärcher et al.* (2007) where low concentrations of particles formed by coagulation of emitted soot with background aerosols could significantly reduce the ice crystal number.

The ice nucleation on soot is associated with a core condensation and freezing process, where water condenses in pore-like cavities of the soot particles already at water subsaturation (*Marcolli*, 2014) and subsequently freezes. Ice can survive in these pores even in an subsaturated environment. This led to the discussion of a pre-activation effect in literature: Contrail ice particles that enclose soot, could release pre-activated particles with surviving pore ice that could feature reduced freezing thresholds (*Zhou and Penner*, 2014; *Marcolli*, 2017). This is another probable ice nuclei candidate which agrees well with the finding of nucleation regions in areas with high soot emissions from aviation. But for now, non of the two options, pre-activation or aging, can be excluded.

4.2.3 Climate impact

In our data, five out of ten statistically independent cloud cases, measured at nine flight days during a period of 17 days, show elevated δ^{part}. The clouds dominated large areas over Europe at the time of their measurement. The fraction might be biased by the employed flight planning strategies, as three of the affected flights were dedicated to investigating contrail cirrus, and therefore, the flights took place in high air traffic regions. Nevertheless, in at least 29% of the days of the campaign this cloud type could be found over Europe. This indicates that an indirect aerosol effect might occur frequently at least in the northern midlatitudes over Europe.

The global climate impact of natural cirrus clouds is $\sim$4.5 W m^{-2}, over Europe it is even up to 10 W m^{-2} (*Gasparini et al.*, 2017). Already a very small modification of the cloud radiative forcing by the indirect aviation effect would result in changes comparable in size to the anthropogenic forcing associated with CO_2 emission from aviation that was

determined at 35 mW m^{-2} (*Boucher et al.*, 2013). This illustrates the strong potential of this effect to influence the climate.

I found lower freezing thresholds for the affected clouds which could lead to a larger cloud cover. However this could be compensated by faster sedimentation due to larger ice crystals (section 3.2.3). Before the process is not investigated in more depth no reliable statements on the actual climatic effect can be made.

4.2.4 Recommendations for future campaigns

In order to investigate an indirect aerosol effect in more detail, future measurement campaigns must focus on the nucleation regions. Characterizing the aerosol load there and the ice residuals from newly formed cirrus could provide the information needed to identify the relevant ice nuclei. Special attention should be given to the role of fresh and aged soot and to pre-activation effects. From accurate measurements of supersaturation in- and outside of cirrus clouds, the corresponding freezing threshold could be determined.

In-situ measurements of the crystal shape would help to identify the microscopic causes of the altered depolarization ratio. As the δ^{part} is apparently especially sensitive to the indirect aerosol effect, a depolarization lidar could act as a pathfinder instrument during the flights, identifying affected clouds. Finally, a characterization of the microphysical properties such as crystal size, number concentration and ice water content would provide the observational basis to represent affected clouds realistically in climate models.

Mission accompanying episodic modeling of the aerosols and cirrus clouds that resolves daily and even diurnal changes in aviation emission patterns could support the flight planning and facilitate the interpretation of the measurements in the larger meteorologic context.

4.3 Assessment of measurement uncertainties

Relative humidity

The difference in the supersaturations reached in 'δ^{part}-high' and 'δ^{part}-low' clouds is 11 % (see section 3.2.2). This is in the order of the accuracy of WALES for individual measurements. In order to reinforce the validity of the finding, the individual sources of systematic error in RH_i measurements must be considered.

The accuracy of the water vapor mixing ration measurement is 5 % and comprises uncertainties in the definition of the water vapor absorption cross-section, in the air density profile, and from the calibration of the DIAL wavelengths (*M. Wirth*, pers. com., July 17, 2019). However, these errors do not change from cloud case to cloud case and can therefore be neglected when investigating relative differences between measurements in two clouds.

The other inaccuracy in RH_i stems from temperature. It is taken from the ECMWF model (6-hourly analysis data interpolated in time and space onto the lidar cross-section). Unfortunately no independent temperature measurements are available for the ML-CIRRUS cases to validate the model at the location of lidar water vapor measurement in the cloud.

During a research flight in 2010, *Groß et al.* (2014) found a mean deviation between onboard temperature sensors and ECMWF model data of 0.8 K at cirrus levels. Assuming that the onboard sensors measured temperature with absolute accuracy and further assuming that the 2010 case is comparable to the ML-CIRRUS flights, this would translate into a relative systematic error of ∼10 % at cirrus temperatures.

The examined distributions (Figure 3.16) are averages of distributions from five independent cloud cases. Only if the ECMWF model would systematically overestimate temperatures in 'δ^{part}-high' cases, or underestimate it in 'δ^{part}-low' cases, a difference of 11 % could be explained only by measurement uncertainties.

However, when assuming that temperature deviations occur randomly from cloud case to cloud case in the model, the systematic error for the mean value of the joined RH_i distributions of 'δ^{part}-high' and 'δ^{part}-low' would be reduced by a factor of $\sqrt{5}/5$ to 4.5 % making it unlikely that the differences were produced by measurement uncertainties.

The fact that RH_i results are well in line with findings from in-situ measurements (section 3.2.3), gives additional confidence in the validity of the RH_i data.

Particle linear depolarization ratio

The ±45°-calibration method that is routinely applied during research flights assures a high accuracy in δ^{part}-measurements (see section 2.1.3). However, absolute deviations of up to 5 % can occur from calibration to calibration. The magnitude of these deviations arises randomly. Averaging over several cloud cases (as in Figure 3.13) therefore would merely lead to a broadening of the distribution and not to the formation of two distinct modes. The mode and median distance of 10 % cannot be explained solely by measurement inaccuracies.

Chapter 5

Conclusions

The objective of this study is to characterize the optical properties and humidity distribution of midlatitude cirrus clouds and to find observational evidence of an indirect aviation effect on natural cirrus clouds. For this, data from the airborne lidar system WALES that was employed during the ML-CIRRUS flight campaign is analyzed. During the campaign, more than $8000\,\mathrm{km}^2$ of cirrus cloud cross-section from ten independent cirrus cases was recorded by lidar.

In order to investigate the impact of cloud evolution, a classification scheme is developed that identifies nucleation, crystal grows, and ice sublimation regions within cirrus clouds. It is based on lidar measurements of backscatter ratio, water vapor concentration and model temperature information. Freezing onset parameterizations are used to determine nucleation regions.

The applicability of the classification is demonstrated in a case study of a cirrus cloud that was observed in a complex meteorological situation comprising a thick aerosol layer, large-scale dynamics, and mesoscale gravity lee waves. Here it reveals a nonstandard horizontal order of the classified evolution stages and helps to identify the influence of underlying wind and gravity wave conditions as well as large-scale dynamics on individual parts of the cloud.

The characterization of midlatitude cirrus clouds shows humidity distributions that agree well with previous studies and with in-situ measurements during the campaign. The median of relative humidity is slightly below saturation which means that the majority of the cloud cross-section (62 %) is subsaturated. Supersaturation of more than 150 % shows that homogeneous freezing plays a role at least in some of the clouds. The airborne lidar system has been proven to be an efficient tool for characterizing the relative humidity in cirrus cloud cross-sections.

The analysis of cirrus depolarization ratio reveals that very small ice particles ($<2\,\mu\mathrm{m}$) at the cloud top, edges and base can produce extreme δ^{part} values (< 0.16 and > 0.63). Apart from this, no significant influence of the classified evolution stage on the overall δ^{part} distribution of cirrus clouds is found. It can be concluded that changes in the ice crystal size are only relevant in the very early and late ice crystal life-cycle and are therefore insignificant for the distribution of whole clouds. As δ^{part} is specifically sensitive to the

crystal shape, this also implies that the life-cycle has no significant impact on the ice habit, at least in these cold cirrus clouds ($T < 235\,\mathrm{K}$).

The inter-cloud variability of δ^{part} reveals the existence of two groups. They form two modes at $\delta^{part} = 0.4$ and $\delta^{part} = 0.5$. To my knowledge nobody has observed this grouping of clouds in depolarization ratio before. Results from the investigation of an indirect aviation effect in section 3.2 answer the research question from section 1.4:

RQ1: Can features in optical cirrus properties be associated with an indirect aerosol effect from aviation?

The fact that whole clouds show shifted δ^{part} distributions (cloud cross-sections of up to $1400\,\mathrm{km}^2$), indicates that they were influenced by a large scale effect. The analysis of backward trajectories reveals a co-occurrence of elevated δ^{part} in cirrus clouds with the origin of air masses in regions of high soot emissions from aviation. This shows that aircraft soot is a probable source of ice nuclei in these cirrus cases. Lower supersaturation found in the affected clouds can be interpreted as the trace of heterogeneous freezing.

It is plausible that the lower supersaturation during the nucleation process leads to altered crystal shapes. This could explain the elevated depolarization ratio. Larger ice crystals and lower number concentrations, revealed by in-situ measurements in the same clouds, are also in good agreement with heterogeneous freezing as opposed to homogeneous freezing. Probable types of ice nuclei are aged soot with diameters larger than 200 nm or soot that was pre-activated in contrails.

Other possible influences like the cloud evolution stage, temperature, cloud formation in the specific meteorologic environment of a warm conveyor belt, or contrails embedded in the clouds are proven to have no impact or play a secondary role. From all this, the group of clouds with high δ^{part} distributions can reasonably be associated with an indirect aerosol effect from aviation.

RQ2: How are ice supersaturation and microphysical properties modified in affected clouds?

The group of clouds that feature high δ^{part} values and were associated with the indirect aerosol effect show distinct properties. They feature a larger subsaturated fraction by 11 % and reach less strong supersaturations compared to δ^{part}-low clouds. The median particle size is significantly larger and number concentrations do not reach high values observed in δ^{part}-low cases.

As these large, affected clouds were observed frequently, only a small modification of the clouds radiative forcing would already render the indirect aerosol effect a considerable anthropogenic climate impact. The lowered freezing threshold and enlarged ice crystals could change the cirrus cloud cover over Europe.

It is found that in order to quantify the aviation impact on cirrus clouds with model simulations, realistic emission data with high spatial and temporal resolution is needed.

Future flight campaigns would benefit from such episodic modeling. The ML-CIRRUS research flights did not focus on indirect effects; therefore, crucial information at the cirrus formation regions was not explored in detail. For a deeper investigation, a mission strategy could include the characterization of the aerosol load in cirrus formation regions, the measurement of microphysical and optical properties of the emerging clouds and the measurement of the supersaturation and updraft velocity distribution during ice nucleation. This way, future flight campaigns can provide in-depth observational data, facilitating investigations of the type of soot responsible for nucleation, the exact freezing threshold of these ice nuclei, and the extent and climatic impact of the indirect aerosol effect on cirrus clouds.

List of Figures

List of Tables

Abbreviations and Symbols

List of Abbreviations

Abbreviation	Long form
AIMS	Atmospheric Ionization Mass Spectrometer
BC	Black Carbon
CALIPSO	Cloud-Aerosol Lidar and Pathfinder Satellite Observations
CAS	Cloud Aerosol Spectrometer
CIMP5	Coupled Model Intercomparison Project - Phase 5
CIP	Cloud Imaging Probe
CLaMS	Chemical Lagrangian Model of the Stratosphere
CoCiP	Contrail Cirrus Prediction Tool
CRE	Cirrus Radiative Forcing
DAC	Data Acquisition
DEP	Region of DEPositional ice growth
DFB	Distributed FeedBack laser diode
DIAL	Differential Absorption Lidar
ECMWF	European Centre for Medium-Range Weather forecasts
ECHAM	Acronym derived form ECMWF and HAMburg
EMAC	ECHAM/MESSy Atmospheric Chemistry
HALO	High Altitude and Long Range Research Aircraft
HET_{in}	Region of HETerogeneous freezing inside clouds
HET_{out}	Region of HETerogeneous freezing outside clouds
HOM_{in}	Region of HOMogeneous freezing inside clouds
HOM_{out}	Region of HOMogeneous freezing outside clouds
HSRL	High Spectral Resolution Lidar
ICAO	International Civil Aviation Organization
IPCC AR5	Inter Governmental Panel on Climate Change (5^{th} Assessment Report)
IQR	Inter-Quartile Range
ISSR	Ice SuperSaturated Region
$ISSR_{out}$	Ice SuperSaturated region outside of clouds
IWC	Ice Water Content
KTP	Potassium titanyl phosphate, $KTiOPO_4$
MADE	Modal Aerosol Dynamics model for Europe
MESSy	Modular Earth Submodel System

Abbreviation	Long form
ML-CIRRUS	MidLatitude CIRRUS experiment
NAT	North Atlantic Tracks
NCAS	National Centre for Atmospheric Science
OPO	Optical Parametric Oscillator
PBS	Polarizing BeamSplitter cube
PMT	Photo Multiplier Tube
RF	Radiative Forcing
SEVIRI	Spinning Enhanced Visible Infrared Imager
SHARC	Sophisticated Hygrometer for Atmospheric ResearCH
SUB	Region of SUBlimation inside clouds
TOA	Top-Of-Atmosphere
UTC	Coordinated Universal Time
WALES	Derived from WAter vapor Lidar Experiment in Space
WCB	Warm Conveyor Belt
YAG	Yttrium Aluminium Garnet, $Y_3Al_5O_{12}$

List of symbols

Symbol	Meaning	Unit
α	extinction coefficient	m^{-1}
$\alpha_{\parallel}$	parallel polarized component of the extinction coefficient	m^{-1}
$\alpha_{\perp}$	cross polarized component of the extinction coefficient	m^{-1}
α^{part}	particle extinction coefficient	m^{-1}
$\alpha_{\parallel}^{part}$	parallel polarized component of the particle extinction coefficient	m^{-1}
$\alpha_{\perp}^{part}$	cross polarized component of the particle extinction coefficient	m^{-1}
α_{sca}^{part}	particle extinction coefficient due to scattering	m^{-1}
α_{abs}^{part}	particle extinction coefficient due to absorption	m^{-1}
α_{abs}^{mol}	molecular extinction coefficient due to absorption	m^{-1}
α_{sca}^{mol}	molecular extinction coefficient due to scattering	m^{-1}
β	backscatter coefficient	$\mathrm{m}^{-1}\,\mathrm{sr}^{-1}$
β^{mol}	molecular backscatter coefficient	$\mathrm{m}^{-1}\,\mathrm{sr}^{-1}$
β^{part}	particle backscatter coefficient	$\mathrm{m}^{-1}\,\mathrm{sr}^{-1}$
$\beta_{\parallel}^{part}$	parallel polarized component of the particle backscatter coefficient	$\mathrm{m}^{-1}\,\mathrm{sr}^{-1}$
$\beta_{\perp}^{part}$	cross polarized component of the particle backscatter coefficient	$\mathrm{m}^{-1}\,\mathrm{sr}^{-1}$
$\beta_{\parallel}$	parallel polarized component of the backscatter coefficient	$\mathrm{m}^{-1}\,\mathrm{sr}^{-1}$
$\beta_{\perp}$	cross polarized component of the backscatter coefficient	$\mathrm{m}^{-1}\,\mathrm{sr}^{-1}$
δ^{part}	particle linear depolarization ratio	
δ^{vol}	volume linear depolarization ratio	
δ^{*}	measured signal ratio	
θ	scattering angle	rad
λ	wavelength	m
λ_{on}	on-line wavelength (DIAL)	m
λ_{off}	off-line wavelength (DIAL)	m
σ	molecular absorption cross-section	m^{2}
τ	pulse duration	s
φ	alignment angle between PBS and polarization of emitted laser light	rad
Ω	solid angle	sr
a_w	water activity	
A	system receiving area	m^{2}
c	speed of light	$\mathrm{m}\,\mathrm{s}^{-1}$
C,$C*$	system parameter	$\mathrm{m}^{3}\,\mathrm{sr}$
d	particle diameter	m
d_{eff}	effective particle diameter	m
$e_{sat,i}$	water vapor saturation pressure with respect to ice	Pa
f	slice recording frequency (CIP)	Hz
IWC	ice water content	$\mathrm{g}\,\mathrm{m}^{-3}$
k_B	Bolzmann constant	$\mathrm{J}\,\mathrm{K}^{-1}$
L^{mol}	molecular extinction-to-backscatter lidar ratio	sr
L^{part}	particle extinction-to-backscatter lidar ratio	sr

Symbol	Meaning	Unit
n^{mol}	molecular number concentration	m^{-3}
n^{part}	particle number concentration	m^{-3}
n_{air}	number concentration of air	m^{-3}
P	power	W
P_{on}	power at on-line wavelength	W
P_{off}	power at off-line wavelength	W
P_0	transmitted laser power at time t_0	W
$P_{0,on}$	transmitted laser power at the on-line wavelength	W
$P_{0,off}$	transmitted laser power at the off-line wavelength	W
P^{part}	light power from particle scattering	W
P^{mol}	light power from molecular scattering	W
$P_{\parallel}$	parallel polarized complement of the light power	W
$P_{\perp}$	cross polarized component of the light power	W
P_s	light power component perpendicular to the incident plane of the PBS	W
P_p	light power component parallel to the incident plane of the PBS	W
P_R	power signal in the reflected branch of the PBS	W
P_T	power signal in the transmitted branch of the PBS	W
$\mathbb{P}$	Rayleigh phase function	
r	lidar range	m
r_{H_2O}	water vapour volume mixing ratio	
R_p	reflectance for light parallel polarized to the PBS	
R_s	reflectance for light cross polarized to the PBS	
$\mathbb{R}$	backscatter ratio	
RH_i	relative humidity with respect to ice	
$RH_{i,het}^{CS}$	onset parameterization for hetrogeneous freezing on coated soot	
$RH_{i,het}^{MD}$	onset parameterization for heterogeneous freezing on mieral dust	
$RH_{i,hom}$	homogeneous freezing threshold	
t	time	s
t_0	time of laser pulse emission	s
T	temperature	K
T_p	transmittance for light parallel polarized to the PBS	
T_s	transmittance for light cross polarized to the PBS	
v	true air speed	$\mathrm{m\,s}^{-1}$
V_R	amplification factor in the reflected branch of the PBS	
V_T	amplification factor in the transmitted branch of the PBS	
V^*	relative amplification factor	
x	size parameter	

Bibliography

Ackermann, I. J., H. Hass, M. Memmesheimer, A. Ebel, F. S. Binkowski, and U. Shankar (1998), Modal aerosol dynamics model for europe, *Atmospheric Environment*, *32*(17), 2981–2999, doi:10.1016/s1352-2310(98)00006-5.

Alcala-Jornod, C., H. van den Bergh, and M. J. Rossi (2002), Can soot particles emitted by airplane exhaust contribute to the formation of aviation contrails and cirrus clouds?, *Geophysical Research Letters*, *29*(17), 1114, doi:10.1029/2001gl014115.

Ansmann, A., U. Wandinger, M. Riebesell, C. Weitkamp, and W. Michaelis (1992), Independent measurement of extinction and backscatter profiles in cirrus clouds by using a combined Raman elastic-backscatter lidar, *Applied Optics*, *31*(33), 7113, doi:10.1364/ao.31.007113.

Arienti, M., M. Geier, X. Yang, J. Orcutt, J. Zenker, and S. D. Brooks (2018), An experimental and numerical study of the light scattering properties of ice crystals with black carbon inclusions, *Journal of Quantitative Spectroscopy and Radiative Transfer*, *211*, 50–63, doi:10.1016/j.jqsrt.2018.02.028.

Bailey, M. P., and J. Hallett (2009), A comprehensive habit diagram for atmospheric ice crystals: Confirmation from the laboratory, AIRS II, and other field studies, *Journal of the Atmospheric Sciences*, *66*(9), 2888–2899, doi:10.1175/2009jas2883.1.

Baker, P. W. (1983), Atmospheric water vapor differential absorption measurements on vertical paths with a CO_2 lidar, *Applied Optics*, *22*(15), 2257, doi:10.1364/ao.22.002257.

Baran, A. J. (2012), From the single-scattering properties of ice crystals to climate prediction: A way forward, *Atmospheric Research*, *112*, 45–69, doi:10.1016/j.atmosres.2012.04.010.

Baumgardner, D., H. Jonsson, W. Dawson, D. O'Connor, and R. Newton (2001), The cloud, aerosol and precipitation spectrometer: a new instrument for cloud investigations, *Atmospheric Research*, *59-60*, 251–264, doi:10.1016/s0169-8095(01)00119-3.

Behrendt, A., and T. Nakamura (2002), Calculation of the calibration constant of polarization lidar and its dependency on atmospheric temperature, *Optics Express*, *10*(16), 805, doi:10.1364/oe.10.000805.

Boucher, O., D. Randall, P. Artaxo, C. Bretherton, G. Feingold, P. Forster, V.-M. Kerminen, Y. Kondo, H. Liao, U. Lohmann, P. Rasch, S. Satheesh, S. Sherwood, B. Stevens, and X. Zhang (2013), Clouds and aerosols, in *Climate Change 2013 - The Physical Science Basis*, edited by Intergovernmental Panel on Climate Change, pp. 571–658, Cambridge University Press, doi:10.1017/cbo9781107415324.016.

Browell, E. V., T. D. Wilkerson, and T. J. Mcilrath (1979), Water vapor differential absorption lidar development and evaluation, *Applied Optics*, *18*(20), 3474, doi:10.1364/ao.18.003474.

Burkhardt, U., and B. Kärcher (2011), Global radiative forcing from contrail cirrus, *Nature Climate Change*, *1*(1), 54–58, doi:10.1038/nclimate1068.

Burkhardt, U., B. Kärcher, and U. Schumann (2010), Global modeling of the contrail and contrail cirrus climate impact, *Bulletin of the American Meteorological Society*, *91*(4), 479–484, doi:10.1175/2009bams2656.1.

Collis, R. T. H. (1965), Lidar observation of cloud, *Science*, *149*(3687), 978–981, doi:10.1126/science.149.3687.978.

Collis, R. T. H., and M. G. H. Ligda (1964), Laser radar echoes from the clear atmosphere, *Nature*, *203*(4944), 508–508, doi:10.1038/203508a0.

Cziczo, D. J., K. D. Froyd, C. Hoose, E. J. Jensen, M. Diao, M. A. Zondlo, J. B. Smith, C. H. Twohy, and D. M. Murphy (2013), Clarifying the dominant sources and mechanisms of cirrus cloud formation, *Science*, *340*(6138), 1320–1324, doi:10.1126/science.1234145.

Davis, P. A. (1969), The analysis of lidar signatures of cirrus clouds, *Applied Optics*, *8*(10), 2099, doi:10.1364/ao.8.002099.

Davis, P. A. (1971), Applications of an airborne ruby lidar during a BOMEX program of cirrus observations, *Journal of Applied Meteorology*, *10*(6), 1314–1323, doi:10.1175/1520-0450(1971)010⟨1314:aoaarl⟩2.0.co;2.

DeMott, P. J., Y. Chen, S. M. Kreidenweis, D. C. Rogers, and D. E. Sherman (1999), Ice formation by black carbon particles, *Geophysical Research Letters*, *26*(16), 2429–2432, doi:10.1029/1999gl900580.

DeMott, P. J., A. J. Prenni, X. Liu, S. M. Kreidenweis, M. D. Petters, C. H. Twohy, M. S. Richardson, T. Eidhammer, and D. C. Rogers (2010), Predicting global atmospheric ice nuclei distributions and their impacts on climate, *Proceedings of the National Academy of Sciences*, *107*(25), 11,217–11,222, doi:10.1073/pnas.0910818107.

Denning, R. F., S. L. Guidero, G. S. Parks, and B. L. Gary (1989), Instrument description of the airborne microwave temperature profiler, *Journal of Geophysical Research*, *94*(D14), 16,757, doi:10.1029/jd094id14p16757.

Diao, M., M. A. Zondlo, A. J. Heymsfield, S. P. Beaton, and D. C. Rogers (2013), Evolution of ice crystal regions on the microscale based on in situ observations, *Geophysical Research Letters*, *40*(13), 3473–3478, doi:10.1002/grl.50665.

Eckhardt, S., A. Stohl, H. Wernli, P. James, C. Forster, and N. Spichtinger (2004), A 15-year climatology of warm conveyor belts, *Journal of Climate*, *17*(1), 218–237, doi:10.1175/1520-0442(2004)017⟨0218:aycowc⟩2.0.co;2.

Eloranta, E. E. (2005), High spectral resolution lidar, in *Lidar*, pp. 143–163, Springer-Verlag, doi:10.1007/0-387-25101-4_5.

Esselborn, M., M. Wirth, A. Fix, M. Tesche, and G. Ehret (2008), Airborne high spectral resolution lidar for measuring aerosol extinction and backscatter coefficients, *Applied Optics*, *47*(3), 346, doi:10.1364/ao.47.000346.

Freudenthaler, V., F. Homburg, and H. Jäger (1996), Optical parameters of contrails from lidar measurements: Linear depolarization, *Geophysical Research Letters*, *23*(25), 3715–3718, doi:10.1029/96gl03646.

Freudenthaler, V., M. Esselborn, M. Wiegner, B. Heese, M. Tesche, A. Ansmann, D. Müller, D. Althausen, M. Wirth, A. Fix, G. Ehret, P. Knippertz, C. Toledano, J. Gasteiger, M. Garhammer, and M. Seefeldner (2009), Depolarization ratio profiling at several wavelengths in pure saharan dust during SAMUM 2006, *Tellus B: Chemical and Physical Meteorology*, *61*(1), 165–179, doi:10.1111/j.1600-0889.2008.00396.x.

Gallagher, M. W., P. J. Connolly, I. Crawford, A. Heymsfield, K. N. Bower, T. W. Choularton, G. Allen, M. J. Flynn, G. Vaughan, and J. Hacker (2012), Observations and modelling of microphysical variability, aggregation and sedimentation in tropical anvil cirrus outflow regions, *Atmospheric Chemistry and Physics*, *12*(14), 6609–6628, doi:10.5194/acp-12-6609-2012.

Gasparini, B., S. Münch, L. Poncet, M. Feldmann, and U. Lohmann (2017), Is increasing ice crystal sedimentation velocity in geoengineering simulations a good proxy for cirrus cloud seeding?, *Atmospheric Chemistry and Physics*, *17*(7), 4871–4885, doi:10.5194/acp-17-4871-2017.

Gettelman, A., and C. Chen (2013), The climate impact of aviation aerosols, *Geophysical Research Letters*, *40*(11), 2785–2789, doi:10.1002/grl.50520.

Gimmestad, G. G. (2005), Differential-absorption lidar for ozone and industrial emissions, in *Lidar*, pp. 187–212, Springer-Verlag, doi:10.1007/0-387-25101-4_7.

Goyer, G. G., and R. Watson (1963), The laser and its application to meteorology, *Bulletin of the American Meteorological Society*, *44*(9), 564–570, doi:10.1175/1520-0477-44.9.564.

Groß, S., M. Esselborn, B. Weinzierl, M. Wirth, A. Fix, and A. Petzold (2013), Aerosol classification by airborne high spectral resolution lidar observations, *Atmospheric Chemistry and Physics*, *13*(5), 2487–2505, doi:10.5194/acp-13-2487-2013.

Groß, S., M. Wirth, A. Schäfler, A. Fix, S. Kaufmann, and C. Voigt (2014), Potential of airborne lidar measurements for cirrus cloud studies, *Atmospheric Measurement Techniques*, *7*(8), 2745–2755, doi:10.5194/amt-7-2745-2014.

Hawkins, E. (2018), Warming strips, url: `https://www.climate-lab-book.ac.uk/2018/warming-stripes/`, visited 2019-06-01.

Hendricks, J., B. Kärcher, U. Lohmann, and M. Ponater (2005), Do aircraft black carbon emissions affect cirrus clouds on the global scale?, *Geophysical Research Letters*, *32*(12), doi:10.1029/2005gl022740.

Heymsfield, A., D. Baumgardner, P. DeMott, P. Forster, K. Gierens, and B. Kärcher (2010), Contrail microphysics, *Bulletin of the American Meteorological Society*, *91*(4), 465–472, doi:10.1175/2009bams2839.1.

Heymsfield, A. J., and L. M. Miloshevich (1995), Relative humidity and temperature influences on cirrus formation and evolution: Observations from wave clouds and FIRE II, *Journal of the Atmospheric Sciences*, *52*(23), 4302–4326, doi:10.1175/1520-0469(1995)052⟨4302:rhatio⟩2.0.co;2.

Hoose, C., and O. Möhler (2012), Heterogeneous ice nucleation on atmospheric aerosols: a review of results from laboratory experiments, *Atmospheric Chemistry and Physics*, *12*(20), 9817–9854, doi:10.5194/acp-12-9817-2012.

Iwabuchi, H., P. Yang, K. N. Liou, and P. Minnis (2012), Physical and optical properties of persistent contrails: Climatology and interpretation, *Journal of Geophysical Research: Atmospheres*, *117*(D6), doi:10.1029/2011jd017020.

Jensen, E. J., and O. B. Toon (1997), The potential impact of soot particles from aircraft exhaust on cirrus clouds, *Geophysical Research Letters*, *24*(3), 249–252, doi:10.1029/96gl03235.

Jöckel, P., R. Sander, A. Kerkweg, H. Tost, and J. Lelieveld (2005), Technical note: The modular earth submodel system (MESSy) - a new approach towards earth system modeling, *Atmospheric Chemistry and Physics*, *5*(2), 433–444, doi:10.5194/acp-5-433-2005.

Kaufmann, S., C. Voigt, R. Heller, T. Jurkat-Witschas, M. Krämer, C. Rolf, M. Zöger, A. Giez, B. Buchholz, V. Ebert, T. Thornberry, and U. Schumann (2018), Intercomparison of midlatitude tropospheric and lower-stratospheric water vapor measurements and comparison to ECMWF humidity data, *Atmospheric Chemistry and Physics*, *18*(22), 16,729–16,745, doi:10.5194/acp-18-16729-2018.

Klett, J. D. (1981), Stable analytical inversion solution for processing lidar returns, *Applied Optics*, *20*(2), 211, doi:10.1364/ao.20.000211.

Koop, T., B. Luo, A. Tsias, and T. Peter (2000), Water activity as the determinant for homogeneous ice nucleation in aqueous solutions, *Nature*, *406*(6796), 611–614, doi:10.1038/35020537.

Korolev, A., and G. A. Isaac (2006), Relative humidity in liquid, mixed-phase, and ice clouds, *Journal of the Atmospheric Sciences*, *63*(11), 2865–2880, doi:10.1175/jas3784.1.

Kristensson, A., J. F. Gayet, J. Ström, and F. Auriol (2000), In situ observations of a reduction in effective crystal diameter in cirrus clouds near flight corridors, *Geophysical Research Letters*, *27*(5), 681–684, doi:10.1029/1999gl010934.

Krämer, M., C. Rolf, A. Luebke, A. Afchine, N. Spelten, A. Costa, J. Meyer, M. Zöger, J. Smith, R. L. Herman, B. Buchholz, V. Ebert, D. Baumgardner, S. Borrmann, M. Klingebiel, and L. Avallone (2016), A microphysics guide to cirrus clouds – part 1: Cirrus types, *Atmospheric Chemistry and Physics*, *16*(5), 3463–3483, doi:10.5194/acp-16-3463-2016.

Kärcher, B. (2018), Formation and radiative forcing of contrail cirrus, *Nature Communications*, *9*(1), doi:10.1038/s41467-018-04068-0.

Kärcher, B., and U. Lohmann (2002), A parameterization of cirrus cloud formation: Homogeneous freezing of supercooled aerosols, *Journal of Geophysical Research*, *107*(D2), doi:10.1029/2001jd000470.

Kärcher, B., O. Möhler, P. J. DeMott, S. Pechtl, and F. Yu (2007), Insights into the role of soot aerosols in cirrus cloud formation, *Atmospheric Chemistry and Physics*, *7*(16), 4203–4227, doi:10.5194/acp-7-4203-2007.

Kärcher, B., U. Burkhardt, A. Bier, L. Bock, and I. J. Ford (2015), The microphysical pathway to contrail formation, *Journal of Geophysical Research: Atmospheres*, *120*(15), 7893–7927, doi:10.1002/2015jd023491.

Kübbeler, M., M. Hildebrandt, J. Meyer, C. Schiller, T. Hamburger, T. Jurkat, A. Minikin, A. Petzold, M. Rautenhaus, H. Schlager, U. Schumann, C. Voigt, P. Spichtinger, J.-F. Gayet, C. Gourbeyre, and M. Krämer (2011), Thin and subvisible cirrus and contrails in a subsaturated environment, *Atmospheric Chemistry and Physics*, *11*(12), 5853–5865, doi:10.5194/acp-11-5853-2011.

Lamarque, J.-F., T. C. Bond, V. Eyring, C. Granier, A. Heil, Z. Klimont, D. Lee, C. Liousse, A. Mieville, B. Owen, M. G. Schultz, D. Shindell, S. J. Smith, E. Stehfest, J. V. Aardenne, O. R. Cooper, M. Kainuma, N. Mahowald, J. R. McConnell, V. Naik, K. Riahi, and D. P. van Vuuren (2010), Historical (1850–2000) gridded anthropogenic and biomass burning emissions of reactive gases and aerosols: methodology and application, *Atmospheric Chemistry and Physics*, *10*(15), 7017–7039, doi:10.5194/acp-10-7017-2010.

Lee, D. S., D. W. Fahey, P. M. Forster, P. J. Newton, R. C. Wit, L. L. Lim, B. Owen, and R. Sausen (2009), Aviation and global climate change in the 21st century, *Atmospheric Environment*, *43*(22-23), 3520–3537, doi:10.1016/j.atmosenv.2009.04.024.

Liou, K. (1986), Influence of cirrus clouds on weather and climate processes: A global perspective, *Monthly Weather Review*, *114*(6), 1167–1199, doi:10.1175/1520-0493(1986)114⟨1167:ioccow⟩2.0.co;2.

Liou, K., and H. Lahore (1974), Laser sensing of cloud composition: A backscattered depolarization technique, *Journal of Applied Meteorology*, *13*(2), 257–263, doi:10.1175/1520-0450(1974)013⟨0257:lsocca⟩2.0.co;2.

Lund, M. T., B. Aamaas, T. Berntsen, L. Bock, U. Burkhardt, J. S. Fuglestvedt, and K. P. Shine (2017), Emission metrics for quantifying regional climate impacts of aviation, *Earth System Dynamics*, *8*(3), 547–563, doi:10.5194/esd-8-547-2017.

Maddrea, G. L., and R. J. Bendura (1981), NASA participation in the 1980 persistent elevated pollution episode/northeast regional oxidant study (PEPE/NEROS) project: operational aspects, *Tech. rep.*, NASA.

Mahrt, F., C. Marcolli, R. O. David, P. Grönquist, E. J. B. Meier, U. Lohmann, and Z. A. Kanji (2018), Ice nucleation abilities of soot particles determined with the horizontal ice nucleation chamber, *Atmospheric Chemistry and Physics*, *18*(18), 13,363–13,392, doi:10.5194/acp-18-13363-2018.

Maiman, T. H. (1960), Stimulated optical radiation in ruby, *Nature*, *187*(4736), 493–494, doi:10.1038/187493a0.

Marcolli, C. (2014), Deposition nucleation viewed as homogeneous or immersion freezing in pores and cavities, *Atmospheric Chemistry and Physics*, *14*(4), 2071–2104, doi:10.5194/acp-14-2071-2014.

Marcolli, C. (2017), Pre-activation of aerosol particles by ice preserved in pores, *Atmospheric Chemistry and Physics*, *17*(3), 1595–1622, doi:10.5194/acp-17-1595-2017.

McKenna, D. S. (2002), A new Chemical Lagrangian Model of the Stratosphere (CLaMS) 1. formulation of advection and mixing, *Journal of Geophysical Research*, *107*(D16), doi:10.1029/2000jd000114.

Minikin, A., A. Petzold, J. Ström, R. Krejci, M. Seifert, P. van Velthoven, H. Schlager, and U. Schumann (2003), Aircraft observations of the upper tropospheric fine particle aerosol in the Northern and Southern hemispheres at midlatitudes, *Geophysical Research Letters*, *30*(10), n/a–n/a, doi:10.1029/2002gl016458.

Minnis, P., J. K. Ayers, R. Palikonda, and D. Phan (2004), Contrails, cirrus trends, and climate, *Journal of Climate*, *17*(8), 1671–1685, doi:10.1175/1520-0442(2004)017⟨1671:cctac⟩2.0.co;2.

Mishchenko, M. I., and K. Sassen (1998), Depolarization of lidar returns by small ice crystals: An application to contrails, *Geophysical Research Letters*, *25*(3), 309–312, doi: 10.1029/97gl03764.

Moore, R. H., K. L. Thornhill, B. Weinzierl, D. Sauer, E. D'Ascoli, J. Kim, M. Lichtenstern, M. Scheibe, B. Beaton, A. J. Beyersdorf, J. Barrick, D. Bulzan, C. A. Corr, E. Crosbie, T. Jurkat, R. Martin, D. Riddick, M. Shook, G. Slover, C. Voigt, R. White, E. Winstead, R. Yasky, L. D. Ziemba, A. Brown, H. Schlager, and B. E. Anderson (2017), Biofuel blending reduces particle emissions from aircraft engines at cruise conditions, *Nature*, *543*(7645), 411–415, doi:10.1038/nature21420.

Murphy, D. M., and T. Koop (2005), Review of the vapour pressures of ice and supercooled water for atmospheric applications, *Quarterly Journal of the Royal Meteorological Society*, *131*(608), 1539–1565, doi:10.1256/qj.04.94.

Möhler, O., C. Linke, H. Saathoff, M. Schnaiter, R. Wagner, A. Mangold, M. Krämer, and U. Schurath (2005), Ice nucleation on flame soot aerosol of different organic carbon content, *Meteorologische Zeitschrift*, *14*(4), 477–484, doi:10.1127/0941-2948/2005/0055.

Müller, D., A. Ansmann, I. Mattis, M. Tesche, U. Wandinger, D. Althausen, and G. Pisani (2007), Aerosol-type-dependent lidar ratios observed with raman lidar, *Journal of Geophysical Research*, *112*(D16), doi:10.1029/2006jd008292.

National Research Council (2010), *Advancing the Science of Climate Change*, 1 pp., National Academies Press, doi:10.17226/12782.

Noel, V., H. Chepfer, G. Ledanois, A. Delaval, and P. H. Flamant (2002), Classification of particle effective shape ratios in cirrus clouds based on the lidar depolarization ratio, *Applied Optics*, *41*(21), 4245, doi:10.1364/ao.41.004245.

Noel, V., H. Chepfer, M. Haeffelin, and Y. Morille (2006), Classification of ice crystal shapes in midlatitude ice clouds from three years of lidar observations over the SIRTA observatory, *Journal of the Atmospheric Sciences*, *63*(11), 2978–2991, doi:10.1175/jas3767.1.

Northend, C. A., R. C. Honey, and W. E. Evans (1966), Laser radar (lidar) for meteorological observations, *Review of Scientific Instruments*, *37*(4), 393–400, doi:10.1063/1.1720199.

Ovarlez, J., J.-F. Gayet, K. Gierens, J. Ström, H. Ovarlez, F. Auriol, R. Busen, and U. Schumann (2002), Water vapour measurements inside cirrus clouds in northern and southern hemispheres during INCA, *Geophysical Research Letters*, *29*(16), 60–1–60–4, doi:10.1029/2001gl014440.

Righi, M., J. Hendricks, and R. Sausen (2013), The global impact of the transport sectors on atmospheric aerosol: simulations for year 2000 emissions, *Atmospheric Chemistry and Physics*, *13*(19), 9939–9970, doi:10.5194/acp-13-9939-2013.

Sassen, K. (1991), The polarization lidar technique for cloud research: A review and current assessment, *Bulletin of the American Meteorological Society*, *72*(12), 1848–1866, doi:10.1175/1520-0477(1991)072⟨1848:tpltfc⟩2.0.co;2.

Sassen, K. (2005), Polarization in lidar, in *Lidar*, pp. 19–42, Springer-Verlag, doi:10.1007/0-387-25101-4_2.

Sassen, K., and S. Benson (2001), A midlatitude cirrus cloud climatology from the facility for atmospheric remote sensing. part II: Microphysical properties derived from lidar depolarization, *Journal of the Atmospheric Sciences*, *58*(15), 2103–2112, doi:10.1175/1520-0469(2001)058⟨2103:amcccf⟩2.0.co;2.

Sassen, K., and J. Zhu (2009), A global survey of CALIPSO linear depolarization ratios in ice clouds: Initial findings, *Journal of Geophysical Research*, *114*, doi:10.1029/2009jd012279.

Sassen, K., Z. Wang, and D. Liu (2008), Global distribution of cirrus clouds from CloudSat/cloud-aerosol lidar and infrared pathfinder satellite observations (CALIPSO) measurements, *Journal of Geophysical Research*, *113*, doi:10.1029/2008jd009972.

Schnaiter, M., S. Büttner, O. Möhler, J. Skrotzki, M. Vragel, and R. Wagner (2012), Influence of particle size and shape on the backscattering linear depolarisation ratio of small ice crystals - cloud chamber measurements in the context of contrail and cirrus microphysics, *Atmospheric Chemistry and Physics*, *12*(21), 10,465–10,484, doi:10.5194/acp-12-10465-2012.

Schnaiter, M., E. Järvinen, P. Vochezer, A. Abdelmonem, R. Wagner, O. Jourdan, G. Mioche, V. N. Shcherbakov, C. G. Schmitt, U. Tricoli, Z. Ulanowski, and A. J. Heymsfield (2016), Cloud chamber experiments on the origin of ice crystal complexity in cirrus clouds, *Atmospheric Chemistry and Physics*, *16*(8), 5091–5110, doi:10.5194/acp-16-5091-2016.

Schumann, U. (2012), A contrail cirrus prediction model, *Geoscientific Model Development*, *5*(3), 543–580, doi:10.5194/gmd-5-543-2012.

Schumann, U., and K. Graf (2013), Aviation-induced cirrus and radiation changes at diurnal timescales, *Journal of Geophysical Research: Atmospheres*, *118*(5), 2404–2421, doi:10.1002/jgrd.50184.

Schumann, U., R. Baumann, D. Baumgardner, S. T. Bedka, D. P. Duda, V. Freudenthaler, J.-F. Gayet, A. J. Heymsfield, P. Minnis, M. Quante, E. Raschke, H. Schlager, M. Vázquez-Navarro, C. Voigt, and Z. Wang (2017), Properties of individual contrails: a compilation of observations and some comparisons, *Atmospheric Chemistry and Physics*, *17*(1), 403–438, doi:10.5194/acp-17-403-2017.

Shipley, S. T., D. H. Tracy, E. W. Eloranta, J. T. Trauger, J. T. Sroga, F. L. Roesler, and J. A. Weinman (1983), High spectral resolution lidar to measure optical scattering properties of atmospheric aerosols 1: Theory and instrumentation, *Applied Optics*, *22*(23), 3716, doi:10.1364/ao.22.003716.

Spichtinger, P., and K. M. Gierens (2009), Modelling of cirrus clouds – part 1b: Structuring cirrus clouds by dynamics, *Atmospheric Chemistry and Physics*, *9*(2), 707–719, doi:10.5194/acp-9-707-2009.

Spichtinger, P., K. Gierens, H. G. J. Smit, J. Ovarlez, and J.-F. Gayet (2004), On the distribution of relative humidity in cirrus clouds, *Atmospheric Chemistry and Physics*, *4*(3), 639–647, doi:10.5194/acp-4-639-2004.

Stephens, G. L., S.-C. Tsay, P. W. Stackhouse, and P. J. Flatau (1990), The relevance of the microphysical and radiative properties of cirrus clouds to climate and climatic feedback, *Journal of the Atmospheric Sciences*, *47*(14), 1742–1754, doi:10.1175/1520-0469(1990)047⟨1742:trotma⟩2.0.co;2.

Stettler, M. E., A. M. Boies, A. Petzold, and S. R. Barrett (2013), Global civil aviation black carbon emissions, *Environmental Science & Technology*, p. 130823150610008, doi:10.1021/es401356v.

Ström, J., and S. Ohlsson (1998), In situ measurements of enhanced crystal number densities in cirrus clouds caused by aircraft exhaust, *Journal of Geophysical Research: Atmospheres*, *103*(D10), 11,355–11,361, doi:10.1029/98jd00807.

Stubenrauch, C. J., A. Chédin, G. Rädel, N. A. Scott, and S. Serrar (2006), Cloud properties and their seasonal and diurnal variability from TOVS path-b, *Journal of Climate*, *19*(21), 5531–5553, doi:10.1175/jcli3929.1.

Tesche, M., P. Achtert, P. Glantz, and K. J. Noone (2016), Aviation effects on already-existing cirrus clouds, *Nature Communications*, *7*(1), doi:10.1038/ncomms12016.

Urbanek, B., S. Groß, A. Schäfler, and M. Wirth (2017), Determining stages of cirrus evolution: a cloud classification scheme, *Atmospheric Measurement Techniques*, *10*(5), 1653–1664, doi:10.5194/amt-10-1653-2017.

Urbanek, B., S. Groß, M. Wirth, C. Rolf, M. Krämer, and C. Voigt (2018), High depolarization ratios of naturally occurring cirrus clouds near air traffic regions over europe, *Geophysical Research Letters*, *45*(23), 13,166–13,172, doi:10.1029/2018gl079345.

Voigt, C., U. Schumann, P. Jessberger, T. Jurkat, A. Petzold, J.-F. Gayet, M. Krämer, T. Thornberry, and D. W. Fahey (2011), Extinction and optical depth of contrails, *Geophysical Research Letters*, *38*(11), doi:10.1029/2011gl047189.

Voigt, C., U. Schumann, A. Minikin, A. Abdelmonem, A. Afchine, S. Borrmann, M. Boettcher, B. Buchholz, L. Bugliaro, A. Costa, J. Curtius, M. Dollner, A. Dörnbrack, V. Dreiling, V. Ebert, A. Ehrlich, A. Fix, L. Forster, F. Frank, D. Fütterer, A. Giez, K. Graf, J.-U. Grooß, S. Groß, K. Heimerl, B. Heinold, T. Hüneke, E. Järvinen, T. Jurkat, S. Kaufmann, M. Kenntner, M. Klingebiel, T. Klimach, R. Kohl, M. Krämer, T. C. Krisna, A. Luebke, B. Mayer, S. Mertes, S. Molleker, A. Petzold, K. Pfeilsticker, M. Port, M. Rapp, P. Reutter, C. Rolf, D. Rose, D. Sauer, A. Schäfler, R. Schlage, M. Schnaiter, J. Schneider, N. Spelten, P. Spichtinger, P. Stock, A. Walser, R. Weigel, B. Weinzierl, M. Wendisch, F. Werner, H. Wernli, M. Wirth, A. Zahn, H. Ziereis, and M. Zöger (2017), ML-CIRRUS: The airborne experiment on natural cirrus and contrail cirrus with the high-altitude long-range research aircraft HALO, *Bulletin of the American Meteorological Society*, *98*(2), 271–288, doi:10.1175/bams-d-15-00213.1.

Weigel, R., P. Spichtinger, C. Mahnke, M. Klingebiel, A. Afchine, A. Petzold, M. Krämer, A. Costa, S. Molleker, T. Jurkat, A. Minikin, and S. Borrmann (2015), Thermodynamic correction of particle concentrations measured by underwing probes on fast flying aircraft, *Atmospheric Measurement Techniques Discussions*, *8*(12), 13,423–13,469, doi:10.5194/amtd-8-13423-2015.

Wendisch, M., P. Yang, and P. Pilewskie (2007), Effects of ice crystal habit on thermal infrared radiative properties and forcing of cirrus, *Journal of Geophysical Research*, *112*(D8), doi:10.1029/2006jd007899.

Wielicki, B. A., E. F. Harrison, R. D. Cess, M. D. King, and D. A. Randall (1995), Mission to planet earth: Role of clouds and radiation in climate, *Bulletin of the American Meteorological Society*, *76*(11), 2125–2153, doi:10.1175/1520-0477(1995)076⟨2125:mtpero⟩2.0.co;2.

Wirth, M., A. Fix, P. Mahnke, H. Schwarzer, F. Schrandt, and G. Ehret (2009), The airborne multi-wavelength water vapor differential absorption lidar WALES: system design and performance, *Applied Physics B*, *96*(1), 201–213, doi:10.1007/s00340-009-3365-7.

Wylie, D. P., and W. P. Menzel (1999), Eight years of high cloud statistics using HIRS, *Journal of Climate*, *12*(1), 170–184, doi:10.1175/1520-0442-12.1.170.

Yi, B., P. Yang, B. A. Baum, T. L'Ecuyer, L. Oreopoulos, E. J. Mlawer, A. J. Heymsfield, and K.-N. Liou (2013), Influence of ice particle surface roughening on the global cloud radiative effect, *Journal of the Atmospheric Sciences*, *70*(9), 2794–2807, doi:10.1175/jas-d-13-020.1.

Zhang, M. H. (2005), Comparing clouds and their seasonal variations in 10 atmospheric general circulation models with satellite measurements, *Journal of Geophysical Research*, *110*(D15), doi:10.1029/2004jd005021.

Zhang, Y., A. Macke, and F. Albers (1999), Effect of crystal size spectrum and crystal shape on stratiform cirrus radiative forcing, *Atmospheric Research*, *52*(1-2), 59–75, doi: 10.1016/s0169-8095(99)00026-5.

Zhou, C., and J. E. Penner (2014), Aircraft soot indirect effect on large-scale cirrus clouds: Is the indirect forcing by aircraft soot positive or negative?, *Journal of Geophysical Research*, *119*(19), doi:10.1002/2014JD021914.

Acknowledgments

This work is the result of my research at "Institut für Physik der Atmosphäre" of the German Aerospace Center (DLR) Oberpfaffenhofen. I want to thank all people that supported me during this endeavor.

First of all, I want to thank Dr. Silke Groß for giving me the opportunity for this work, her gentle guidance over the last three years and many fruitful discussions of this thesis. Further, I want to thank my supervisors Prof. Dr. Bernhard Mayer and Prof. Dr. Markus Rapp for their continuous interest and support. My thank goes to Dr. Martin Wirth for his technical help and discussions concerning the lidar system WALES.

I thank Prof. Dr. Christiane Voigt and Tina Jurkat-Witschas for providing in-situ data recorded during the ML-CIRRUS campaign and for helping in the interpretation of the data analysis in the context of an indirect aerosol effect from aviation. I want to thank Prof. Dr. Ulrich Schumann for providing CoCiP simulations that helped to exclude the influence of embedded contrails.

I thank Dr. Martina Krämer and Dr. Christian Rolf for early discussions of my findings and for providing backward trajectories for the investigated cloud cases.

My special thanks goes to my colleges Dr. Benedikt Ehard, Dr. Florian Ewald, Dr. Andreas Schäfler, Dr. Quitterie Cazenave, Manuel Gutleben, Robert Reichert, Sebastian Wolff, Dr. Eleni Marinou, and Eleni Tetoni for many whiteboard sessions and discussions in the coffee kitchen and for the good spirit in our office.

All this would not have been possible without the strong support of my wife Anna.